ARMY RESEARCH LABORATORY

Experimental Evaluation and Numerical Simulations of Multi-Driver Shock Tube Flow

Stephen J. Schraml
Christopher Mermagen

ARL-TR-1084 APRIL 1996

The findings in this report are not to be construed as an official Department of the Army position unless so designated by other authorized documents.

Citation of manufacturer's or trade names does not constitute an official endorsement or approval of the use thereof.

Destroy this report when it is no longer needed. Do not return it to the originator.

REPORT DOCUMENTATION PAGE

Form Approved
OMB No. 0704-0188

1. AGENCY USE ONLY *(Leave blank)*	2. REPORT DATE	3. REPORT TYPE AND DATES COVERED
	April 1996	Final

4. TITLE AND SUBTITLE

Experimental Evaluation and Numerical Simulations of Multi-Driver Shock Tube Flow

5. FUNDING NUMBERS

PR: 68N522

6. AUTHOR(S)

Schraml, S.J.; Mermagen, C.

7. PERFORMING ORGANIZATION NAME(S) AND ADDRESS(ES)

U.S. Army Research Laboratory
Weapons Technology Directorate
Aberdeen Proving Ground, MD 21010-5066

8. PERFORMING ORGANIZATION REPORT NUMBER

9. SPONSORING/MONITORING AGENCY NAME(S) AND ADDRESS(ES)

U.S. Army Research Laboratory
Weapons Technology Directorate
Aberdeen Proving Ground, MD 21010-5066

10. SPONSORING/MONITORING AGENCY REPORT NUMBER

ARL-TR-1084

11. SUPPLEMENTARY NOTES

12a. DISTRIBUTION/AVAILABILITY STATEMENT

Approved for public release; distribution is unlimited.

12b. DISTRIBUTION CODE

13. ABSTRACT *(Maximum 200 words)*

The U.S. Army Research Laboratory and the Centre d'Etudes de Gramat, France, executed a cooperative study in which the time-dependent flow fields in *Le Simulateur de Souffle à Grand Gabarit* (SSGG) large blast simulator were examined. The flow characteristics of static and stagnation overpressure were measured at two longitudinal positions in the expansion tunnel of the simulator. Instrumentation rakes were designed and fabricated to support a total of 19 pairs of static and stagnation pressure transducers that were distributed across the expansion tunnel cross section at each of the longitudinal positions. Flow measurements were recorded for eight shots with peak static overpressure levels between 20 kPa and 120 kPa. The measured data were used to assess the flow uniformity and distribution at each of the longitudinal measurement positions in the simulator. A finite difference Euler equation solver and a finite volume Navier-Stokes equation solver were employed in a set of detailed, three-dimensional (3-D) fluid dynamics calculations that were performed to match the test conditions. The 3-D computational results are compared to the experimental data to further examine the time-dependent flow characteristics and to validate the fluid dynamics codes for future blast studies.

14. SUBJECT TERMS

blast; flow fields; nuclear explosion simulation; nuclear weapons; shock tubes

15. NUMBER OF PAGES

75

16. PRICE CODE

17. SECURITY CLASSIFICATION OF REPORT	18. SECURITY CLASSIFICATION OF THIS PAGE	19. SECURITY CLASSIFICATION OF ABSTRACT	20. LIMITATION OF ABSTRACT
Unclassified	Unclassified	Unclassified	

INTENTIONALLY LEFT BLANK

ACKNOWLEDGMENTS

The experiments described in this report were performed at the Centre d'Etudes de Gramat (CEG), France. The authors extend their gratitude to Daniel Mergnat and Solange Gratias of CEG, who led the experimental effort. Their diligence and efficiency in executing the experimental program culminated in the test results, which are the foundation of this report.

The finite volume flow solutions discussed in this report were based on previous work performed at the U.S. Army Research Laboratory by Dixie Hisley. These initial computational investigations provided the basis for the development and execution of the Navier-Stokes solutions presented here. Ms. Hisley also performed a technical review of this report and made many valuable suggestions to improve its content.

The finite volume flow solver was developed by the Rockwell International Science Center, under the direction of Dr. Sukumar Chakravarthy. Dr. Dale Ota of Rockwell maintained the code library at ARL and kept it in efficient working order.

The k-ϵ turbulence model used in the finite difference solutions was incorporated into the 3-D finite difference code by Mr. Joseph Crepeau, formerly of S-Cubed and now with Applied Research Associates. Mr. Crepeau also maintained this code on the computer systems used to perform the finite difference flow solutions.

INTENTIONALLY LEFT BLANK

TABLE OF CONTENTS

INTENTIONALLY LEFT BLANK

LIST OF FIGURES

LIST OF FIGURES (continued)

Figure **Page**

LIST OF FIGURES (continued)

INTENTIONALLY LEFT BLANK

LIST OF TABLES

INTENTIONALLY LEFT BLANK

1. INTRODUCTION

The U.S. Army Research Laboratory (ARL) and its predecessor organization, the U.S. Army Ballistic Research Laboratory, have played a significant role in the technology development of the Large Blast/Thermal Simulator (LB/TS), a Defense Nuclear Agency (DNA) testing facility at the White Sands Missile Range, New Mexico. During the concept and early design phases, the operational characteristics and the primary dimensions of the facility were determined through a combination of small scale experiments[1], computational fluid dynamics (CFD) simulations[2], and a transfer of technology employed at the Centre d'Etudes de Gramat (CEG), France.[3] To develop the required simulation technology in a timely and cost-effective manner, the experimental work was primarily performed in small, cylindrical shock tubes. The accompanying numerical simulations were performed in a quasi-one-dimensional or two-dimensional (2-D) axisymmetric representation.

With the knowledge that three-dimensional (3-D) numerical simulations would be required for the LB/TS characterization and development of advanced testing methodologies, it became necessary to validate some candidate 3-D CFD codes to model the facility in full geometric detail. To accomplish this task, CEG and ARL formed a cooperative research agreement in which the flow characteristics of the Simulateur de Souffle à Grand Gabarit (SSGG)[4, 5] large blast simulator at CEG would be mapped experimentally and the data used to validate candidate CFD codes.

While several multiple driver, large blast simulators such as the SSGG exist in the world, experimental data providing detailed characteristics of flow throughout the expansion tunnel were sparse or completely unavailable. Because the LB/TS concept is primarily based on the design and operational characteristics of the SSGG, it is the optimum vehicle for providing these data.[6]

It is possible to build and operate a small scale, multiple driver model of this type of facility[7], but this approach presents several challenging obstacles. Because this type of blast simulator is very large, a laboratory shock tube model must be constructed on a scale factor of 20 or greater for convenience of operation and manipulation. When scaled down, the throat section of one driver tube may have a diameter as small as 2 to 3 centimeters. The fluid boundary layer in a throat section of this size can be a significant fraction of the throat diameter, resulting in driver emptying times that are not representative of the full scale facility. Simultaneous firing of several drivers is difficult in a small scale blast simulator because the time scale is identical to the length scale. As a result, a small difference in diaphragm rupture times in the model will be equivalent to a significant delay between driver firings on full scale.

To overcome these difficulties in performing small scale tests of multiple driver shock tube flow, the shock tube geometry is sometimes simplified in the development of the model. Small scale, cylindrical shock tube models are developed using the approach of combining an available set of flow areas at a common longitudinal position into a single cross section of the equivalent area. Combining the areas at all points along the length of the shock tube results in a simplified model with properly scaled areas, volumes, lengths, masses and

energies. The primary experimental advantage of this approach is simplicity in fabrication and operation. A "lumped area" shock tube will typically combine multiple driver tubes into a single, cylindrical driver. The need to change a single diaphragm between tests and eliminate the need for simultaneous firing of several drivers significantly simplifies the testing process.

Computational models of blast simulators are often developed using this same lumped area approach. The advantages of employing this approach for numerical simulation lie primarily in the reduction of the computational domain from three dimensions to two. This simplification alone can decrease model size and required computational resources by one or more orders of magnitude.

Simplifications of the shock tube geometry make it impossible to experimentally or computationally study some of the multi-dimensional characteristics of the time-dependent flow produced by the simulator. Of particular interest are the interactions between driver flow fields during the time when the shortest drivers are nearly empty, while the longest drivers are still flowing mass into the expansion tunnel at a high rate. The tendency of the flow to diffuse and uniformly fill the expansion tunnel is essential for a high fidelity simulation of an ideal nuclear blast in such a facility. Understanding these aspects of time-dependent flow in multiple driver blast simulators forms the motivation for this study.

By combining the resources of CEG and ARL, it was possible to perform this comprehensive experimental and computational study in a very efficient manner. The use of the SSGG simulator at CEG provided experimental data from a full scale, multiple driver, shock tube facility. The flow uniformity analysis provides insight to the types of flow fields that are likely to be encountered in the LB/TS. The validated 3-D CFD codes used in this study will be applicable to other blast studies involving complex geometries and flow fields.

2. SSGG FACILITY AND FLOW-MAPPING EXPERIMENTS

The SSGG blast simulator is a very large shock tube with seven cylindrical driver tubes feeding into a semi-cylindricial expansion section. Each driver tube has an inside diameter of 1.33 m. Of these seven driver tubes, two are 44 m long, two 26 m long, two 19 m long, and one is 35 m long. At the downstream end of each driver is a converging-diverging nozzle system, each having a throat diameter of 66.5 cm. Positioned within each throat is a diaphragm which is used to initially contain the high pressure air in the driver tubes. These diaphragms are simultaneously ruptured to initiate flow during a test. The driver tubes can be pressurized to a maximum of 80 bars, which is sufficient to produce a peak shock overpressure of 140 kPa in the expansion tunnel. The orientation of the drivers at the upstream end of the expanson section can be seen in Figure 1.

The expansion tunnel is 105 m long and has a width of 12 m at the base and a height of 7.1 m at the center. The test section is that area of the expansion tunnel where articles are placed for blast testing. The test section is 15 m long and its upstream end is 60 m from the beginning of the expansion tunnel. A 30-meter-long target displacement area exists down

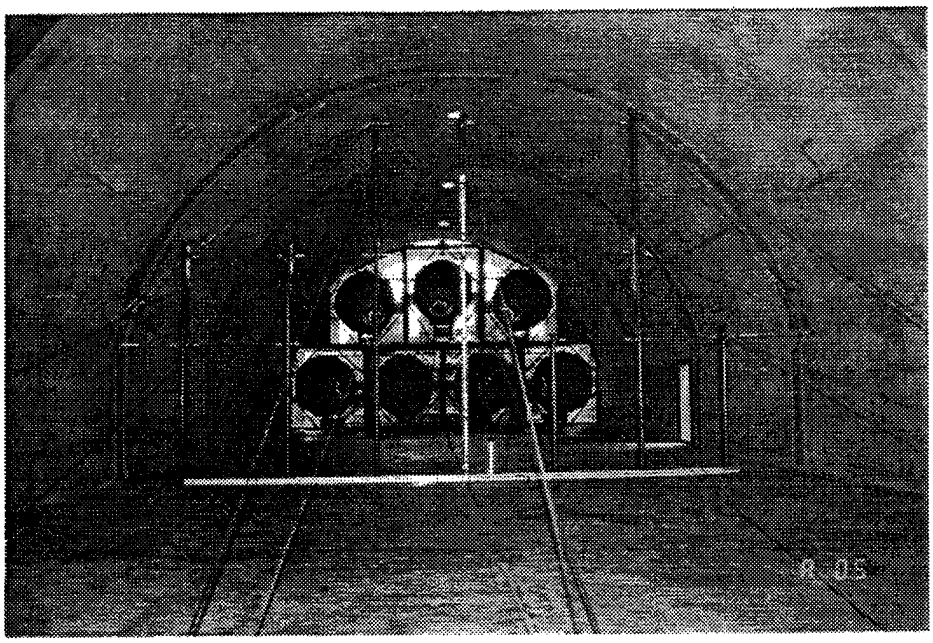

Figure 1. View of Drivers from Inside the Expansion Tunnel.

stream from the test section and extends to the downstream end of the expansion tunnel. At this end of the tunnel is an active rarefaction wave eliminator (RWE) which is used to eliminate flow disturbances that are created when the shock wave arrives at the tunnel exit. Figure 2 shows the RWE as seen from the test section of the SSGG.

Eight experiments were performed in the flow-mapping tests. For the first four shots in the test series, the instrumentation array was positioned at the test section a distance of 67.5 m down stream from the beginning of the expansion section. For the last four tests, the array was placed 22.5 m from the beginning of the expansion section. The initial conditions for the eight tests are outlined in Table 1.

The experimental mapping of time-dependent flow in the SSGG facility was expedited by measuring the flow data at a variety of positions within the expansion tunnel. Figure 3 illustrates the cross-sectional view of the test instrumentation positions in the expansion tunnel that was used for all the tests. The figure shows the locations of the 19 pairs of static and stagnation pressure gauges that were used. It also shows the projection of the exit diameter of the diverging nozzles onto the instrumentation rakes in the expansion tunnel. The SSGG facility has seven drivers, which are distributed symmetrically about the vertical center plane of the expansion tunnel, with one driver split by the center plane. Each of the drivers that feeds into a symmetrical half of the expansion tunnel has a unique length. Static and stagnation pressure gauge pairs were positioned in the expansion tunnel so that three sets of gauges were distributed across the flow path of each unique length driver. For each unique driver length, gauge pairs were positioned on the driver centerline, on the projected outer radius of that driver's diverging nozzle, and half the distance between the centerline and the outer radius of the diverging nozzle. The remaining seven gauge pairs were

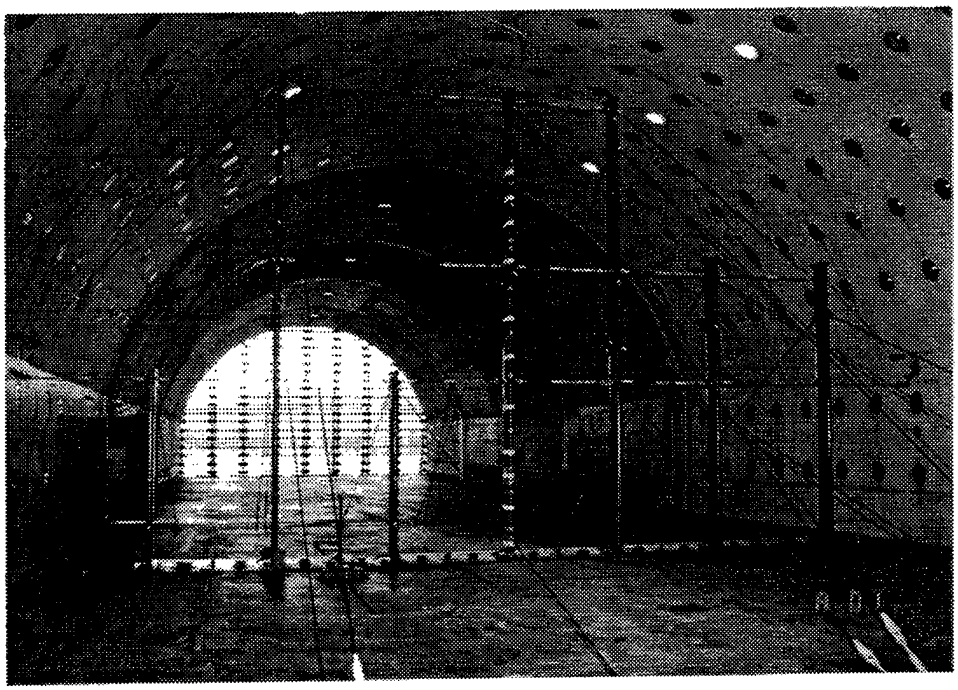

Figure 2. View of Test Section and RWE.

Table 1. Summary of All Tests in the Study.

Test Number	Rake Position (m)	Nominal Shock Overpressure (kPa)	Average Driver Overpressure (bar)	Ambient Pressure (mbar)	Ambient Temperature (°C)	Relative Humidity (percent)
1	67.5	20	7.1	968	11	60
2	67.5	80	36.5	965	7	55
3	67.5	120	60.6	972	6	60
4	67.5	120	61.2	980	1	54
5	22.5	20	7.1	963	4	48
6	22.5	20	7.1	964	2	40
7	22.5	50	20.1	975	8	48
8	22.5	80	36.7	982	7	48

positioned between the projected flow paths of the drivers. The information presented in Figure 3 illustrates which gauge pairs fell within the projected flow path of individual drivers and which gauge pairs fell between drivers. Throughout this report, the **PS** nomenclature denotes a static pressure gauge while a **PB** denotes a stagnation pressure gauge. In both cases, the number following the **PB** or **PS** notation indicates the location of the gauge as shown in Figure 3.

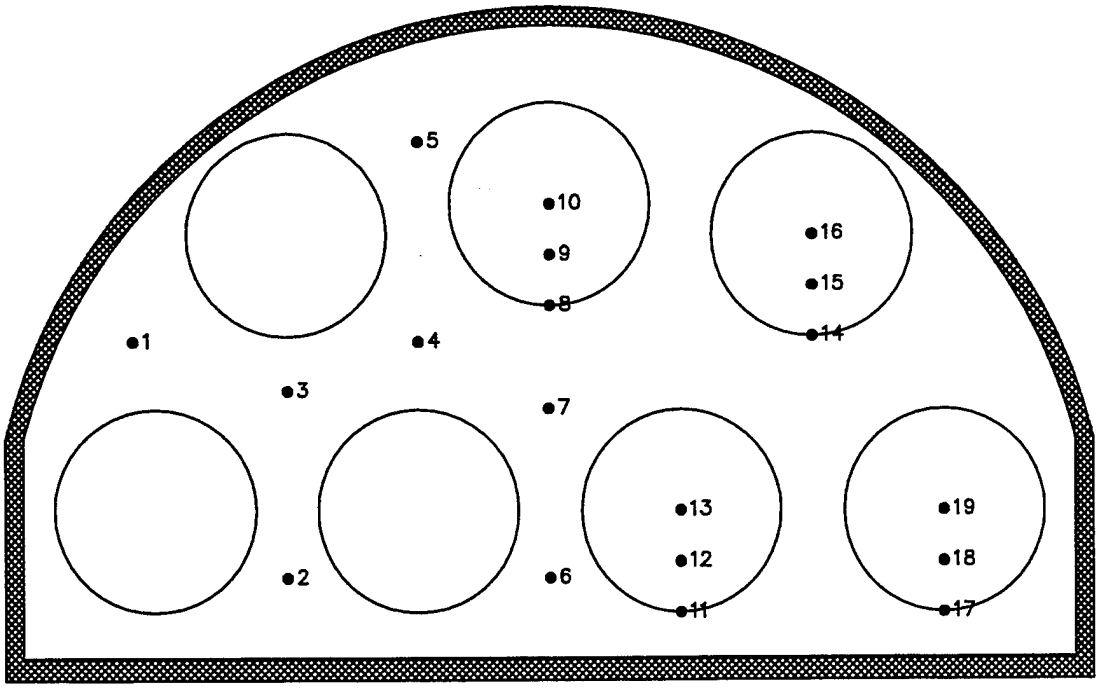

Figure 3. Instrumentation Locations in the Expansion Tunnel Relative to Projected Driver Exit Planes.

3. REDUCTION OF EXPERIMENTAL DATA

CEG provided the raw data on four 2.54-cm magnetic tapes. Four recording stations were used in the original experiments, each with 14 channels of input from the test section. The two types of gauges used to acquire the blast history data were Endevco models 8510B and 8510C pressure transducers. The output of the gauges was conditioned and amplified to a usable voltage level using ANS amplifiers and signal conditioners. The recording instruments used to capture the analog signal were Schlumberger MT5529s.

The data were reduced to engineering units at ARL using a Pacific Instruments data acquisition rack, Honeywell 2.54-cm tape drive, and an IBM-compatible personal computer (PC). The Pacific Instruments data acquisition equipment consisted of a model 9255 amplifier and signal conditioner and a model 9830 digitizer, storing the resultant digital data. The data were then transferred to the PC where software was used to reduce the digital data to engineering units.

Preceding the data on the magnetic tapes for each shot was a calibration step, which was loaded into a calibration segment of the Pacific digitizers. The analog signal of the recorded data was then transferred into the digitizer as if it were an actual test, using a built-in triggering device. The software on the PC downloaded the data and calibration step for each shot, using the information provide by CEG to convert the digitized information into engineering units and save it to a data file for later analysis.

4. DATA ANALYSIS METHOD

Before the test data were analyzed, it was necessary to develop a method of accessing and displaying those results. Consistent usage of a rigorous analytical method would guarantee an unbiased evaluation of all experimental data. Because the primary goal of the project was to study the uniformity of flow at two different axial positions in the expansion tunnel of the SSGG blast simulator, a data analysis methodology was developed in which the flow histories from various points in the expansion tunnel cross section were compared to determine the variation in the flow field at that longitudinal position.

The analysis method for determining flow uniformity employs four different types of pressure-time history comparison:

1. Pressure histories from gauges positioned in the flow path of drivers of different lengths were compared to each other to determine the effects of driver length on the flow in that local region. For instance, referring to Figure 3, the static overpressures recorded in the paths of the driver centerlines could be studied by comparing the data from gauges PS10, PS13, PS16, and PS19. The same could be done for gauges on the outer radius of the diverging nozzle (PS8, PS11, PS14, and PS17) or those between the centerline and outer radius (PS9, PS12, PS15, and PS18).
2. Pressure histories from the seven pairs of gauges positioned between drivers could be compared to each other to determine whether the expansion tunnel walls have a significant influence on the flow characteristics. Stagnation overpressure measurements from gauges PB1 and PB2 may be compared to those from PB4 and PB7 for this purpose.
3. Data obtained from gauges distributed across the radius of a particular driver can be compared to each other to determine the presence of jet flow that may originate from the drivers.
4. Flow histories from gauges within the projected flow paths of drivers could be compared to histories obtained from gauges between drivers to assess the diffusion of the individual driver jets into a single, uniform flow field. Stagnation overpressure data from PB19 and PB10 may be compared to that from PB3 and PB7 for this purpose.

Another method of analyzing the uniformity of the flow fields is to select one flow parameter from each of the 19 gauge locations and view the variation of the parameter in the cross section of the expansion section of the blast simulator. This is performed by making a contour plot of the parameter, which is imposed on the shape of the expansion tunnel. This

method of analysis can be used to determine the uniformity of such flow parameters as peak static overpressure or stagnation overpressure impulse, as two examples.

Of the eight shots that were performed in the test series, four provided a logical set on which to base the flow uniformity analysis. These were tests at two different pressure levels in which the driver initial conditions for shots with the instrumentation array positioned at 22.5 m were nearly the same as the initial conditions of the shots where the array was at the 67.5-m location. A summary of the conditions of these four tests is provided in Table 2. By selecting an appropriate pair of tests with nearly identical initial conditions, it is possible to perform an analysis as if the test data were derived from one shot with one instrumentation array at 22.5 m and another at 67.5 m.

Table 2. Summary of Tests Used in Flow-Mapping Analysis.

Test Number	Rake Position (m)	Nominal Shock Overpressure (kPa)	Average Driver Overpressure (bar)	Ambient Pressure (mbar)	Ambient Temperature (°C)	Relative Humidity (percent)
1	67.5	20	7.09	968	11	60
6	22.5	20	7.06	964	2	40
2	67.5	80	36.46	965	7	55
8	22.5	80	36.66	982	7	48

In this table, the average driver overpressure refers to the fact that the seven drivers of the SSGG are manifolded together to equilibrate the pressure between the driver tubes. The actual pressures for the tests were recorded independently for each driver tube and differed slightly from one driver to the next. The values listed in Table 2 are the mean overpressures of all seven drivers for each test.

The nominal shock overpressure refers to the approximate incident static overpressure produced in the expansion tunnel by the blast. The actual peak static overpressure may not be exactly 20 kPa and may even vary from one location to the next in the expansion tunnel. The nominal shock overpressure is used here as a means of identifying the tests by a significant flow characteristic, rather than a test number.

This table illustrates that the results of Tests 1 and 6 can be combined to analyze the flow associated with a shot having a peak static overpressure of 20 kPa. Similarly, the results of Tests 2 and 8 can be used for the analysis of an 80-kPa shot.

5. ANALYSIS OF 20-kPa TESTS

The flow uniformity analysis was performed by beginning with the lowest overpressure tests and finishing with the high overpressure tests. For each of the two overpressure levels presented here, the data collected at the 67.5-m position are addressed first, followed by those of the 22.5-m position. For the 20-kPa tests, Test 1 had the instrumentation array

positioned at the 67.5-m position, while the data from Test 6 were collected at the 22.5-m position.

The results of the tests are presented in a manner that is consistent with the analysis method discussed previously. If any non-uniformity exists in the flow field, it is expected to be caused by persistent jets of driver gas traveling down stream. One would expect the strongest area of such flow to exist at the center of the jet. It is with this understanding that the flow uniformity analysis begins by comparing the measured flow histories from gauges positioned in the flow path of driver centerlines.

Figure 4 compares the early time static overpressure waveforms from Test 1 for gauges positioned in the flow path of the centerlines of the 26-m driver, the 35-m driver, and the 44-m driver: gauges PS16, PS10, and PS19, respectively, from Figure 3. This figure shows that, of these three waveforms, PS19 has the greatest peak static overpressure at 23.45 kPa. The lowest of the three peak static overpressures occurred at gauge PS10, in the centerline of the 35-m driver and was 21.96 kPa. The variation between these two peaks is 1.49 kPa or 6.6%. Figure 5 shows the full positive phase duration of the static overpressure of these same three gauges. This figure shows that the static overpressure of the flow in the path of the driver centerlines is uniform.

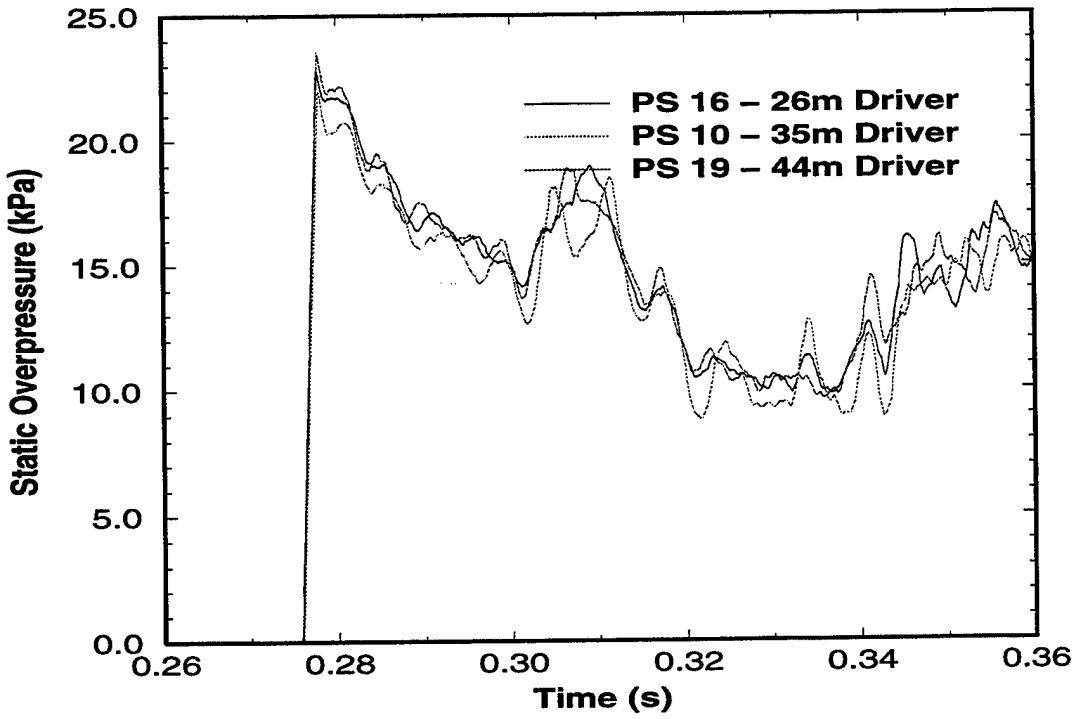

Figure 4. Test 1 Static Overpressure from Gauges in the Flow Path of Driver Centerlines (early time history).

Figures 6 and 7 provide an illustration of Test 1 data from the same driver centerlines as Figures 4 and 5 except that in these figures, stagnation overpressure is plotted instead of static overpressure. Figure 6 shows an early time history in which the peak stagnation overpressure occurred in the centerline of the 35-m driver (gauge PB10) and was 27.90 kPa.

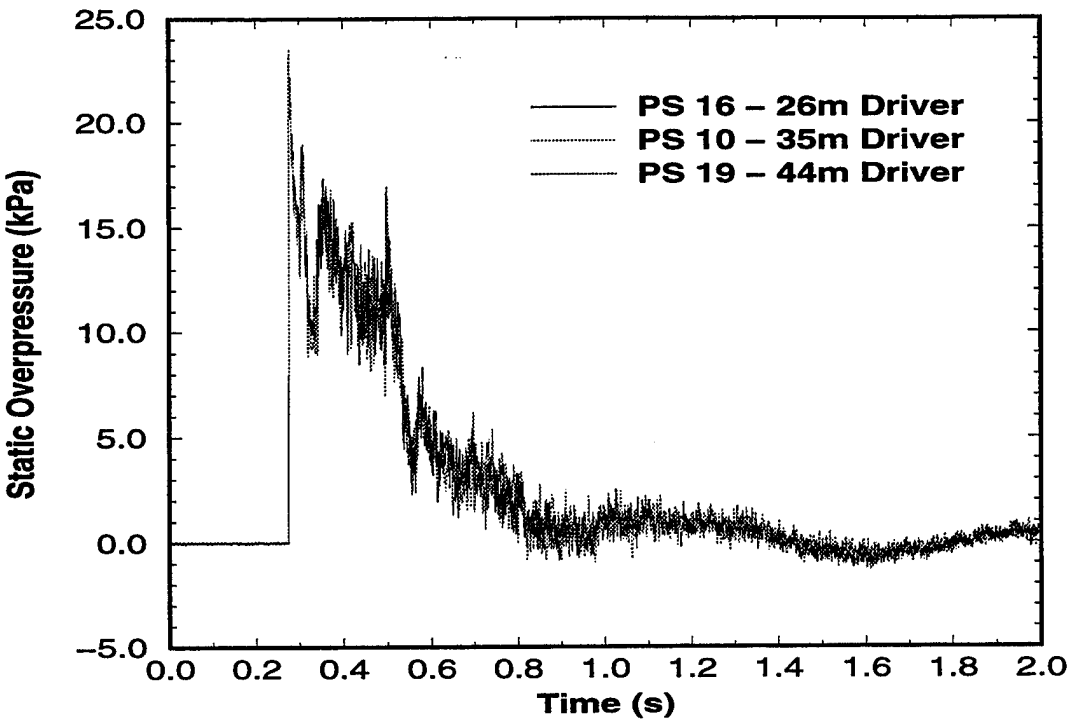

Figure 5. Test 1 Static Overpressure from Gauges in the Flow Path of Driver Centerlines.

The smallest of the three stagnation overpressure peaks occurred in the centerline of the 26-m driver (gauge PB16) and was 24.63 kPa. The difference between this local maximum and minimum is 3.27 kPa or 12.4%. Figure 7 provides the same full positive phase duration of these three centerline gauges and proves that, like that static overpressure, the stagnation overpressures are nearly identical.

If the driver gas flow were to produce persistent jets that travel down stream in the expansion section, then a shear surface would be produced at the interface between the driver jet and the tunnel gas. Jet flow from shock tubes has been observed to maintain the shape of the exit plane in testing at ARL.[8] In the case of the SSGG large blast simulator, jet flow exiting one of the drivers would be expected to take the size and shape of the exit planes of the diverging nozzles that empty into the expansion section. Thus, it may be possible to determine the presence or absence of driver jet flow at a given longitudinal position by comparing the static and stagnation overpressures of gauges positioned in the path of the outer radius of the diverging nozzles. Test 1 had the instrumentation array positioned at the 67.5-m position in the expansion tunnel. Test 1 static overpressure data from gauges positioned in the path of the outer radius of the diverging nozzles are presented in Figure 8. The records represented in this figure are from gauges PS14, PS8, and PS17 which lie on the nozzle exit radius of the 26-m driver, 35-m driver, and 44-m driver, respectively. These results show that, like the flow in the driver centerline paths, the static overpressure is uniform at these gauges. Figure 9 is a plot of the stagnation overpressure histories from these same three gauges in the path of the nozzle exit radius. Again, these results show no significant difference between the recordings of the subject gauges. These results clearly

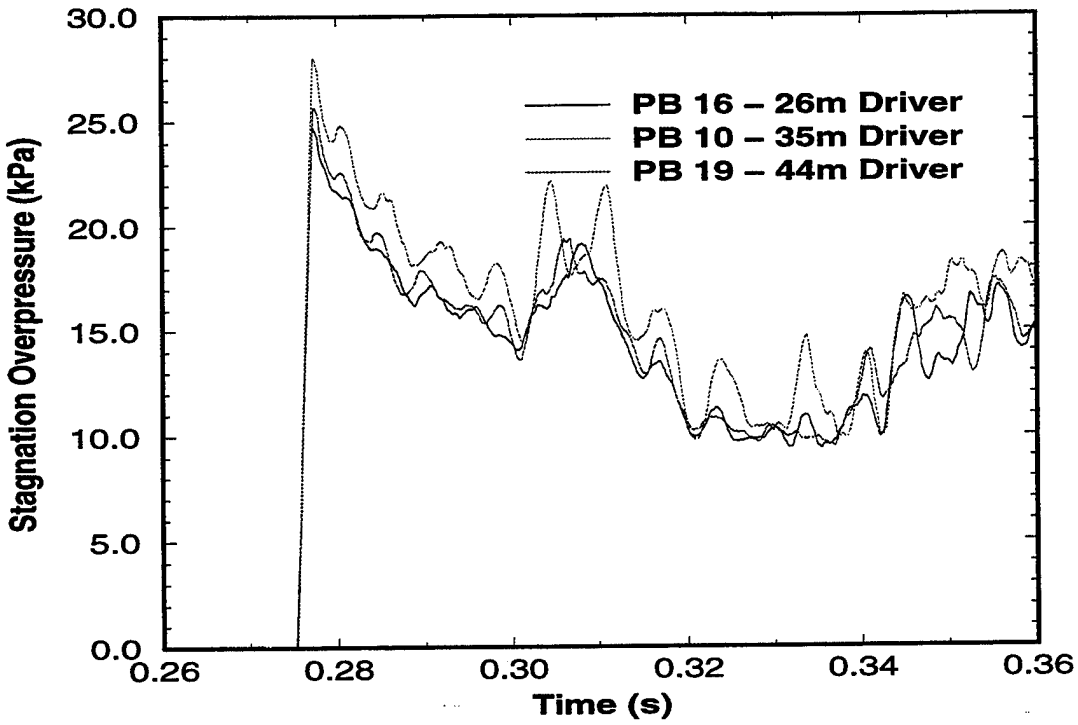

Figure 6. Test 1 Stagnation Overpressure from Gauges in the Flow Path of Driver Centerlines (early time history).

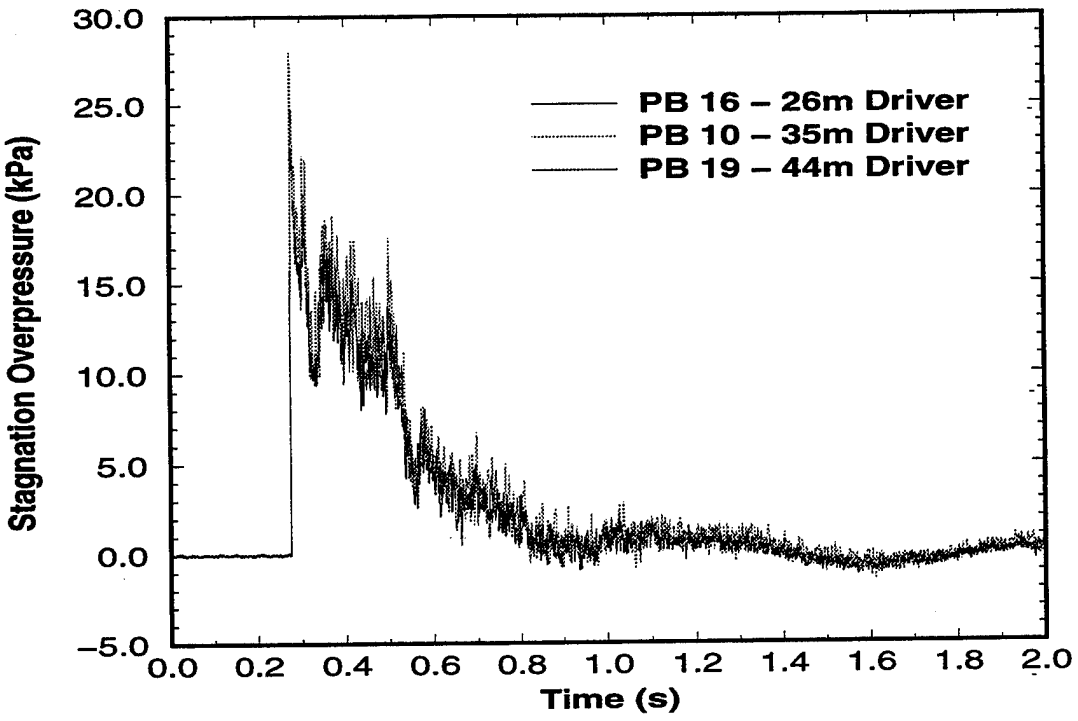

Figure 7. Test 1 Stagnation Overpressure from Gauges in the Flow Path of Driver Centerlines.

demonstrate that there is no evidence of driver jet flow at the 67.5-m test section for tests at the 20 kPa overpressure level.

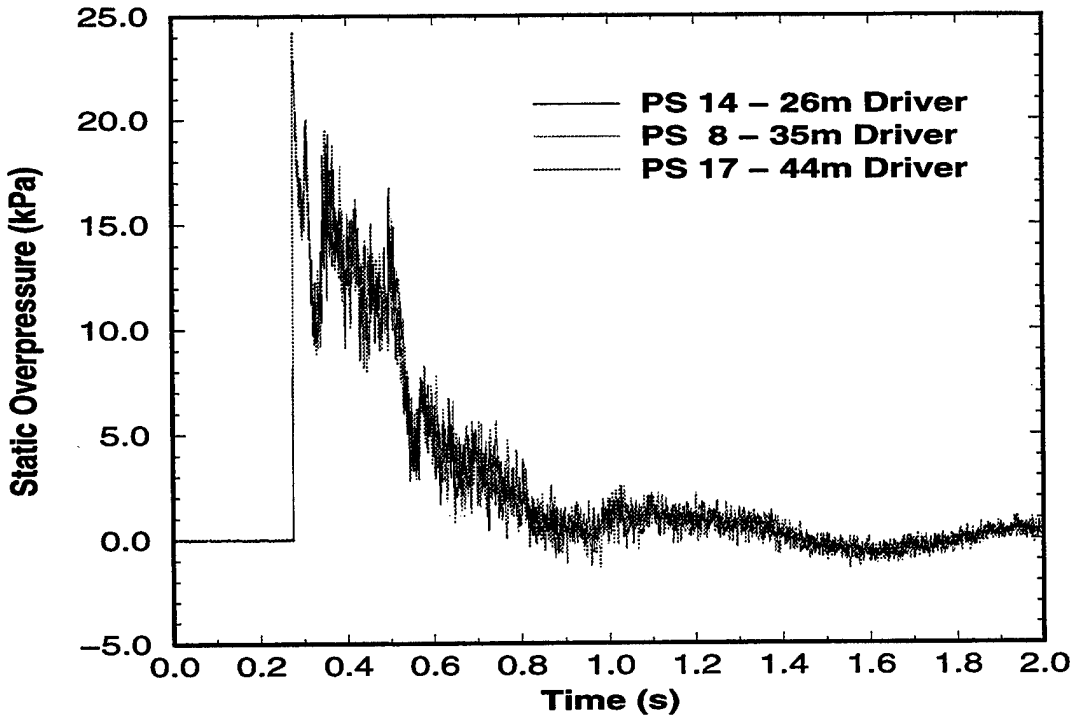

Figure 8. Test 1 Static Overpressure from Gauges in the Flow Path of the Outer Radius of Driver Diverging Nozzles.

It has been shown that the flow in the paths of the drivers is uniform across different driver lengths. The next step in the analysis is to examine the flow recorded at gauges positioned between the flow paths of the drivers. This analysis will determine the ability of the driver gas to uniformly fill the entire cross-sectional area of the expansion section. Figure 10 provides an early time history of the static overpressure waveforms from gauges PS1, PS2, PS5, and PS6 of Test 1. The illustration of Figure 3 shows that each of these records falls between the flow paths of different length drivers and is recorded by gauges that are close to the walls of the expansion tunnel. The peak static overpressures in Figure 10 are bracketed by the gauges PS6 and PS1. Gauge PS6 has the greatest static overpressure of the four at 23.74 kPa and PS1 has the lowest at 23.01 kPa, a difference of 0.73 kPa or 3.1%. While not shown in the figure, the full positive phase static overpressure waveforms of these four gauges are once again nearly identical. The stagnation overpressure from these same gauge locations are plotted in Figure 11, which also shows no significant difference between the four records. These two figures indicate that, at the 20-kPa overpressure level, the flow from the drivers is able to sufficiently diffuse to uniformly fill the expansion tunnel at the 67.5-m test section.

From these many comparisons, one can confidently conclude that the flow at the 67.5-m position, the test section in the SSGG, is highly uniform at the 20-kPa overpressure level. Consequently, it can be expected that targets will be uniformly loaded in both shock

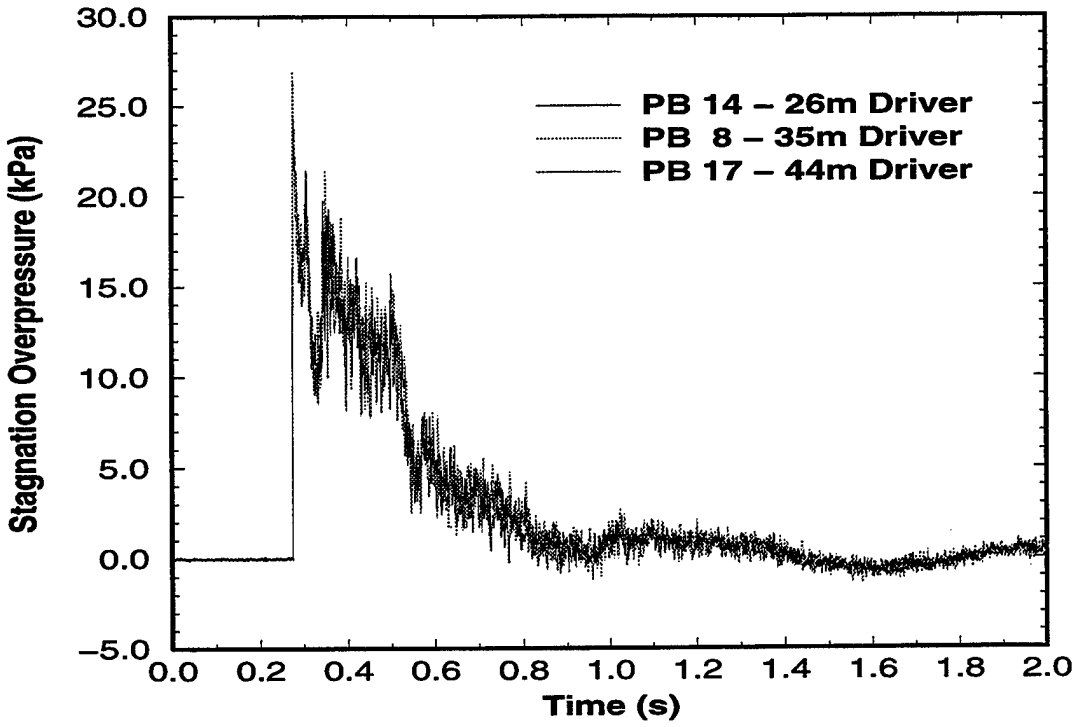

Figure 9. Test 1 Stagnation Overpressure from Gauges in the Flow Path of the Outer Radius of Driver Diverging Nozzles.

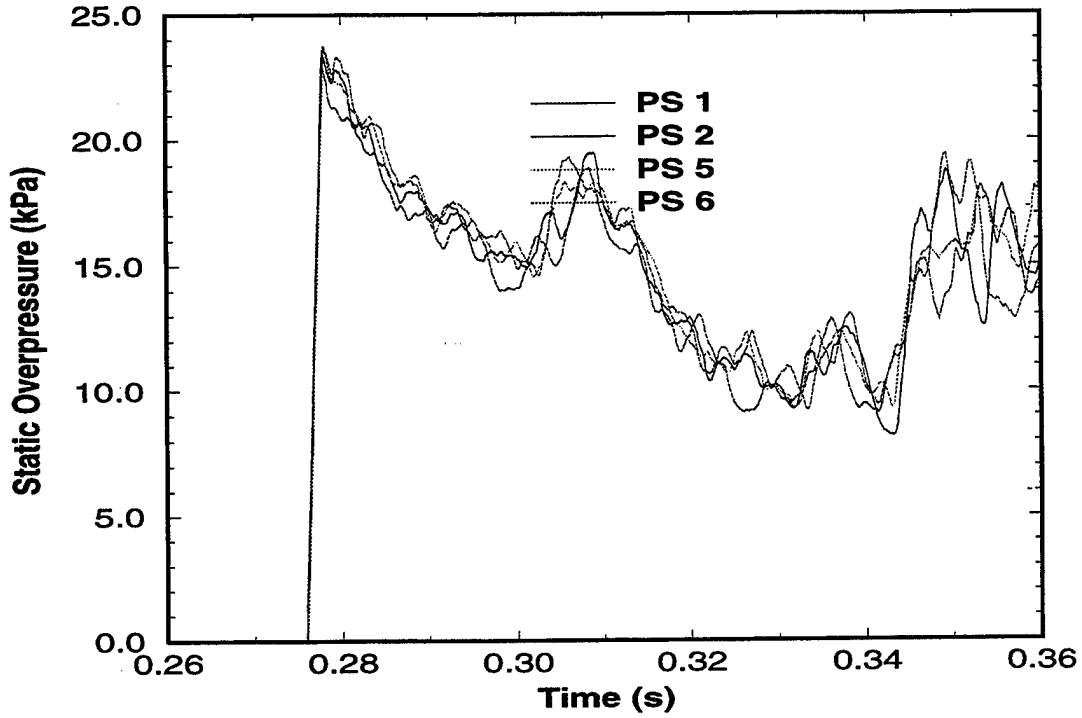

Figure 10. Test 1 Static Overpressure from Gauges Between Drivers.

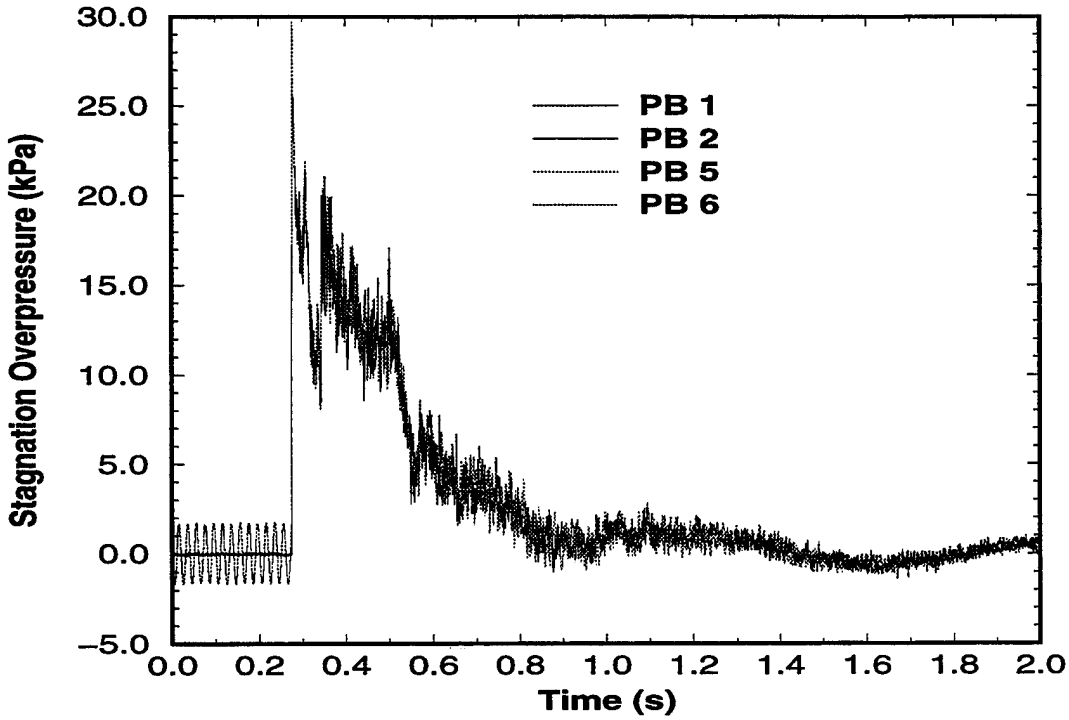

Figure 11. Test 1 Stagnation Overpressure from Gauges in Between Drivers.

diffraction and drag loading when placed in the test section of the SSGG for a test at this overpressure level.

Test 6 was the 20-kPa overpressure test in which the instrumentation array was positioned 22.5 m down stream from the beginning of the expansion section. To provide a self-consistent set of results of these shots, the Test 6 data are presented in nearly the same format as those of Test 1. Figure 12 shows an early time history of the static overpressure records taken from the gauges in the path of the driver centerlines (PS13, PS16, PS10, and PS19). In this figure, the gauge PS13 has the largest peak static overpressure at 28.13 kPa, while gauge PS10 had the lowest of the four at 26.61 kPa, a difference of 1.52 kPa or 5.6%. For the remainder of the positive phase (not shown in the figure), the four records are nearly coincidental. Figure 13 shows the stagnation overpressure from the same four gauge locations. This figure provides the first indication of any nonuniformity of the flow in the expansion tunnel. The stagnation overpressure records follow the same pattern until about 530 ms where the PB19 record suddenly increases and remains at an elevated level of approximately 10 kPa for the remainder of the positive phase. The gauge PB19 is in the path of the centerline of the 44-m driver, the longest driver in the SSGG facility. This result is an indication that the gas exiting this driver may be forming a jet flow in the expansion tunnel.

To further investigate the possible driver jet flow phenomenon illustrated in Figure 13, the records from the gauges positioned in the path of the outer radius of the diverging nozzles are examined. Figure 14 illustrates the static overpressure records from gauges PS11, PS14, PS8, and PS17, which are aligned with the nozzle exit radii. This figure shows that the static overpressure is again uniform across the different drivers. Figure 15, however, shows

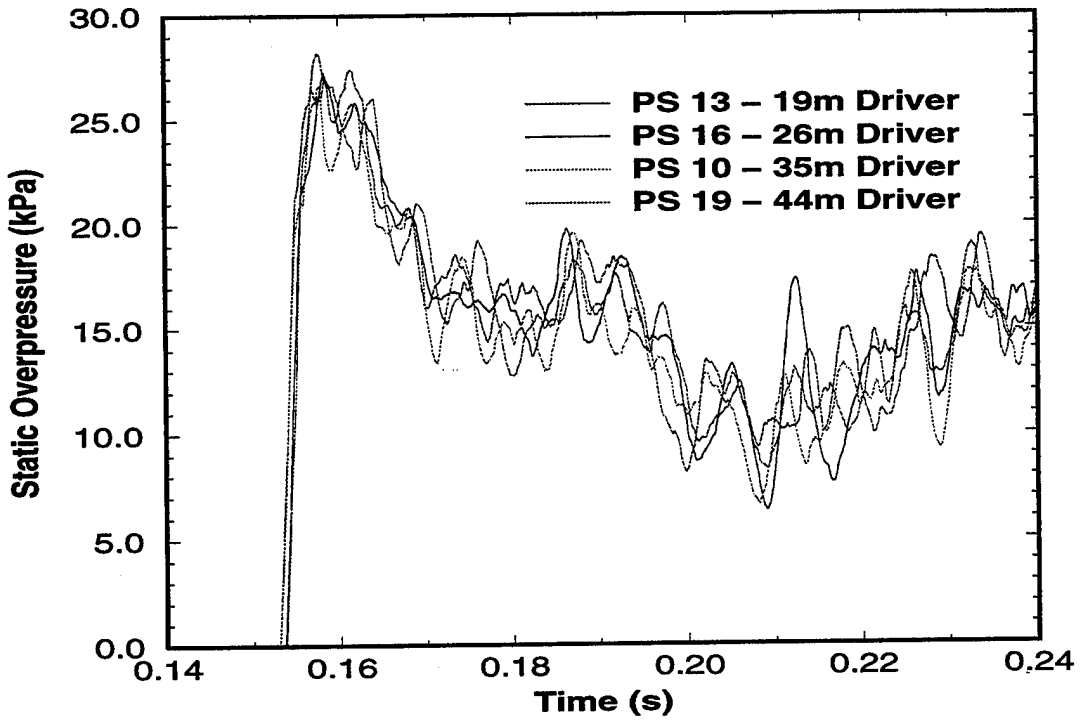

Figure 12. Test 6 Static Overpressure from Gauges in the Flow Path of Driver Centerlines.

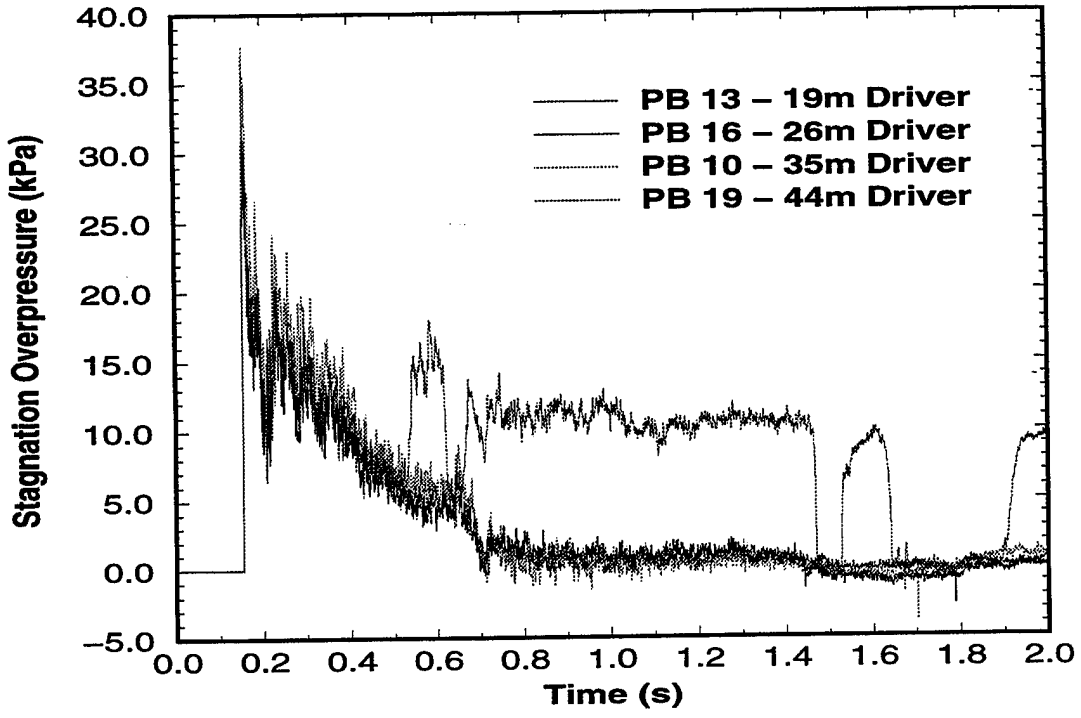

Figure 13. Test 6 Stagnation Overpressure from Gauges in the Flow Path of Driver Centerlines.

that the stagnation overpressure from these gauge positions is uniform for only three of the four. The PB17 record, aligned with the 44-m driver, has a much lower value than the rest from 180 ms until 650 ms.

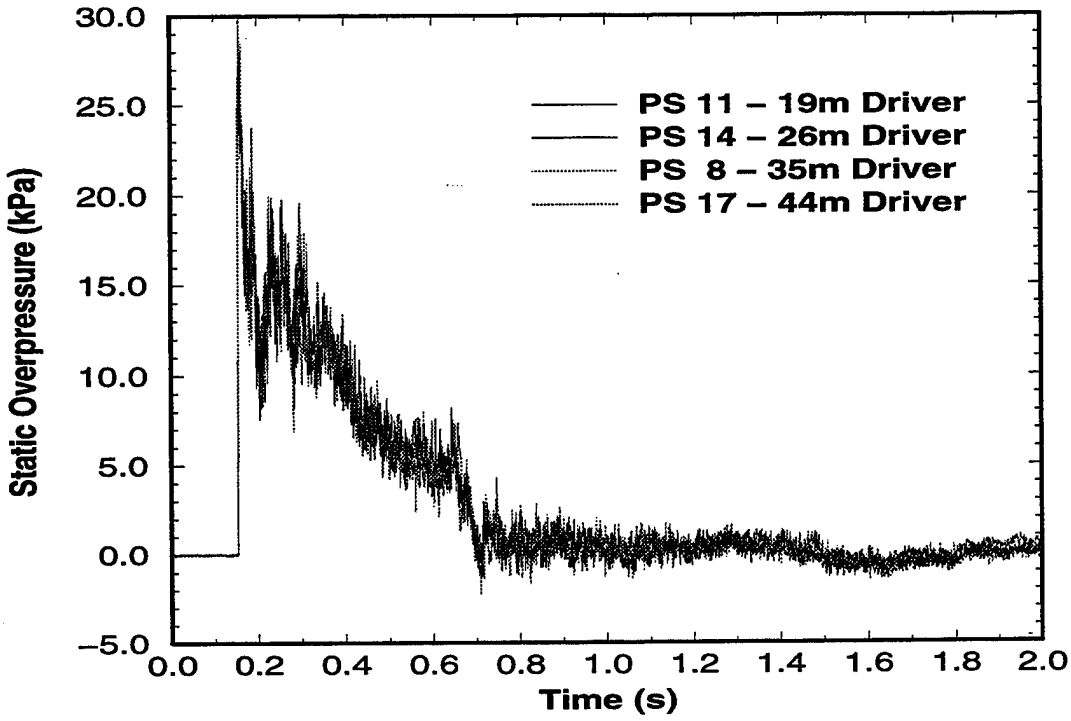

Figure 14. Test 6 Static Overpressure from Gauges in the Flow Path of the Outer Radius of Driver Diverging Nozzles.

To gain a better understanding of the flow from the 44-m driver, records from the gauges distributed across the radius of that driver were compared. Figure 16 provides the comparison of the stagnation overpressures measured in the path of the driver centerline (PB17), the nozzle exit radius (PB19), and half the distance between these two points at the nozzle half radius (PB18). This figure clearly shows the formation of jet flow from the 44-m driver. The jet appears to be concentrated in an area that is smaller than the radius of the nozzle exit. This is evidenced by the very high stagnation overpressure in the path of the driver centerline and a very low stagnation overpressure for much of the PB17 record which is aligned with the nozzle exit radius. The PB18 record on the nozzle half radius initially follows the centerline record of PB19, then diverges from it at about 540 ms to eventually coincide with the PB17 record at about 710 ms. These results are evidence that flow separation is occurring as the gas transitions from the throat section to the diverging nozzle. This separated flow then forms the jet which retains its shape for some distance as it travels down stream and passes the 22.5-m instrumentation array.

This type of jet flow is consistent in character to that observed during testing of the ARL 10.2-cm shock tube.[8] This device was constructed to perform research in the use of shock tube exit jets for the simulation of thermally precursed, non-ideal blast produced by tactical nuclear weapons.[9, 10] A photograph of the 10.2-cm shock tube is provided in Figure 17.

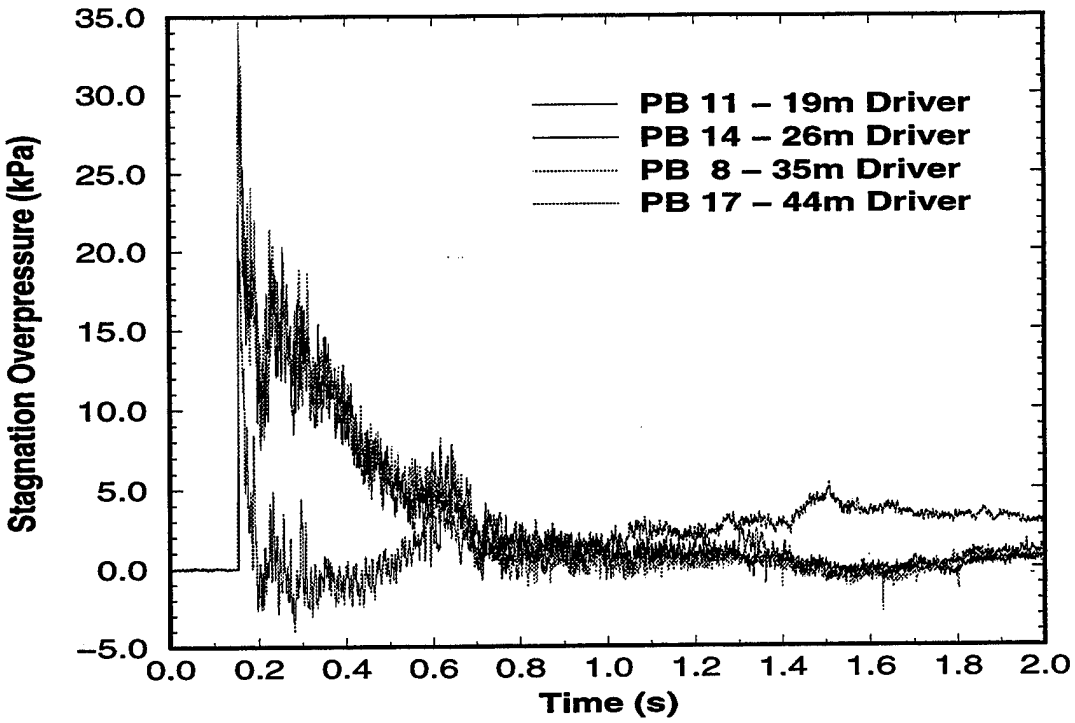

Figure 15. Test 6 Stagnation Overpressure from Gauges in the Flow Path of the Outer Radius of Driver Diverging Nozzles.

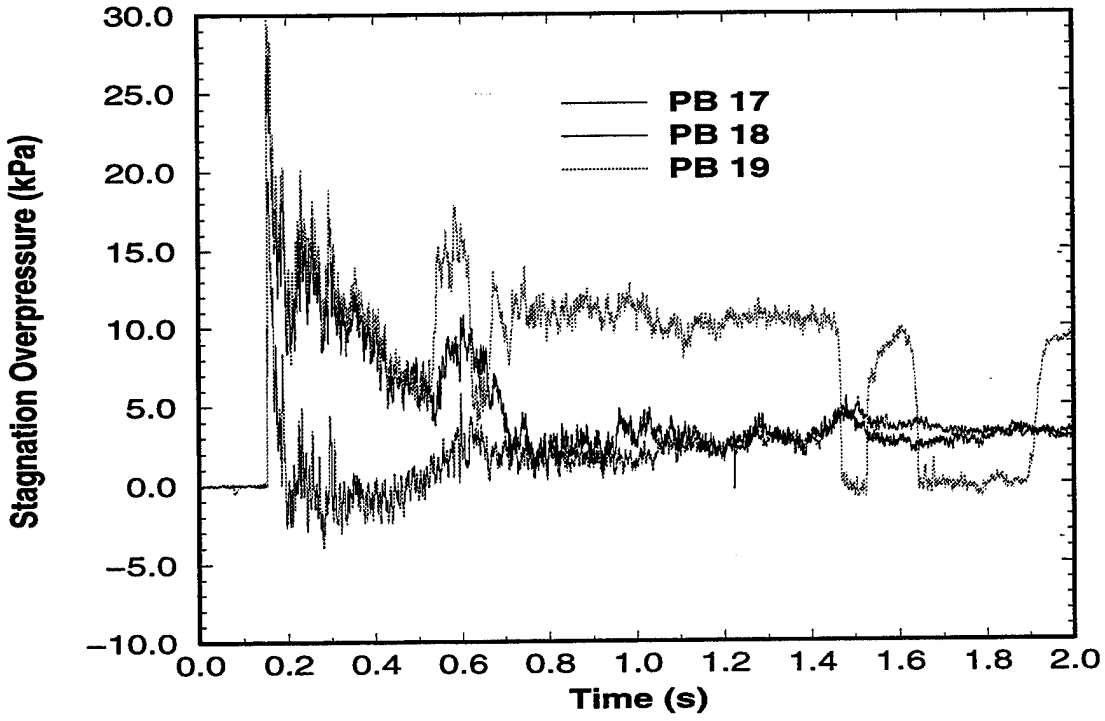

Figure 16. Test 6 Stagnation Overpressure from Gauges Across the Radius of the 44-m Driver.

This photograph was taken from the downstream end of the expansion section and shows the exit plane of the shock tube. Down stream from the shock tube exit plane there is an instrumentation rake that contains a vertical set of differential pressure gauges[11] that are used to measure the characteristics of the flow exiting the tube. In the test configuration of the 10.2-cm shock tube, differential pressure measurements were made in the path of the shock tube centerline, on the exit plane outer radius, and at the half-radius point, in addition to several other vertical locations. Differential pressure time histories from a test of this facility[12]are provided in Figure 18. This figure shows flow that has similar characteristics to those measured in the path of the SSGG 44-m driver. The data from the gauge aligned with the shock tube centerline are at all times greater than those recorded elsewhere. The differential pressure on the exit radius is always the smallest, and the half-radius data fall in between the other two.

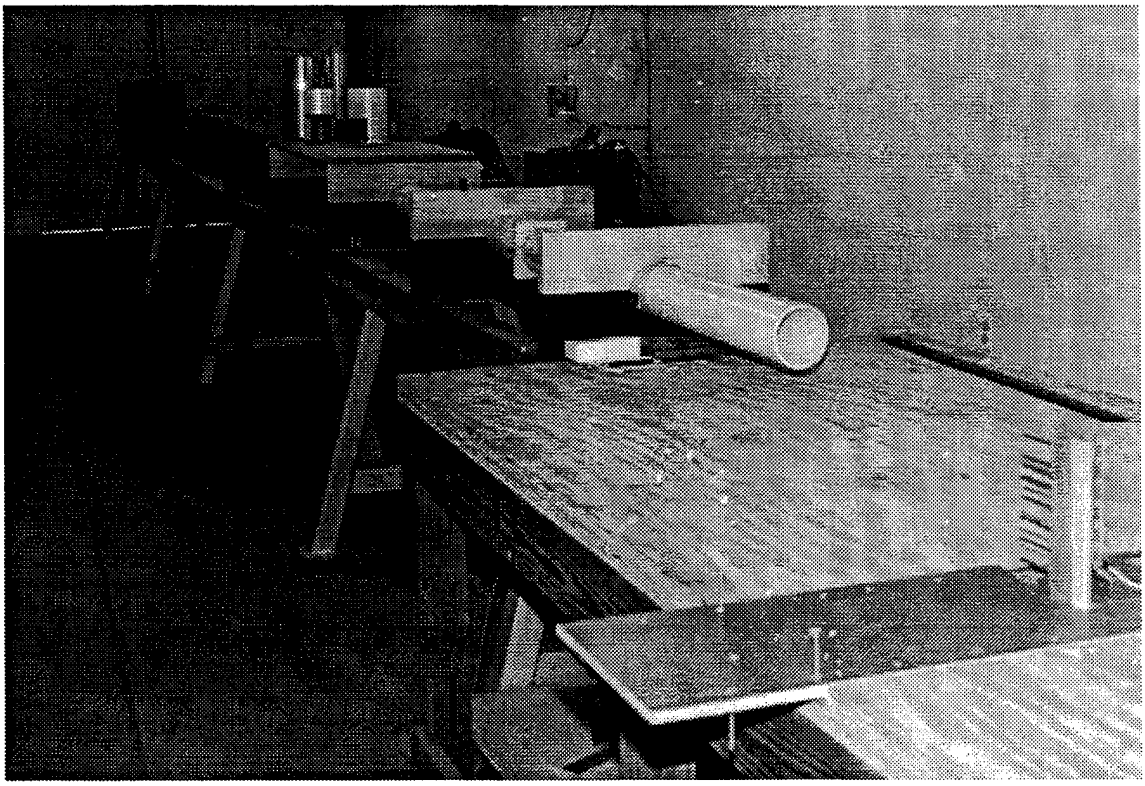

Figure 17. ARL 10.2-cm Shock Tube.

These results are clear evidence that driver jet flow does exist in the upstream end of the SSGG expansion tunnel at the 20-kPa overpressure level. However, this phenomenon was only found in the path of the longest driver. The other shorter drivers produced no noticeable jet flow at this shock overpressure level. It is also important to reiterate that, even though some shear flow was found at the 22.5-m position, the flow at the 67.5-m vehicle test station was completely uniform in static and stagnation overpressure. The flow travel distance in the expansion tunnel from the 22.5-m position to the 67.5-m position is sufficient for any driver jet flow produced at this overpressure level to diffuse and form a flow field which is essentially one-dimensional at the test section.

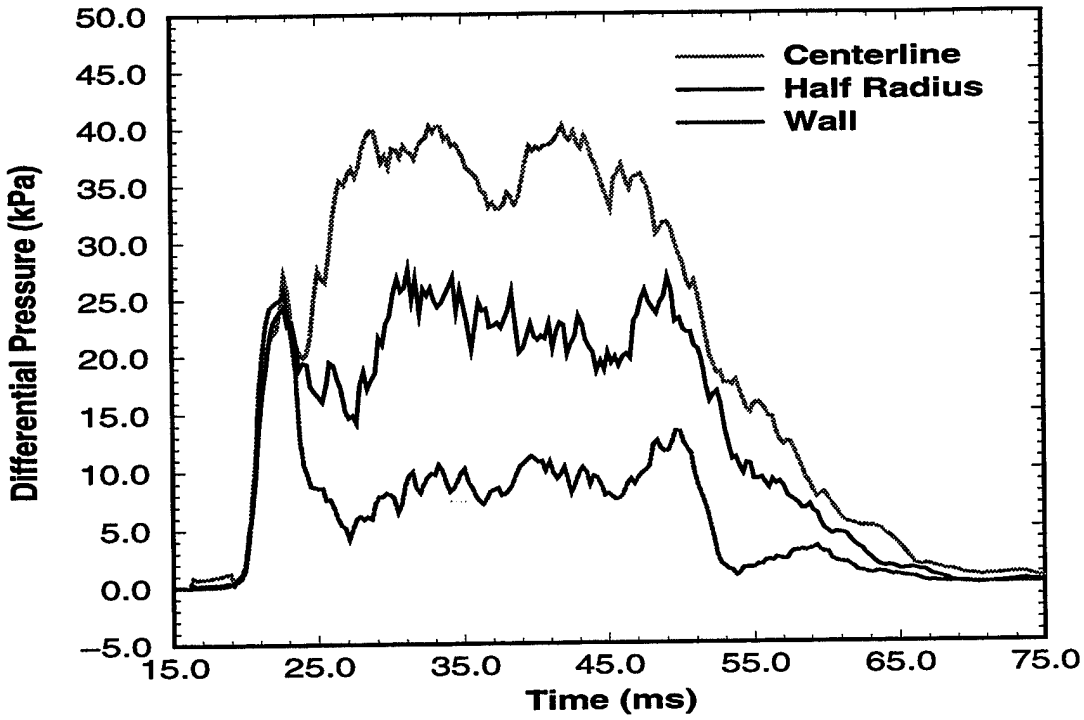

Figure 18. Differential Pressure Histories Across the Radius of the ARL 10.2-cm Shock Tube.

6. ANALYSIS OF 80-kPa TESTS

Tests 2 and 8 were shots in which a nominal peak static overpressure of 80 kPa was produced in the expansion section. Test 2 had the instrumentation array positioned at the 67.5-m location. The early time history of the static overpressure recorded on the gauges in the path of the driver centerlines is presented in Figure 19. The greatest of these four static overpressures was measured on gauges PS13 and PS19 at 77.9 kPa, while the lowest of the four peaks occurred on gauge PS10 at 73.9 kPa. The difference between these peak static overpressures is 8.00 kPa or 10.8%. For the remainder of the positive phase, the static overpressures of the four records closely agree. Based on this agreement and that of the prior discussion, it is possible at this point in the analysis to declare the static overpressure to be uniform across a particular cross section in the expansion tunnel an any point in time during the blast event. Using this conclusion, the remainder of the flow uniformity will concentrate on variations that may exist in the stagnation overpressure records.

The Test 2 stagnation overpressure records from the gauges in the paths of the driver centerlines are presented in Figure 20. The most significant characteristic of these records is the dropout of the PB16 record at 1.0 s. At this point in time, the data from that gauge dropped out of the range of physically realistic values and did not recover during the remainder of the positive phase. Also important in this figure is the dropout of the data from gauge PB19 at about 1.1 s, which soon returns and again follows the remainder of the traces.

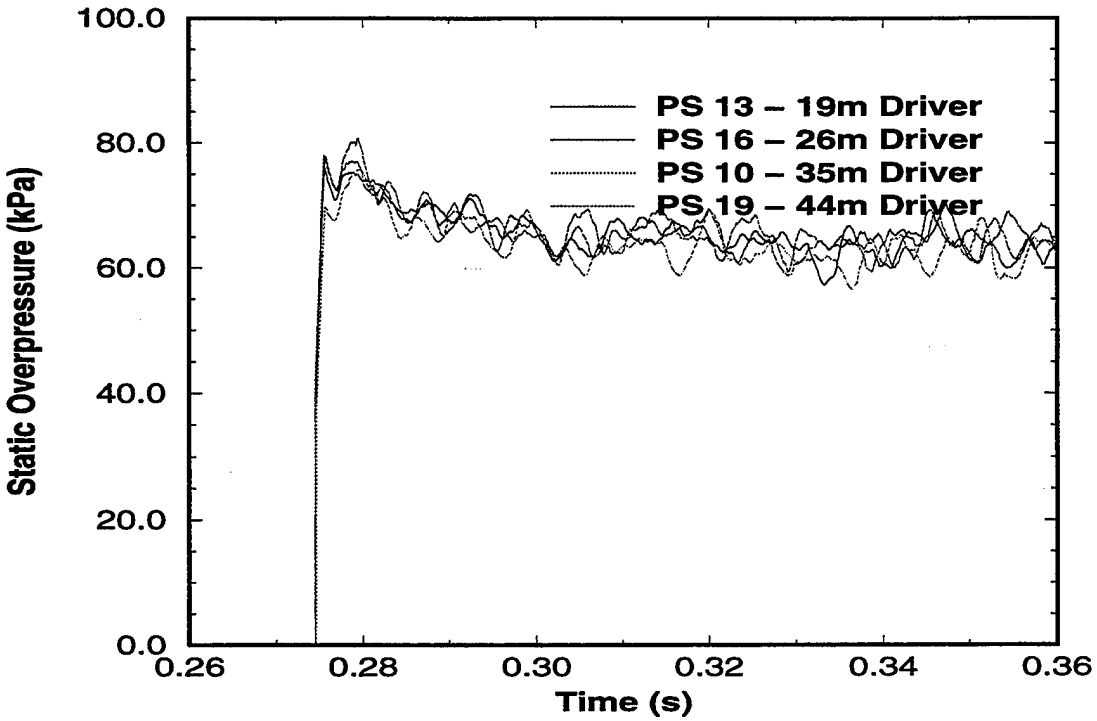

Figure 19. Test 2 Static Overpressure from Gauges in the Flow Path of Driver Centerlines (early time history).

A possible explanation of the reason for these dropouts in these records lies in the configuration of the SSGG blast simulator. The seven drivers and their associated converging/diverging systems are evenly distributed across the diameter of the expansion section of the facility. The reaction pier and other structural supports hold the driver system in place. The transition region between the diverging nozzles and the expansion tunnel is not sealed. As a result, the shock wave propagation down the expansion tunnel can create a low pressure region at the upstream end of the tunnel, which will cause ambient air to be entrained in the flow field. Table 2 shows that when these tests were performed, the ambient air was cold and damp. The driver gas is atmospheric air which is run through compressors to pressurize the drivers. At the time the flow is initiated, the driver air is at the same temperature as the surrounding atmosphere. When flow is initiated, the driver gas expands through the diverging nozzles and cools. It is believed that the expanded driver gas cooled the entrained ambient air and caused small ice particles to form in the flow. These ice particles are believed to have clogged the stagnation pressure gauges and to have caused the dropouts observed in Figure 20.

The stagnation overpressure records in Figure 20 show that there are slight variations between the different records at several points in time during the positive phase. For instance, at 450 ms, gauge PB16 recorded a stagnation overpressure of about 61 kPa, while gauge PB10 simultaneously recorded a level of about 78 kPa. To better quantify these variations, these traces were numerically integrated to produce stagnation overpressure impulse histories. Figure 21 is a plot of these four impulse histories from Test 2. In this figure, one can see the

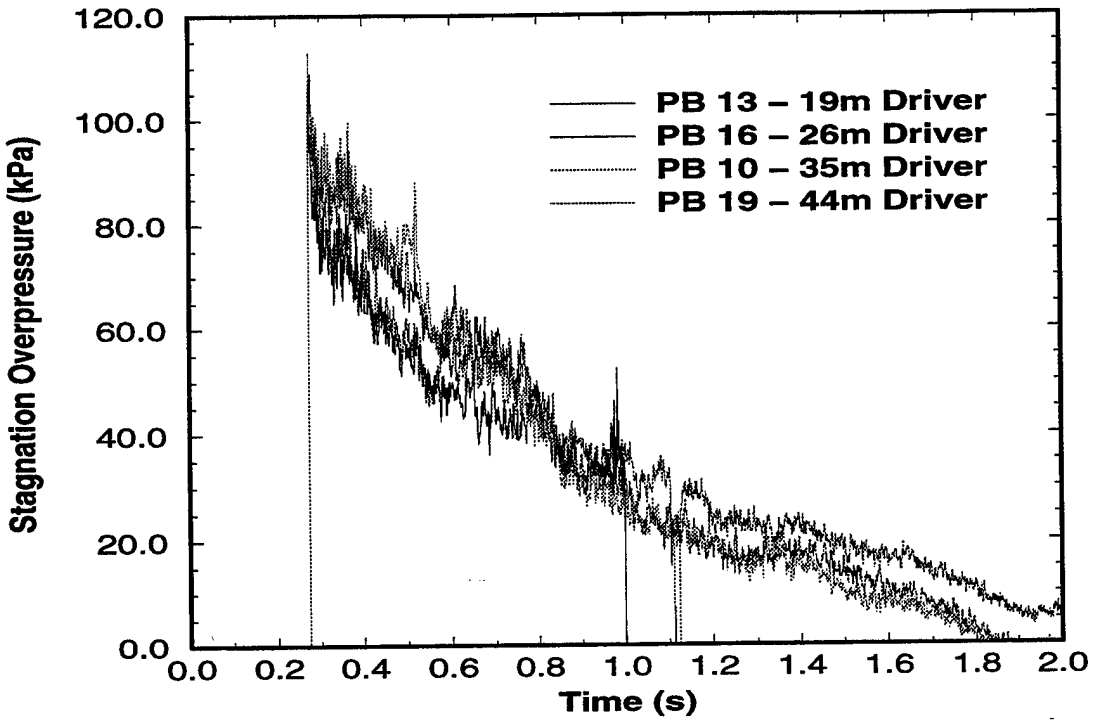

Figure 20. Test 2 Stagnation Overpressure from Gauges in the Flow Path of Driver Centerlines.

point at which gauge PB16 completely dropped out and also the step in the PB19 record denoting the brief dropout that it experienced. Despite these dropouts, one can see that the stagnation overpressure impulse histories of these four gauges closely followed each other. The integrated impulse values at 2.0 s range from 57.5 kPa-s for PB19 to 53.4 kPa-s for gauge PB10, a spread of 7.4%. The Test 2 stagnation overpressure histories from gauges between drivers are presented in Figure 22. This figure again illustrates nearly coincidental records produced by gauges in these positions. The average stagnation overpressure impulse at 2 s from these three gauges was 52.2 kPa-s. The consistency of the recorded stagnation overpressure impulse for these gauges distributed about the cross section of the expansion tunnel, along with the nearly coincidental static overpressure histories, is a clear indication of a uniform flow field being produced at the 67.5-m test section for the 80-kPa overpressure level.

Finally, Test 8 was the 80-kPa overpressure shot in which the instrumentation array was positioned at the 22.5-m longitudinal position in the expansion section. This was the highest overpressure test performed with the instrumentation placed at this position. This test provides a very informative view at the driver gas flow at this high overpressure level. Figure 23 compares the stagnation overpressures from the gauges in the path of the driver centerlines. This figure shows that the four records follow nearly the same path from the time of shock arrival at 175 ms until about 220 ms, at which time, large oscillations in all four records exist. This period of disturbance lasts until about 800 ms, after which, the four histories follow approximately the same pattern. The large oscillations in the flow occur

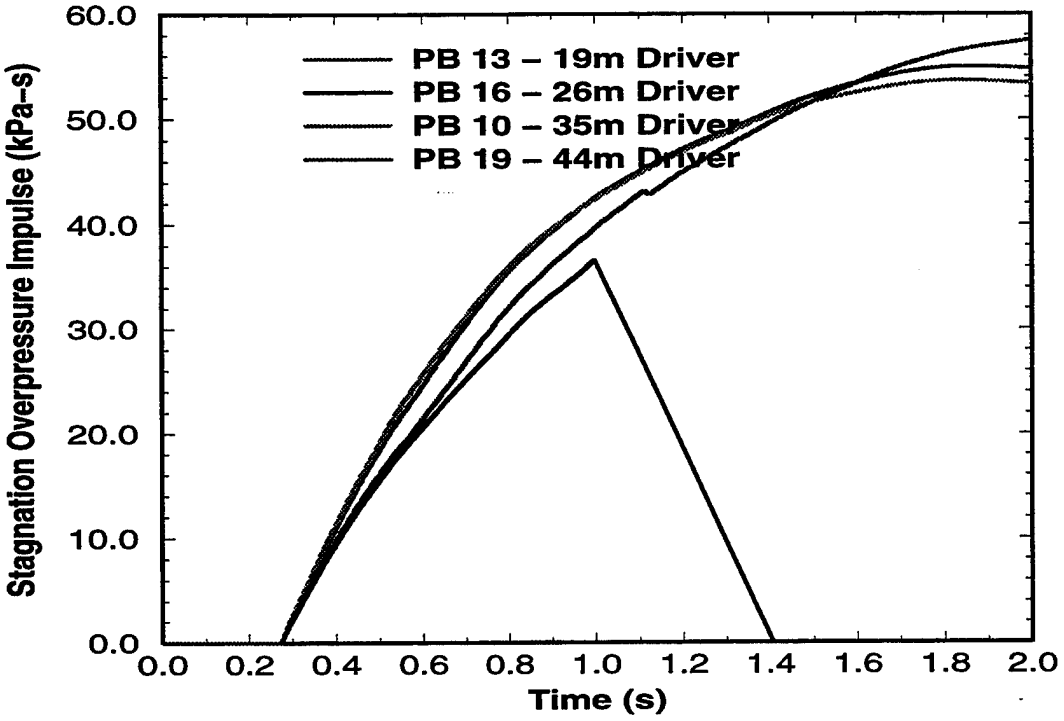

Figure 21. Test 2 Stagnation Overpressure Impulse from Gauges in the Flow Path of Driver Centerlines.

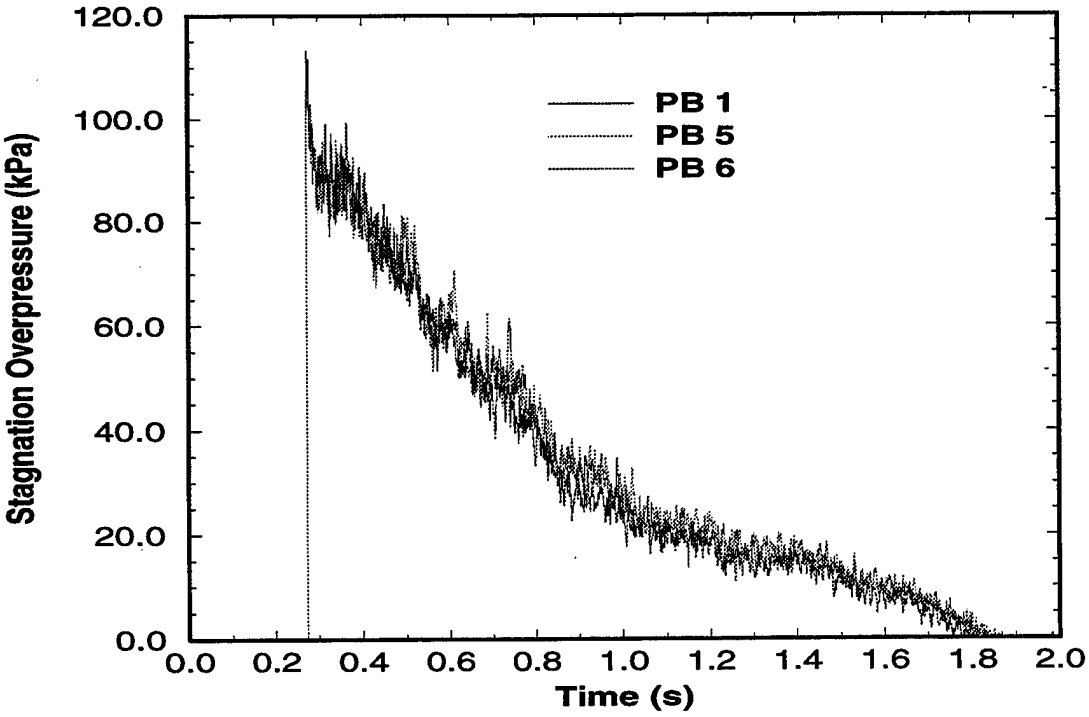

Figure 22. Test 2 Stagnation Overpressure from Gauges Between Drivers.

when the driver gas arrives at the measurement position. The shear stress produced by the interaction of the driver gas jet with the tunnel air generates a highly turbulent flow field. The turbulent mixing of the driver gas with the tunnel air diffuses the jet and produces the flow disturbances illustrated in Figure 23.

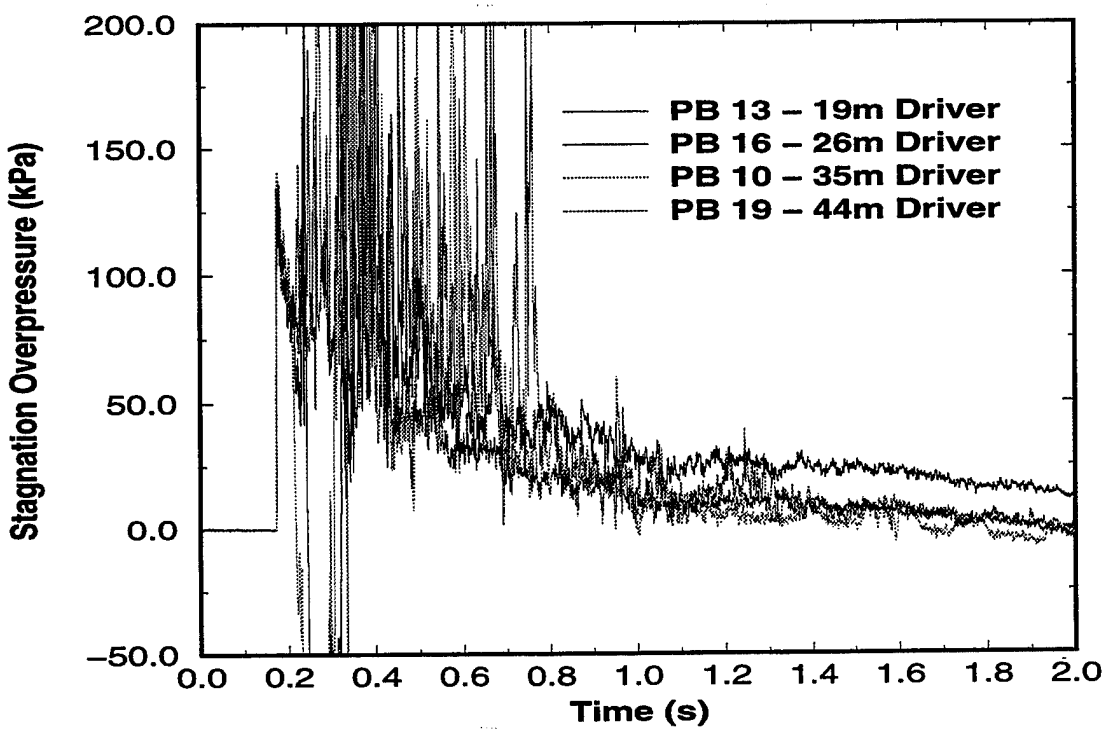

Figure 23. Test 8 Stagnation Overpressure from Gauges in the Flow Path of Driver Centerlines.

Also evident in Figure 23 are dropouts of the records of gauges PB16 and PB10. To better illustrate this phenomenon, the stagnation overpressure histories from these two gauges are plotted together in Figure 24. In this figure, both records experience the dropout at about 230 ms and recover at about 330 ms. Again, this effect is considered to be caused by ice formation on the stagnation probe. It is interesting to note that these dropouts do not occur on gauges PB13 and PB19, which are plotted together in Figure 25. Referring again to Figure 3, one can see that the gauges that experienced the dropouts are positioned in the paths of the 26-m and 35-m drivers that are near the top of the expansion section. The dropouts are not apparent in the records of the gauges in the paths of the drivers that are near the floor of the expansion section.

To further investigate this phenomenon, Figure 26 was produced to compare the stagnation overpressure histories of gauges in the path of the diverging nozzle exit radius for the 26-m and 35-m drivers. This figure shows that, on the same test, these gauges experienced the icing effect at the same point in time. In fact, the data show that all six gauges positioned in the paths of these two drivers experienced the icing effect in Test 8. Conversely, Figure 27 shows the stagnation overpressure records from the gauges in the path of the diverging nozzle exit radii of the 19-m and 44-m drivers. This figure is consistent with Figure 25 in that it

shows no evidence of probe icing for those in the flow path of the drivers near the floor of the expansion section.

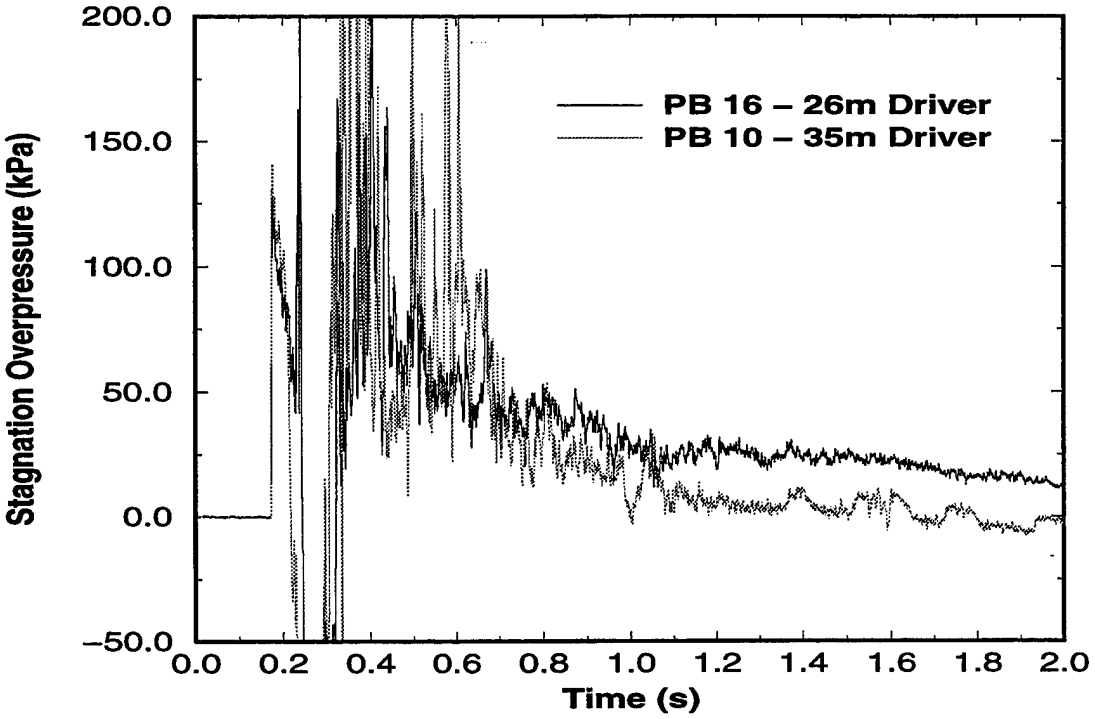

Figure 24. Test 8 Stagnation Overpressure from Gauges PB16 and PB10.

A possible explanation for this occurrence of the dropout effect on the high gauges is the available area for entrainment of ambient air into the expansion section. The structure that supports the drivers and nozzles consists of a network of steel beams and a concrete reaction mass, all of which tie into the ground. Even though the upstream end of the SSGG expansion section is open to the surrounding atmosphere, this structure restricts the available area in which air can be entrained around the 19-m and 44-m drivers near the floor. On the other hand, far less support structure exists near the top of the expansion section, which allows ambient air to be more readily entrained into the expansion section. The mixing of moist, entrained air with the cool, expanded driver gas is believed to cause the formation of small ice crystals in the flow.

Finally, the Test 8 stagnation overpressures from gauges positioned between the flow paths of the drivers are presented in Figure 28. Here, the flow histories from the different locations in the expansion tunnel are consistent with one another. The average stagnation overpressure impulse from these three gauges at a time of 2 s is 31.03 kPa-s.

7. NUMERICAL SIMULATIONS

Computational fluid dynamics (CFD) techniques are routinely employed to solve a wide variety of problems in the field of nuclear and conventional blast. Such modeling efforts

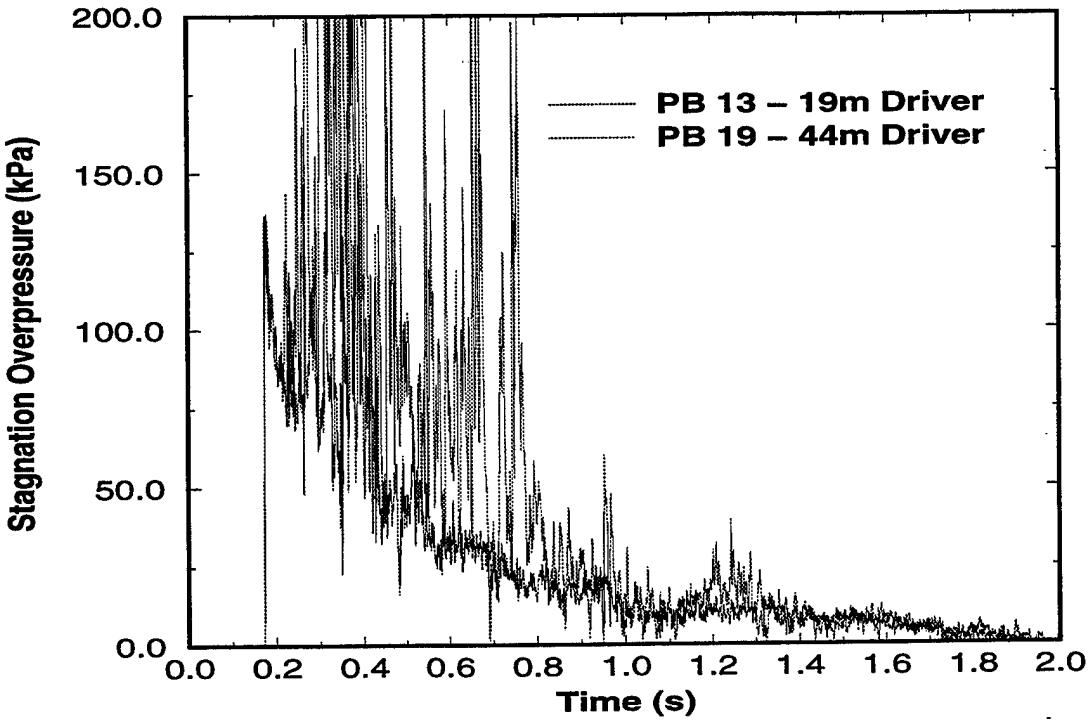

Figure 25. Test 8 Stagnation Overpressure from Gauges PB13 and PB19.

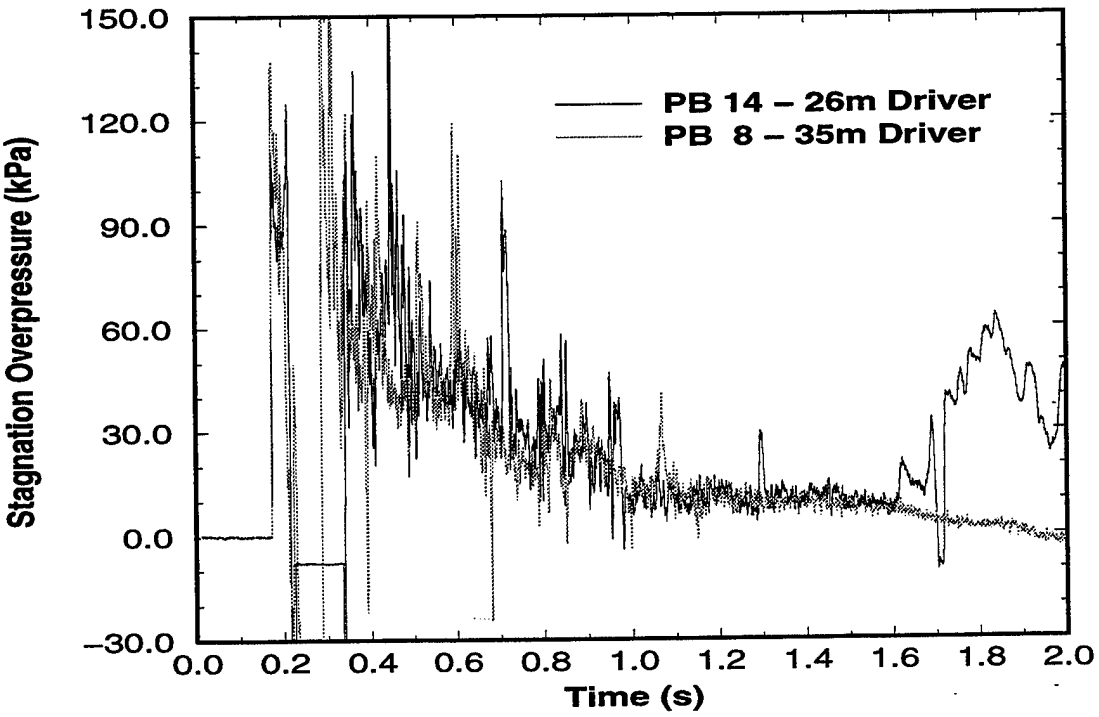

Figure 26. Test 8 Stagnation Overpressure from Gauges PB14 and PB8.

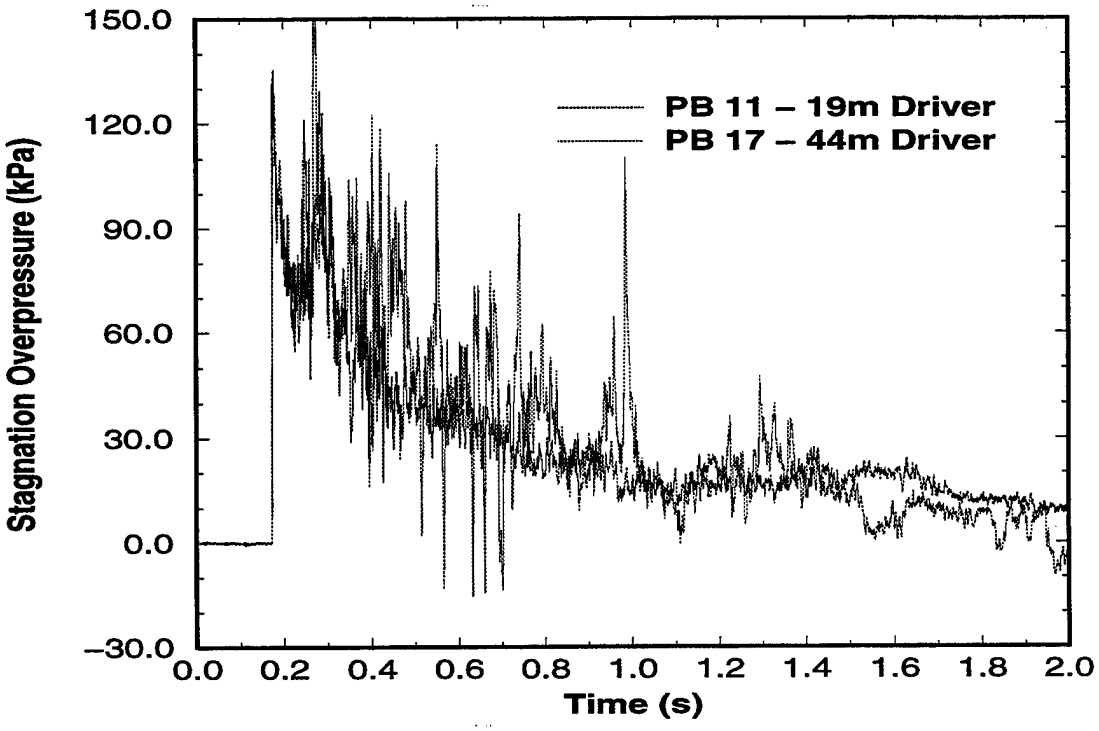

Figure 27. Test 8 Stagnation Overpressure from Gauges PB11 and PB17.

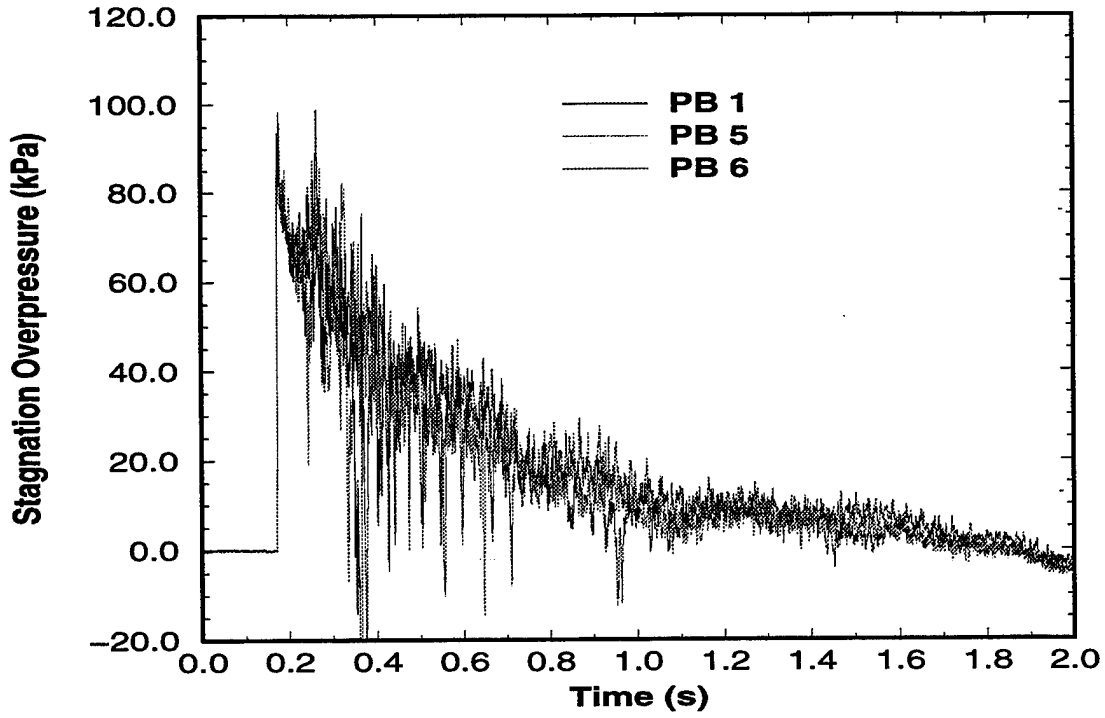

Figure 28. Test 8 Stagnation Overpressure from Gauges Between Drivers.

typically fall under one of two categories, the simulation of blast flow interaction with specific types of targets, and the numerical simulation of time-dependent flow in shock tubes and blast simulators. One common thread that links the vast majority of these studies is that most of them employed an approach that was a one-dimensional (1-D) or two-dimensional (2-D) approximation of a more complex system.

This simplifying approach has practical benefits in both experimental and computational studies. From an experimental standpoint, reduction of one of the spatial dimensions can significantly reduce the cost of fabrication of test articles and instrumentation requirements. The simplified geometry often leads to an improved understanding of the present blast phenomena. In some cases, experimental configurations are geometrically simplified for the purpose of making direct comparisons to 2-D computational predictions.

This geometric simplification offers several obvious advantages to the world of numerical simulation. A 2-D computational domain is a discrete collection of points that fall onto the curves that define the model. In 3-D, these curves project into complex surfaces whose shape may require many defining points to sufficiently describe it. In fact, much of the time spent in generating a 2-D model lies in the abstraction of a true three-dimensional (3-D) geometry into a 2-D computational domain. Like the advantage offered to the experimenter, model simplification may reduce the complexity of the phenomena being considered and therefore ease interpretation of the results. However, the most significant reason behind the use of geometrically simplified numerical models is the extraordinary cost associated with detailed 3-D computation.

These approximations, however, reduce the accuracy and reliability of numerical simulation. The work described in this report focuses on the recognition that 3-D numerical simulation will play an increasingly large role in assessing the survivability of military equipment in blast environments. Presently, large numbers of 1-D and 2-D simulations are used to conduct studies of time-dependent fluid flow in the free field, either over military equipment or within blast simulators. The results of these many calculations are employed to develop empirical relationships between the governing parameters of the problems. The relationships can then be used to quickly determine the behavior of one parameter with the variation of another. Currently, 3-D CFD simulations of blast phenomena are used as a final, confirming verification of the study, if used at all.

The reason for this lies in the cost of 3-D numerical simulations. A model with sufficient resolution to capture the driving flow phenomena in all three spatial dimensions can have millions of grid points. Time-dependent flow such as blast requires a converged solution to be computed for every time step. In other words, the fluid state at each of the millions of grid points must be computed for each time step. Typical tactical nuclear blast waveforms have a positive phase duration as long as 2 seconds. Tens of thousands of time steps may be required to march this solution through the time period of interest. Consequently, a 3-D numerical simulation of a time-dependent flow may require the calculation of 10^9 to 10^{11} grid point fluid states. Such computations take hundreds of hours to complete on today's most powerful supercomputers.

Despite these obstacles that inhibit the present utility of 3-D CFD simulations for blast modeling, it is advantageous to pursue the process of validating CFD algorithms for future use. Recent advances in scalable, parallel computer technology offer the possibility of 3-D numerical modeling of blast effects in a production environment. Research performed at ARL[13, 14] has demonstrated significant performance enhancements of CFD algorithms on massively parallel computers. By validating the predictive capability of candidate 3-D flow solvers for blast modeling, future efforts can be concentrated on modifying and optimizing these codes for execution on scalable, parallel computers.

8. DESCRIPTION OF FLOW SOLVERS

The two fluid dynamics codes selected for validation were the second order, hydrodynamic, advanced research code (SHARC) and the universal solution algorithms, real gas (USA-RG) code. Two-dimensional versions of both codes have been used to solve a wide variety of blast problems.[15, 16]

SHARC is an explicit Euler[17] solver,[18] which was derived from the Hull code, which was originally developed at the U.S. Air Force Weapons Laboratory to model nuclear blast loading on missile silos.[19] The underlying algorithm of SHARC is a finite difference scheme that employs a rectangular discretized mesh to model the computational domain. The algorithm is a discretization of the Euler equation, a subset of the Navier-Stokes[17] equation, which contains no viscous terms. The SHARC solution algorithm is second order accurate in space and time and also offers a k-ϵ turbulence model, which improves the capability of the code in cases that involve shear flow or flow over rough surfaces.

The Euler equation, illustrated in Equation 1, describes the motion of an inviscid, Newtonian fluid.

$$\rho \frac{D\mathbf{u}}{Dt} = -\nabla \cdot \mathbf{P} + \rho \mathbf{g} \tag{1}$$

When the k-ϵ turbulence model is employed, the conservation equations include terms for turbulent diffusion and Reynolds stresses. The turbulent dissipation is incorporated into the momentum equation in the form of a correction of the pressure term as shown in Equations 2 and 3,[20]

$$P_{ij} = \left(P_m + \frac{2}{3} \rho k \right) \delta_{ij} - S_{ij} \tag{2}$$

in which P_m is the thermodynamic pressure, δ_{ij} is the Kronecker δ function, and

$$S_{ij} = \mu_t \left[\frac{\partial u_i}{\partial x_j} + \frac{\partial u_j}{\partial x_i} - \frac{2}{3} \delta_{ij} \frac{\partial u_k}{\partial x_k} \right]. \tag{3}$$

In Equation 3, the term μ_t is the eddy viscosity computed by the k-ϵ turbulence model. According to the relation in Equation 4,

$$\mu_t = \rho C_\mu \frac{k^2}{\epsilon} \tag{4}$$

in which k is the local turbulence kinetic energy per unit mass, ϵ is the time rate of dissipation of k, and C_μ is a constant.[21]

When used to model turbulent flow near a wall, this implementation of the k-ϵ model imposes a theoretically established boundary layer profile, also referred to as a "wall function."[22] This approach allows the computation to mimic the flow pattern resulting from the viscous stresses and eliminates costly grid clustering near walls to resolve the boundary layer. The SHARC calculations described in this report did not employ wall functions.

SHARC supports 2-D axisymmetric, 2-D cartesian, and 3-D cartesian geometries. Variable spacing of grid points along each coordinate axis is allowed. Complex shapes are modeled by placing a perfectly rigid, perfectly reflective material, known as "island" material, in the rectangular (2-D) or box-shaped (3-D) computational cells. The degree to which computational results match experimental results is affected by the grid resolution used. In general, higher grid resolutions lead to better agreement. Increasing grid resolution, however, can quickly lead to unreasonably long run times.

Like all explicit, time-marching codes, the time step in SHARC is a function of the cell size, particle velocity and sound speed. For every iteration through time, a characteristic time scale for each cell in the grid is determined by the ratio of the cell size, divided by the sum of the particle velocity and fluid sound speed in that cell. The smallest characteristic time of all the cells determines the time step of the entire computational domain. As a result, increasing the grid resolution will cause a drop in the time step, as well an increase in the number of cell in the domain. For example, doubling the grid resolution of the 3-D SHARC computation will increase the run time by a factor of 16, because of the factor of two drop in the time step and the doubling of the number of grid points in each coordinate direction. Thus, the grid resolution selected for a computational study involves a trade-off between the accuracy of the result and the time required to obtain a solution.

The USA-RG code discretizes the Navier-Stokes equation using a finite volume, Roe's Riemann solver, total variation diminishing (TVD), implicit algorithm.[23] The implicit scheme produces an algorithm that is well suited for blast wave calculations because upwind flux difference splitting with TVD achieves second order accuracy without introducing spurious oscillations near discontinuities. Strong gradients and complex flow fields are resolved accurately. TVD schemes are often referred to as modern shock-capturing methods because the numerical dissipation terms are nonlinear. That is, the amount of dissipation is controlled by automatic feedback mechanisms that can vary from one grid point to another. Also, the dissipation is scaled to the underlying eigensystem of the hyperbolic Euler equation. In classical shock-capturing methods, the numerical dissipation terms are either linear so that the same amount of numerical dissipation is added at all grid points or the numerical dissipation is controlled by parameters that must be optimized. Classical shock-capturing methods typically result in oscillatory solutions at strong discontinuities.

The conservative nature of the scheme captures shocks and other discontinuities automatically. The finite volume philosophy ensures energy and mass conservation at interior grid points. The implicit version of the scheme requires more computations per integration step than the explicit version but permits larger time steps which, for mathematically stiff

(viscous) problems, reduces computational expense. The code has the capability to handle multi-zone grids and has several turbulence models available. These models are modified Baldwin-Lomax[24] (0 equation), k-L[25] (1 equation), and k-ϵ[26] (2 equation).

The Navier-Stokes equation, Equation 5, describes the motion of a viscous, Newtonian fluid.

$$\rho \frac{Du_i}{Dt} = -\frac{\partial p}{\partial x_i} + \rho g_i + \mu \left[\nabla^2 u_i + \frac{1}{3} \frac{\partial}{\partial x_i} (\nabla \cdot \mathbf{u}) \right] \tag{5}$$

When a turbulence model is incorporated into the solution method, the turbulent distributions are used to form an eddy viscosity field, μ_t, that is added to the molecular viscosity, μ_v, to yield a net viscosity, μ.[25] This viscous term is then used in the Navier-Stokes equation (5) to account for the turbulent and molecular dissipation.

The USA-RG code and other computational fluid dynamics codes like it employ gridding techniques that are quite different from those of SHARC. In particular, the coordinate axes are not required to be straight lines. Rather, the coordinate axes can be defined in practically any form necessary to define the complex shape of the system being modeled. This type of grid is referred to as "body conformal" because the grid can be wrapped around the body of interest, thus modeling it with a high level of accuracy. An additional level of flexibility is available to the USA-RG code in that it supports multi-zone grids. This basically means that numerous independent body conformal grids can be combined in one computational model to represent the system with a high degree of fidelity without placing a large number of grid points in regions of uniform steady flows.

9. 3-D SHARC MODELS

The SHARC code representation of the SSGG facility was developed to model as closely as possible the driver systems and expansion section of the blast simulator. The model takes advantage of the symmetry of the facility about the vertical center plane. The expansion section of the SSGG is 105 m long, with an RWE positioned at the downstream end. The purpose of the RWE is to suppress the generation of a rarefaction wave that forms when the shock front exits the downstream end of the expansion section.[1] Such disturbances in the flow field can destroy the fidelity of the simulated blast environment. An RWE modifies the exit flow from the expansion tunnel in such a way that it makes the tunnel appear infinitely long. To avoid the computational complexity of modeling the dynamics of the flow through the RWE, the expansion section in the 3-D SHARC model was made sufficiently long that no disturbance to the flow field would be observed at the measurement locations during the time of interest.

Two different 3-D SHARC models of the SSGG were developed, the first of which is illustrated in Figure 29. This figure shows the half of the facility that was represented by the model. The vertical center plane was represented as a reflective plane to account for the geometric symmetry of the problem. This figure shows the four unique lengths of driver, each connected to a cylindrical throat section that empties into the diverging nozzles. This figure also demonstrates the means by which the model is shaped by placement of "island"

cells in the grid. The actual diverging nozzles are conically shaped, but the figure shows the diameter change in a series of steps. Each step corresponds to a transition of the island material from one grid plane to the next. This characteristic is also evident in the shape of the cylindrical driver tubes.

The upstream end of the expansion section of the SSGG is open to the surrounding atmosphere. The propagation of the shock down the expansion tunnel causes the ambient air to be entrained into the expansion section and can influence the flow histories there. The initial model SHARC was not developed with the capability to simulate this effect. In Figure 29, one can see the solid wall at the upstream end of the expansion section, which connects the diverging nozzles to the walls of the tunnel. Because the entrainment of ambient air is considered to be an important characteristic of the time-dependent flow, a second 3-D SHARC model was developed to provide ambient air surrounding the facility. Figure 30 shows this later model. In this figure, the driver tubes have been eliminated to make the spacing between the diverging nozzles more noticeable.

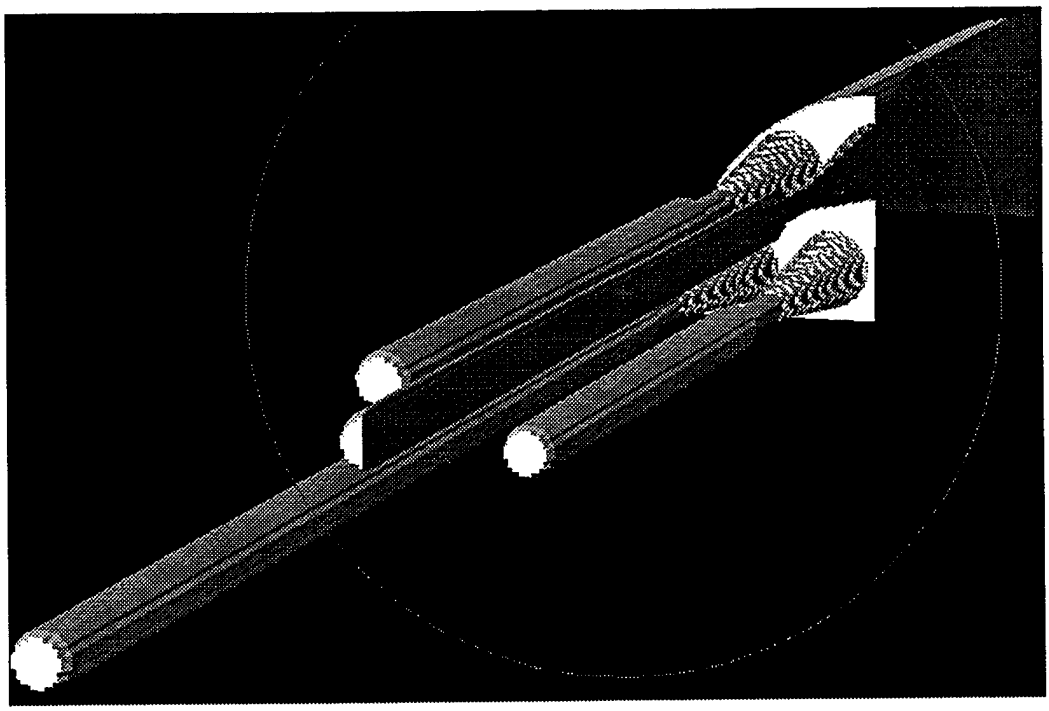

Figure 29. Initial SHARC Model of SSGG.

The figure also shows the model reflected about the plane of symmetry to provide a more realistic view of the facility. Figure 30 illustrates that the structural elements that support the driver tubes are not present in the model. As a result, this model has a greater available area for flow to be entrained into the expansion section than does the actual blast simulator.

Figure 30. SHARC Model of SSGG for Ambient Air Entrainment.

9.1. Preliminary SHARC Calculations

The models presented were developed and tested before the execution of the SSGG experiments described earlier. These test computations were simulations of experiments which had been performed in the SSGG in 1987 to determine the effects of expansion tunnel blockage on blast flow histories. Figure 31 is from a SHARC calculation that simulates one of the tests in that series in which a shock overpressure of nominally 75 kPa was produced in the expansion section. The presence of the solid wall at the upstream end of the expansion section shows that this calculation was performed using the model that did not provide ambient air entrainment into the tunnel. The figure shows the formation of the primary shock at 16 ms, 20 ms, and 28 ms. Here, a time of zero corresponds to the initiation of flow at the diaphragm position. In Figure 31a, four individual shock fronts produced in the different drivers are evident. At this point in time, the primary shocks have not yet entered the expansion section. At 20 ms, Figure 31b shows the individual shocks expanding into the expansion section and beginning to coalesce to the wall, floor, and interfaces between shocks. Finally, Figure 31c presents a nearly planar shock front at 28 ms after flow initiation. This series of figures presents that, according to the computation, the shock front is uniform near the upstream end of the expansion section.

To assess the influence of ambient air entrainment into the SSGG expansion tunnel, a calculation was performed using the second 3-D SHARC model. This calculation used the same initial conditions as the first test calculation. The results of the two calculations are presented in Figure 32 and show stagnation overpressure histories recorded in the expansion section at a distance of 52.5 m from the upstream end of the expansion section. This figure shows two significant influences of the inflow on the recorded histories in the tunnel. First, the calculation without the entrainment capability produced a significant increase in the stagnation overpressure between 115 ms and 180 ms after shock arrival at the measurement position. This increase is caused by the arrival of the driver gas at the measurement position. The driver tubes in the SSGG are pressurized with air by compressors. At the time of flow initiation, the temperature of the compressed driver air is about the same as the surrounding atmosphere. When the flow is initiated, the driver gas expands into the tunnel, which causes the driver gas to cool. This results in an increase in the density of the driver gas and is the cause of the increase in the stagnation overpressure history of Figure 32. In the same figure, the curve generated by the inflow model has a much smaller increase at this same point in time, so small that it would be difficult to differentiate it from the other oscillations if not for the result of the calculation with no inflow. The increase in stagnation overpressure resulting from the arrival of the driver gas is smaller for the inflow case because the entrained, ambient air is at a higher temperature than the expanded driver gas and mixes with the driver gas before arriving at the measurement position. The mixing of the driver gas with the entraied air increases the temperature of the expanded driver gas, thereby decreasing its density.

The other effect of ambient air entrainment that is noticeable in Figure 32 is the elevated level of the record from the inflow model in late time. This elevated pressure level results from the increased mass flow through the expansion tunnel created by the addition of the entrained ambient air. The elevated pressure level increases the impulse delivery to a test

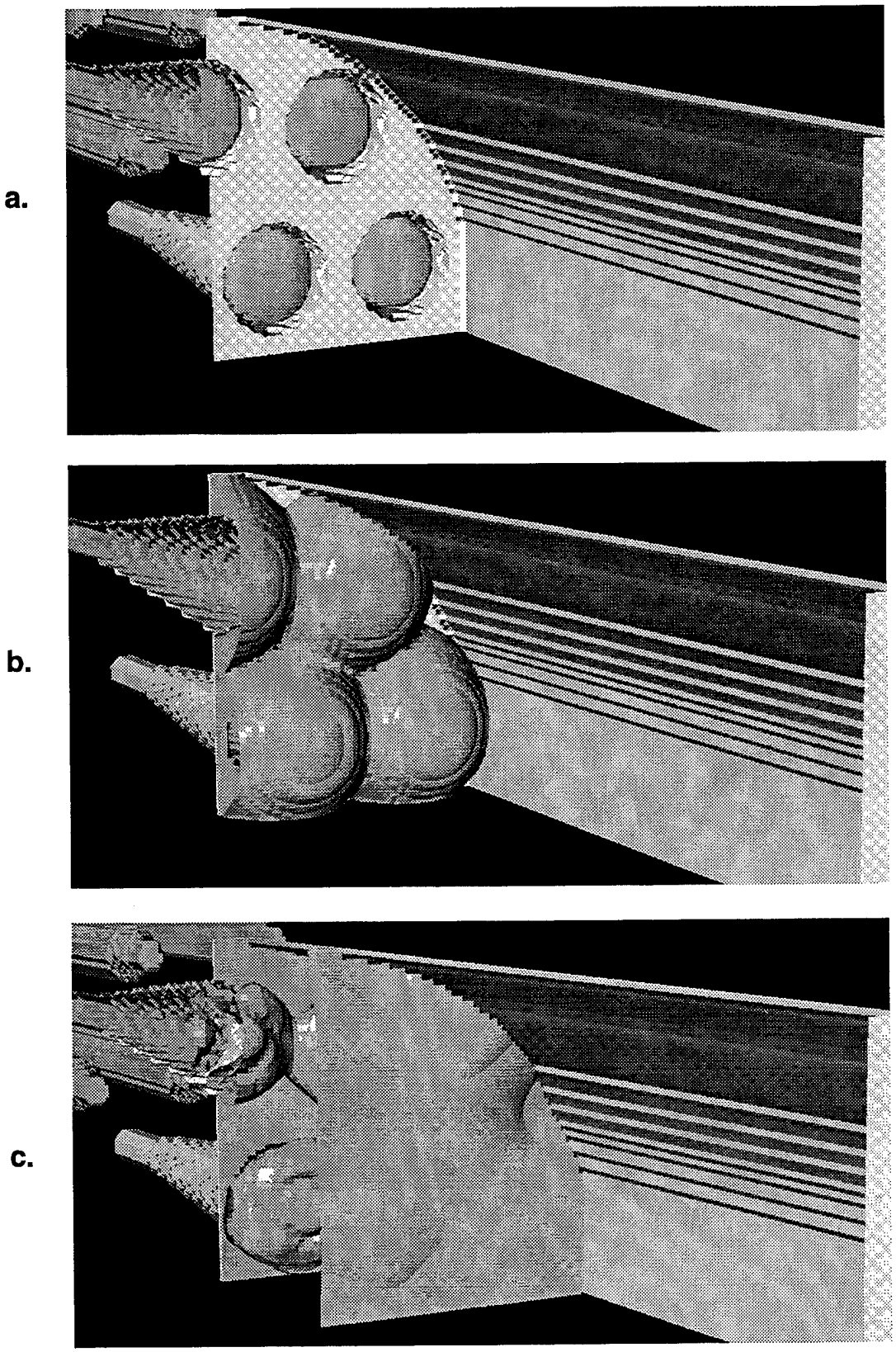

Figure 31. SHARC Simulation of Shock Formation at a) 16 ms, b) 20 ms, and c) 28 ms.

article, and thus the simulated weapon yield is increased. By comparison, the stagnation overpressure impulse of the model without the inflow is 37.83 kPa-s, while that of the inflow model is 42.57 kPa-s at 870 ms after shock arrival. At this point, the positive phase is not yet complete. It is logical to assume that by the end of the positive phase, the difference in stagnation overpressure impulse between these two records would be even greater.

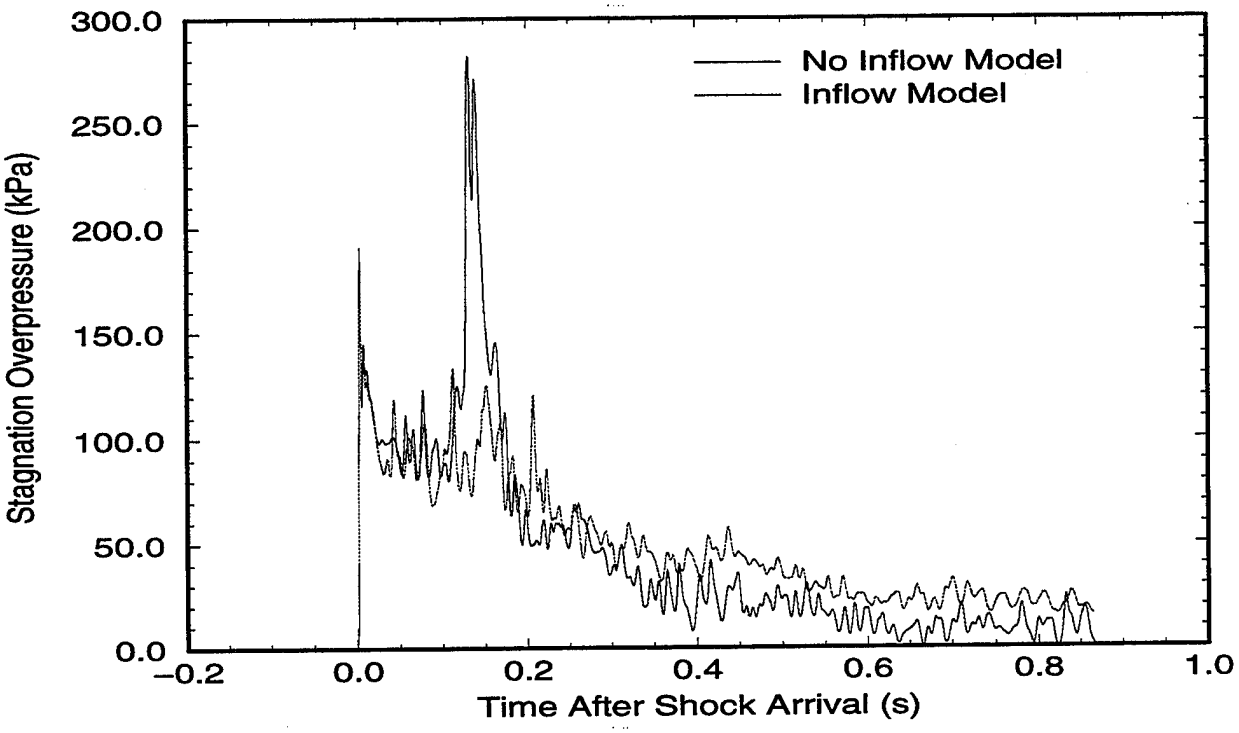

Figure 32. Comparison of SHARC Models with and Without Ambient Air Entrainment.

10. SHARC FLOW UNIFORMITY CALCULATIONS

After the preliminary test calculations were complete and the SSGG flow-mapping tests were done, a series of 3-D SHARC calculations was performed to match the 20-kPa and 80-kPa tests from the experimental study. Based on the influence of the ambient air entrainment observed in the preliminary calculations, it was decided that the inflow model would be used for the remainder of the numerical study. This model employed a grid with 85 cells in the horizontal direction, distributed along lines normal to the plane of symmetry, 91 cells in the vertical direction normal to the ground plane, and 478 cells in the longitudinal direction. The size of the cells varied throughout the grid, with the highest concentration of grid points in the area of the converging/diverging nozzles and the upstream end of the expansion section. In this region, a nominal cell size of 7 cm was used. This level of grid resolution placed ten computational cells across the diameter of each throat section, which is considered the minimum amount of cells required to capture the dominant flow characteristics. Additional grid resolution would have led to better definition of the flow structure but would have made the calculations impossible to complete, even on the most powerful vector supercomputers.

A total of four SHARC calculations was performed with this model: two without the turbulence model and two using the k-ϵ model. A summary of these calculations is provided in Table 3. At regular intervals during the execution of a calculation, the solution is saved in the form of a restart file. The restart file primarily contains the hydrodynamic variables at each grid point. For the cases in which the turbulence model was not used, a single restart file contained five hydrodynamic variables at each of the nearly 3.7 million cells in the grid. The resulting binary restart file for a non-turbulent SHARC calculation was 148 MB in size. The turbulent SHARC calculation stores seven variables at each computational cell and the resulting restart file for the inflow model is 207 MB.

Table 3. Summary of 3-D SHARC Calculations.

Calculation	Nominal Shock Overpressure (kPa)	Solution Method	Computed Cycles	Flow Time (ms)	CPU Time (hours)
1	20	Euler	6058	800	45 (C-90)
2	20	Euler + k-ϵ	4485	450	93 (C-90)
3	80	Euler	7516	1000	100 (X-MP)
4	80	Euler + k-ϵ	13741	645	288 (C-90)

Table 3 clearly demonstrates the cost of this type of numerical simulation. For each of the cases, many thousands of computational cycles are required to step the solution through the time of interest. The additional cost of using the k-ϵ turbulence model can be determined by comparing a nonturbulent calculation to its otherwise identical turbulent case. For each of the two overpressure levels, the turbulent calculation required more than double the computer time to march the solution through a shorter period of time. This is caused by the combined effect of an increased number of floating point computations to solve the two additional partial differential equations of the turbulence model and the decrease in the time step which is caused by the numerical formulation of the turbulence model.

10.1. SHARC Calculations of 20-kPa Tests

The first two SHARC calculations to match the flow-mapping tests simulated the conditions of the 20-kPa overpressure shots of the test series, Tests 1 and 6. To assess the accuracy of the calculations in simulating the flow in the expansion tunnel, the time history data generated by the calculations are compared to the data gathered from the experiments. To best assess the code's ability to model the basic flow parameters of pressure, density and velocity, the stagnation overpressure records from the experiments are used as the benchmark. In each of the comparisons, the turbulent and nonturbulent SHARC calculation results are plotted together with the appropriate experimental record to illustrate the differences of the solution methods and the accuracy of the simulations as compared to the experiments.

Figure 33 shows the Test 1 recording from gauge PB19 compared to the SHARC results. This gauge location is at the 67.5-m longitudinal position, in the path of the centerline

of the longest driver. This figure shows several interesting characteristics of the SHARC predictions. The overall shape of the calculated histories closely follows the experimental data. The nonturbulent solution captures many of the features observed in the experimental data but has a greater stagnation overpressure than the experiment 250 ms after shock arrival. The turbulent solution has a lower stagnation overpressure than the nonturbulent solution and lacks much of the secondary flow structure that is evident in the experiment and the nonturbulent case.

Figure 34 compares the stagnation overpressure from Test 1, gauge PB4, to the equivalent SHARC results. This gauge was positioned between the paths of two drivers. The figure shows a very similar result to the previous comparison. This is to be expected because the flow at the test section was found to be highly uniform at the 20-kPa and 80-kPa overpressure levels. In fact, the flow histories predicted by the turbulent and nonturbulent SHARC solutions are extremely uniform at this 67.5-m position. When many are plotted together from different points in the cross section, the curves almost exactly follow one another.

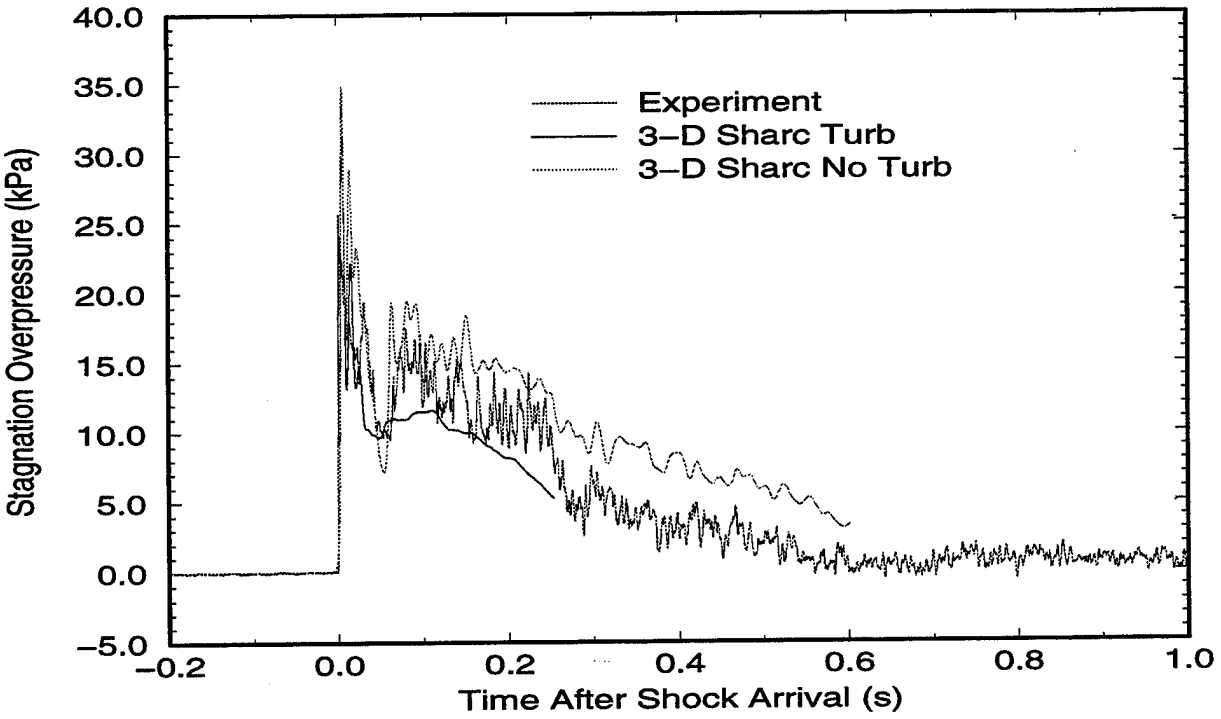

Figure 33. SHARC Simulations of Test 1, Gauge PB19.

The SHARC results are compared to the Test 6 experimental data in Figures 35 and 36. Again, the stagnation overpressure histories from gauges PB19 and PB4 were used. In Test 6, the instrumentation array was placed at the 22.5-m position. The PB19 experimental result from this test showed signs of the production of jet flow from the 44-m driver. This is evident by the increase in stagnation overpressure beginning at about 400 ms after shock arrival and continuing for the remainder of the record. The SHARC nonturbulent prediction closely follows the experimental result until reaching the point where the experimental data

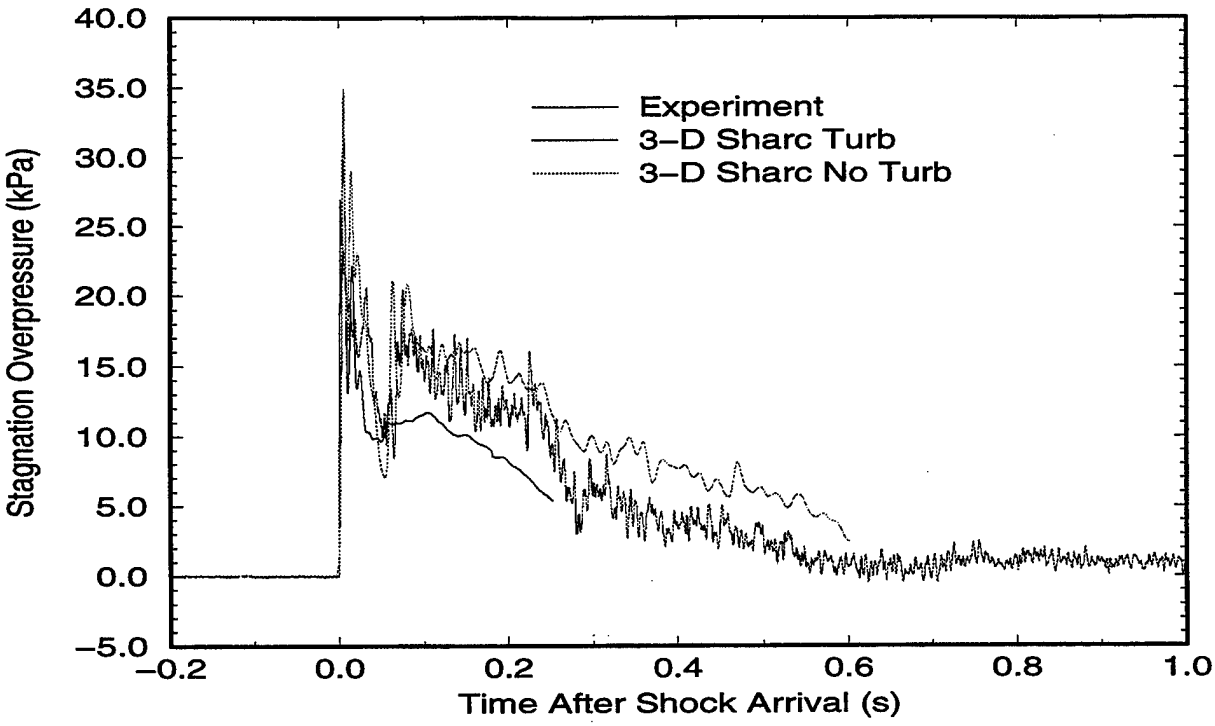

Figure 34. SHARC Simulations of Test 1, Gauge PB4.

increase. The stagnation overpressure of the SHARC turbulent result again was slightly lower than that of the experimental result.

The comparisons in Figure 36 show the same characteristics in comparison to gauge PB4 from Test 6. The nonturbulent prediction of stagnation overpressure very closely follows the experimental data, while the turbulent solution predicts a lower stagnation overpressure. The advantage of the turbulent solution is evident at about 50 ms after shock arrival when the experimental record decreases to approximately 10 kPa, then quickly recovers to about 17 kPa. The turbulent solution accurately predicts the minimum value and timing of the drop but does not increase to as high a value as the experiment. The nonturbulent solution overpredicts the drop in stagnation overpressure, reaching a value of about 5 kPa and quickly overcompensating by increasing to a value of 25 kPa, after which, it resumes following the experimental data.

The results of Figures 33 through 36 indicate that the k-ϵ turbulence model is providing too much dissipation of the flow, thereby eliminating some of the significant flow features and secondary flow structure. This is believed to be the result of the low grid resolution used in the model. Two-dimensional computational studies with SHARC have demonstrated improved performance of the turbulence model with increasing grid resolution. Unfortunately, increasing the grid resolution of this model is not a viable option for the current class of vector supercomputers.

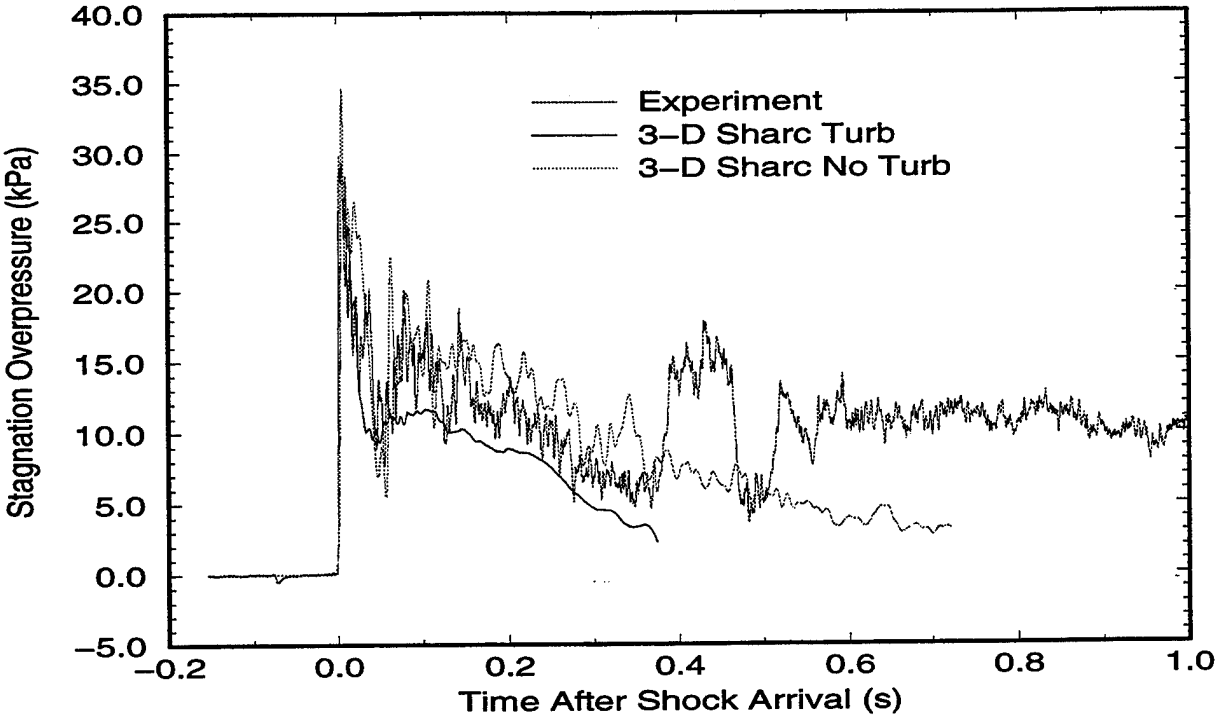

Figure 35. SHARC Simulations of Test 6, Gauge PB19.

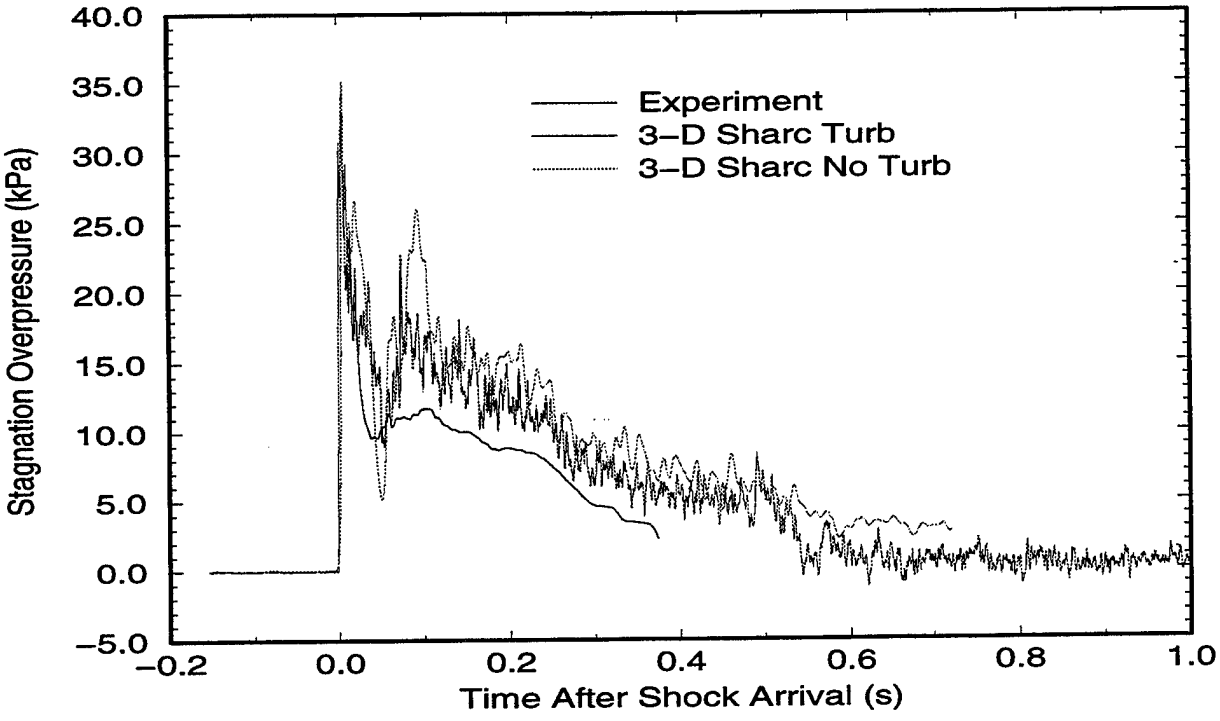

Figure 36. SHARC Simulations of Test 6, Gauge PB4.

10.2. SHARC Calculations of 80-kPa Tests

The low grid resolution causes the nonturbulent simulation of the 20-kPa tests to appear to be a better prediction than the turbulent solution. However, it should be noted that these comparisons apply to a flow with relatively weak shocks and small gradients. The more challenging test of both solution methods lies in the simulation of the 80-kPa tests. The results of these calculations are presented in Figures 37 through 40, in which the turbulent and nonturbulent predictions are again compared to the PB19 and PB4 stagnation overpressure records. The first two of these figures plot the records from Test 2 which were recorded at the 67.5-m position. In Figure 37, the two SHARC solutions follow similar patterns that are initially greater than the stagnation overpressure of the experiment, then follow more closely after 250 ms. Like the 20-kPa calculations, the turbulent solution lacks some of the secondary flow structure of the nonturbulent solution and the experiment, an indication that the use of the k-ϵ model with the low grid resolution provides excess dissipation of the flow. The comparison of the SHARC solutions to the recording of gauge PB4 is presented in Figure 38 and again shows the two SHARC solutions following similar paths. Both computational results are slightly lower than the experimental stagnation overpressure for most of the history. However, the agreement between the calculations and the experiment is very good.

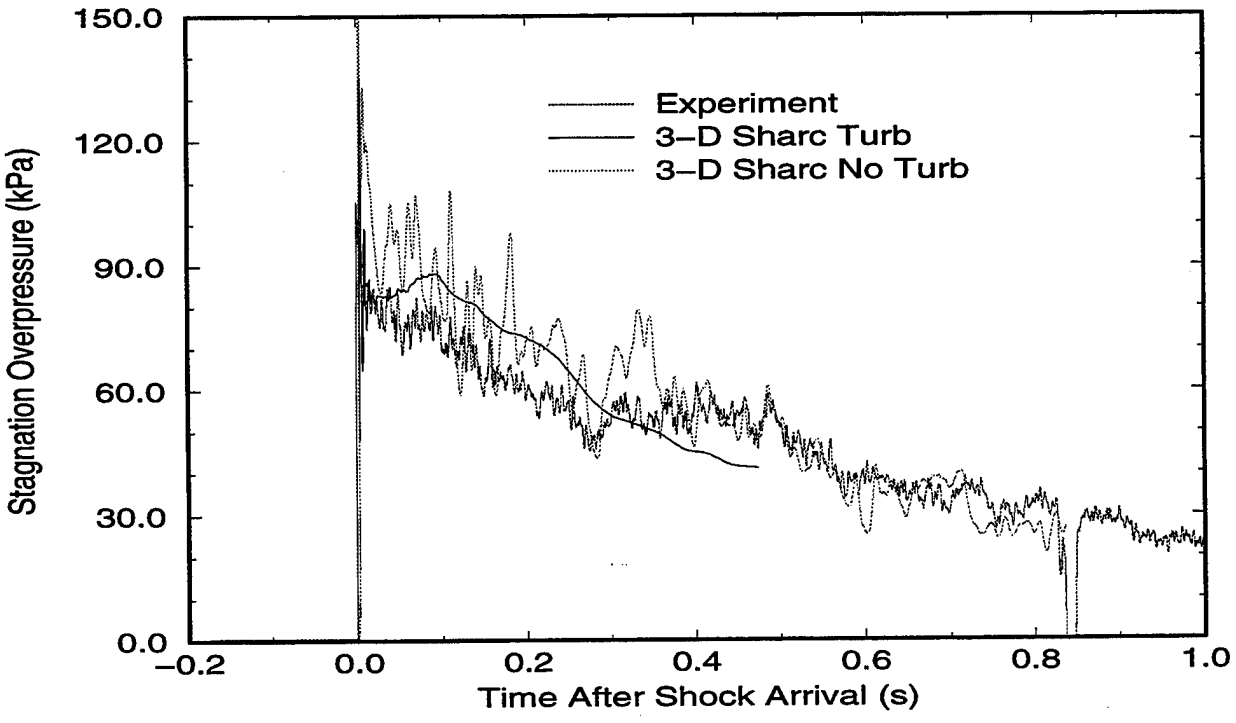

Figure 37. SHARC Simulations of Test 2, Gauge PB19.

The most interesting comparisons between the 3-D SHARC calculations and the experiments is at the 22.5-m location for the other 80-kPa shot, Test 8. The stagnation overpressure of the two calculations is compared to the PB19 record in Figure 39. In this figure, the experimental data show signs of highly turbulent jet flow from the 44-m driver at the

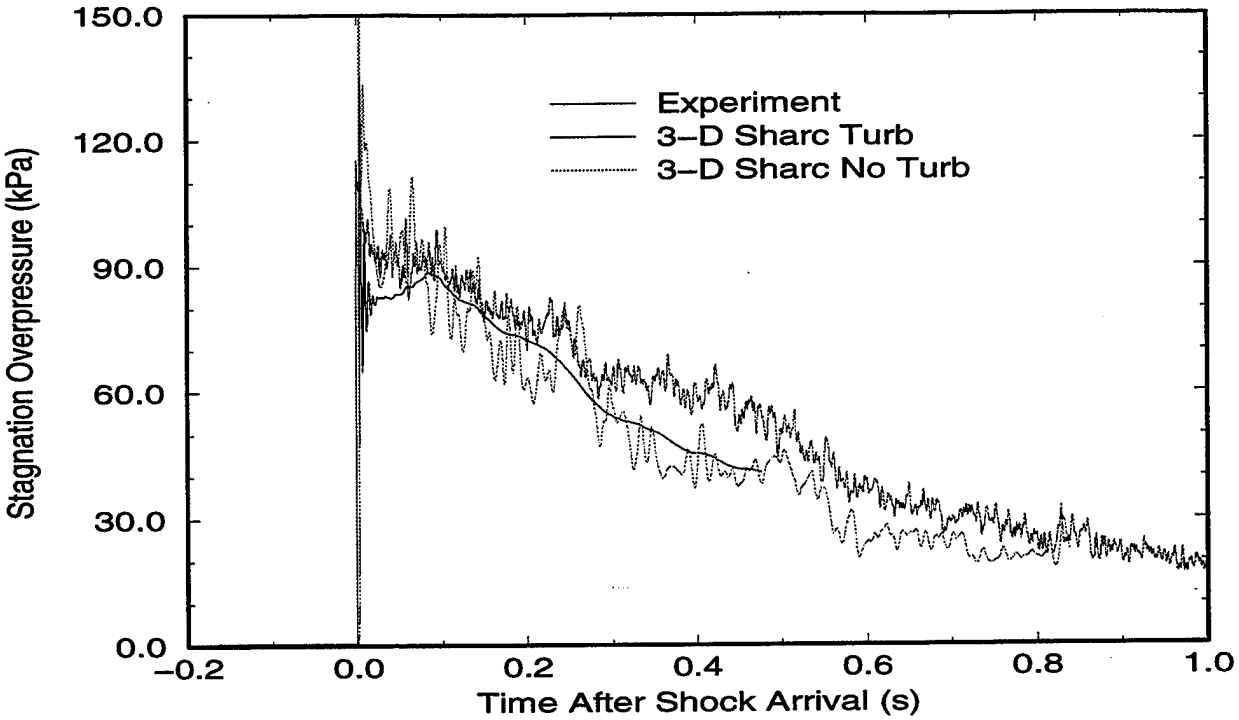

Figure 38. SHARC Simulations of Test 2, Gauge PB4.

22.5-m position. The nonturbulent calculation overpredicts the coherence of the driver jet and predicts stagnation overpressures that are well outside the limits plotted in Figure 39. In fact, the nonturbulent solution has sustained stagnation overpressure levels of more than 3000 kPa at certain times in the record. In contrast, the calculation with the k-ϵ turbulence model generally follows the path of the experimental data, while still lacking the secondary flow structure.

Finally, the PB4 stagnation overpressure recorded on Test 8 is compared to the SHARC calculation in Figure 40. This figure shows that the nonturbulent calculation significantly underpredicts the stagnation overpressure at this gauge location between two drivers, an artifact of the artificially strong driver jet flow produced by the nonturbulent solution. Consistent with the other figures, the turbulent solution accurately predicts the path of the experimental history but lacks some of the flow structure.

The excess dissipation of the turbulent solution results in a computed flow field that is uniform at the 22.5-m measurement position. However, the experimental data from Test 8 indicate the presence of some jet flow from the drivers, which diffuses before reaching the 67.5-m test section.

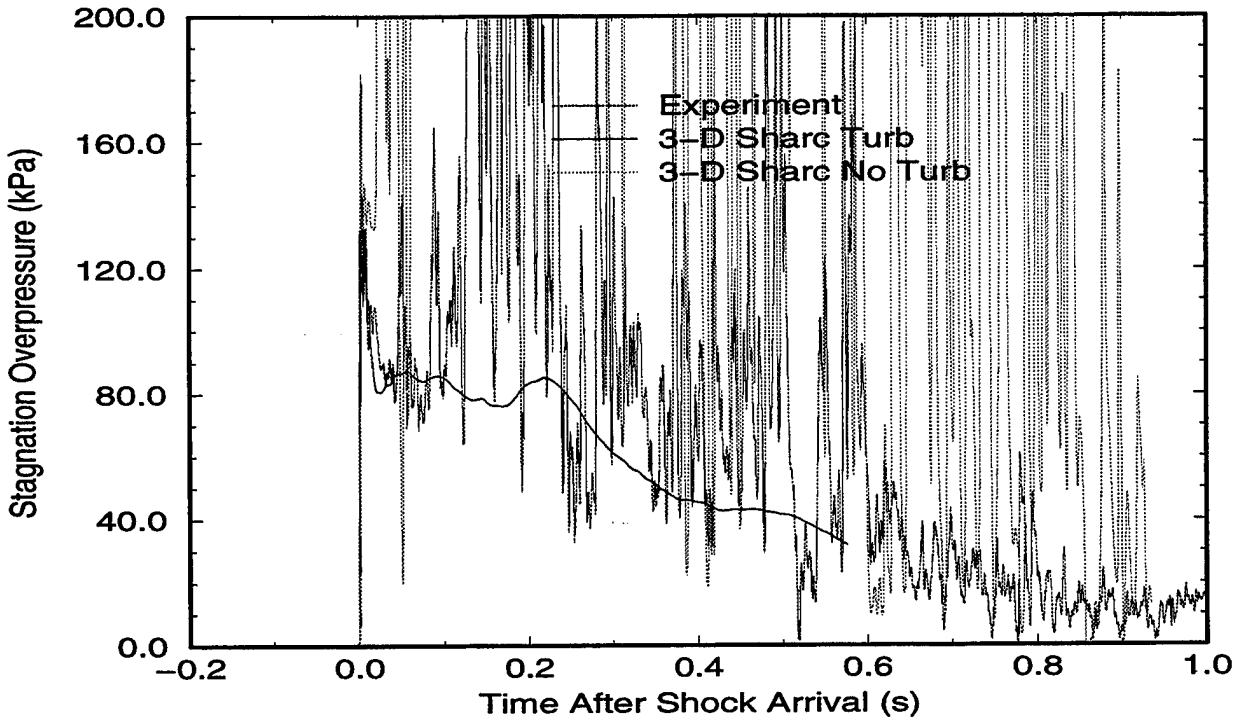

Figure 39. SHARC Simulations of Test 8, Gauge PB19.

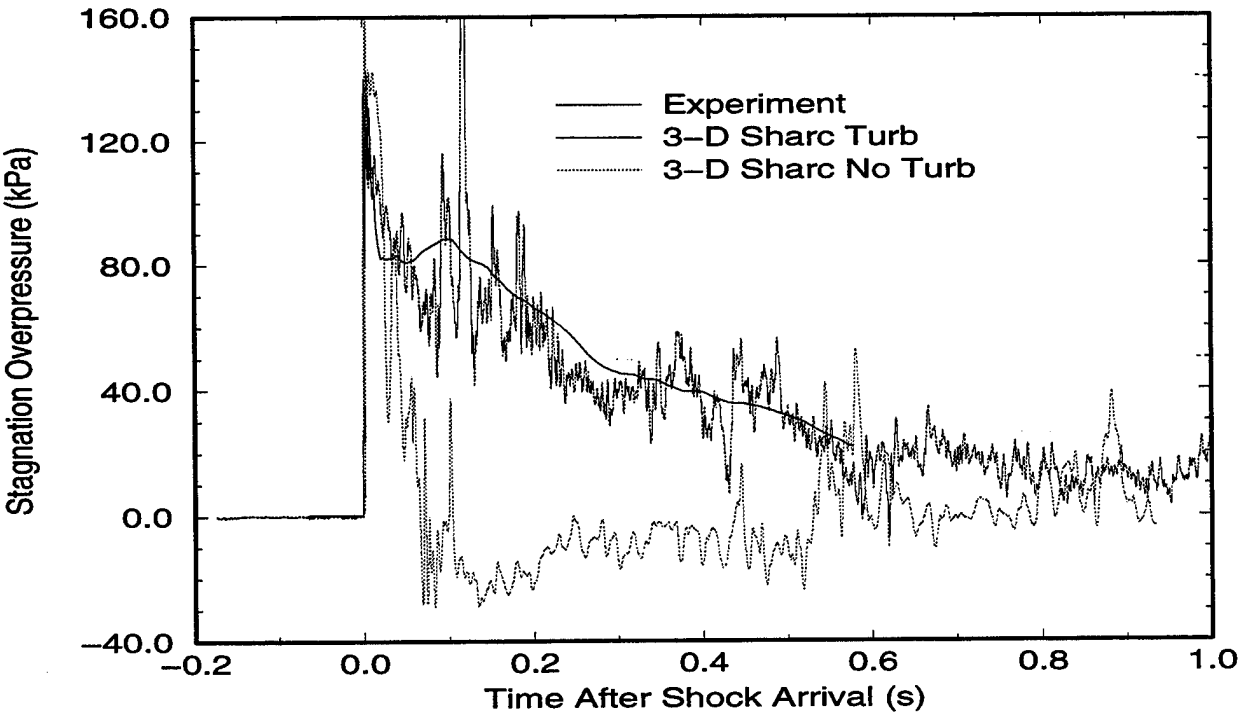

Figure 40. SHARC Simulations of Test 8, Gauge PB4.

11. USA-RG3 MODEL

The USA-RG3 code model consists of a collection of body conformal grids, or zones, which are combined to define the shape of the drivers and expansion tunnel of the SSGG. Like the 3-D SHARC models, the USA-RG3 model takes advantage of the symmetry of the facility that exists at the vertical center plane of the SSGG. The expansion section is again made artificially long so that disturbances generated at the exit boundary of the model may not arrive at the measurement locations within the period of interest. The USA-RG3 model was designed to allow entrainment of the surrounding ambient air into the expansion section. Figure 41 provides a view of the upstream end of the expansion section of the USA-RG3 model. In this figure, the driver tubes and converging nozzles have been dropped to illustrate the grid definition in the throat sections at the diaphragms. The figure also shows how the shape of the grid defines the surfaces of the diverging nozzles and expansion section. The zones that provide the surrounding ambient air for entrainment are not shown, but the grid definition at the upstream end of the tunnel for the area between the drivers is evident in the figure.

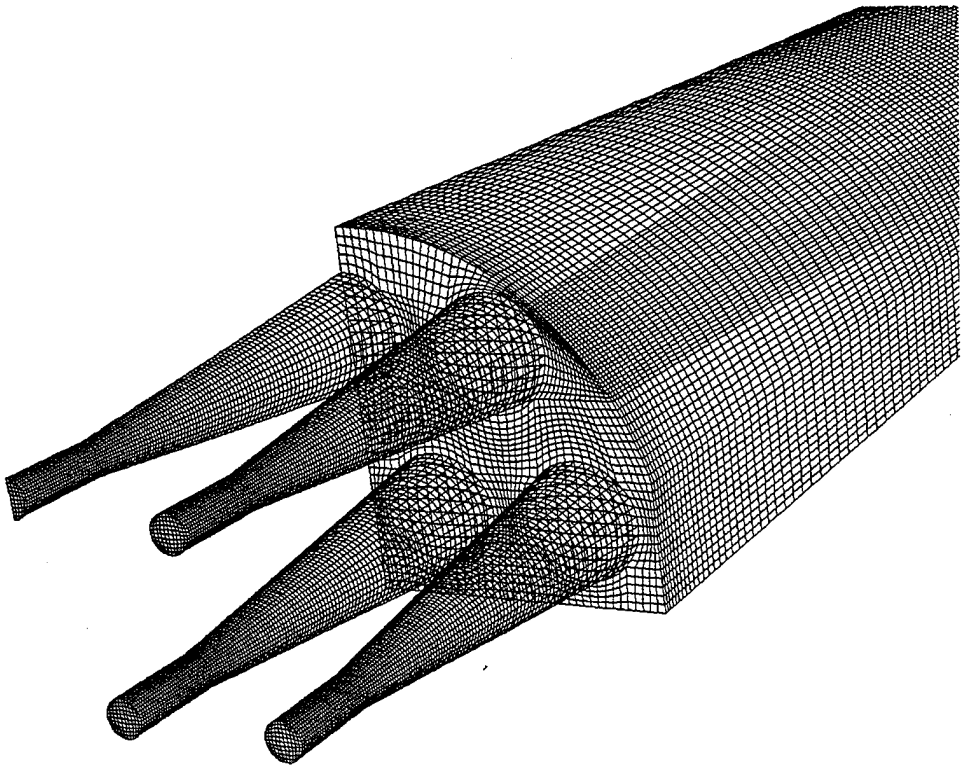

Figure 41. USA-RG3 Model of SSGG.

The multi-grid model contains 21 independent zones, each with its own generalized, curvilinear coordinate system. The interfacing grid points at the zone boundaries are aligned and the flow solver allows flow across these interfaces through communicating boundary condition routines. Approximately 780,000 grid points are used in the USA-RG3 model of the SSGG. The grid was developed with the greatest concentration of points near the

upstream end of the expansion section and in the converging/diverging nozzle area. Similar to the SHARC model resolution, ten computational cells were placed across the diameter of each throat section. This resolution results in 100 cells within the cross section of each driver at every longitudinal grid point. The implicit solution of the Navier-Stokes equation with k-ϵ turbulence modeling involves the solution of 5.5 million simultaneous equations at each time step and requires about 400 MB of core memory.

12. USA-RG3 FLOW UNIFORMITY CALCULATIONS

A series of USA-RG3 calculations was performed to match the 20-kPa and 80-kPa shots from the SSGG flow-mapping tests. These calculations were executed in a similar manner to the set of SHARC calculations described previously. Two calculations were run at each of the shock overpressure levels, one an inviscid flow solution and the other a viscous solution using the k-ϵ turbulence model.

Table 4 provides a summary of some of the details of these calculations. The third column in the table, entitled *Solution Method* describes the set of equations that was used to solve the equations of motion of the fluids. In this column, an Euler solution method refers to the solution of the fluid motion equations without the viscous terms used. Conversely, N-S + k-ϵ in the table describes a Navier-Stokes solution (viscous terms used) with the 2-equation k-ϵ turbulence model employed. All of the USA-RG3 calculations were run on a Cray C-90 vector supercomputer.

Table 4. Summary of USA-RG3 Calculations.

Calculation	Nominal Shock Overpressure (kPa)	Solution Method	Computed Cycles	Flow Time (ms)	CPU Time (hours)
1	20	Euler	8400	919	62
2	20	N-S + k-ϵ	8400	919	115
3	80	Euler	9200	1459	68
4	80	N-S + k-ϵ	9200	1459	126

In Table 4, one can see that the number of cycles and the simulated flow time are common between an inviscid solution and its corresponding Navier-Stokes solution. This is different from the SHARC code results in which the turbulent solution required not only more CPU time per cycle but also a greater number of cycles to reach the same simulated flow time. As described earlier in the case of the SHARC code, the turbulence model is explicit and the turbulence quantities have an effect on the time step, generally acting to decrease it. In the case of the USA-RG3 code, the solution method is completely implicit. As a result, the time step is not affected by the turbulence model.

12.1. USA-RG3 Calculations of 20-kPa Tests

The flow uniformity analysis and the earlier discussion of air entrainment both described the significance of the density of the expanded driver gas on the ideal nuclear blast simulation. The results of the USA-RG3 simulation of Tests 1 and 6 help to describe the evolution of the driver gas as it moves down stream in the expansion tunnel and mixes with the entrained air and the tunnel gas. Figures 42 and 43 present illustrations of the density distribution in the shock tube at 172 ms and 302 ms, respectively. In these figures, obtained from the viscous, turbulent solution, density levels are depicted by the shading of various surfaces in the computational domain. The vertical planes in the expansion section area at 22.5 m and 67.5 m indicate the density distribution at the two instrumentation array locations. Grid surfaces that pass through the driver horizontal center planes are also provided to show the longitudinal and lateral motion of the driver gas. Figure 42 shows that at 172 ms after flow initiation, the shock front is approaching the 67.5-m position (shown in the upper right corner of the figure) but has not yet reached it. The leading edge of the driver gas from the individual drivers has begun to pass through the 22.5-m plane, and evidence of mixing of the driver gas with the entrained air is evident up stream from the 22.5-m location.

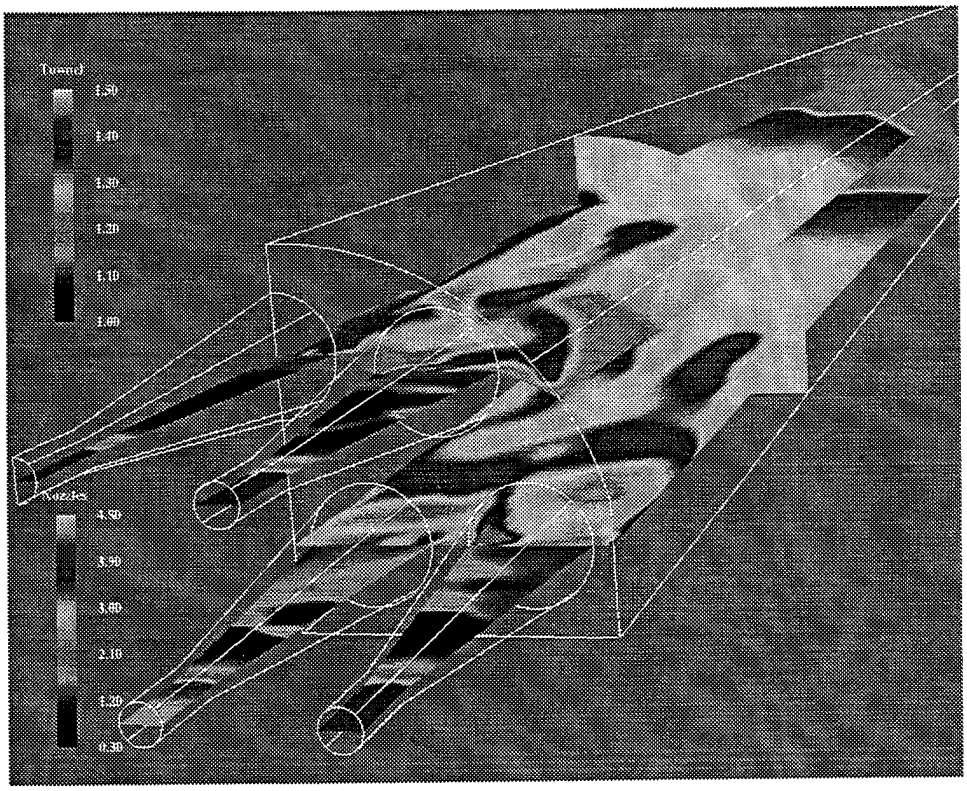

Figure 42. USA-RG3 Viscous Turbulent Solution: Density at 172 ms.

Figure 43 shows the density distribution in the computational domain at 302 ms. The single, continuous shade at the 67.5-m position indicates a uniform distribution of gas density at the test section, further evidence of uniform flow at that location. Regions of slightly elevated density are evident within the driver flow paths at the 22.5-m plane. In these

elevated regions, the density is approximately 1.35 kg/m^3, while the density elsewhere at the same cross section is nominally 1.28 kg/m^3, a variation of about 5%.

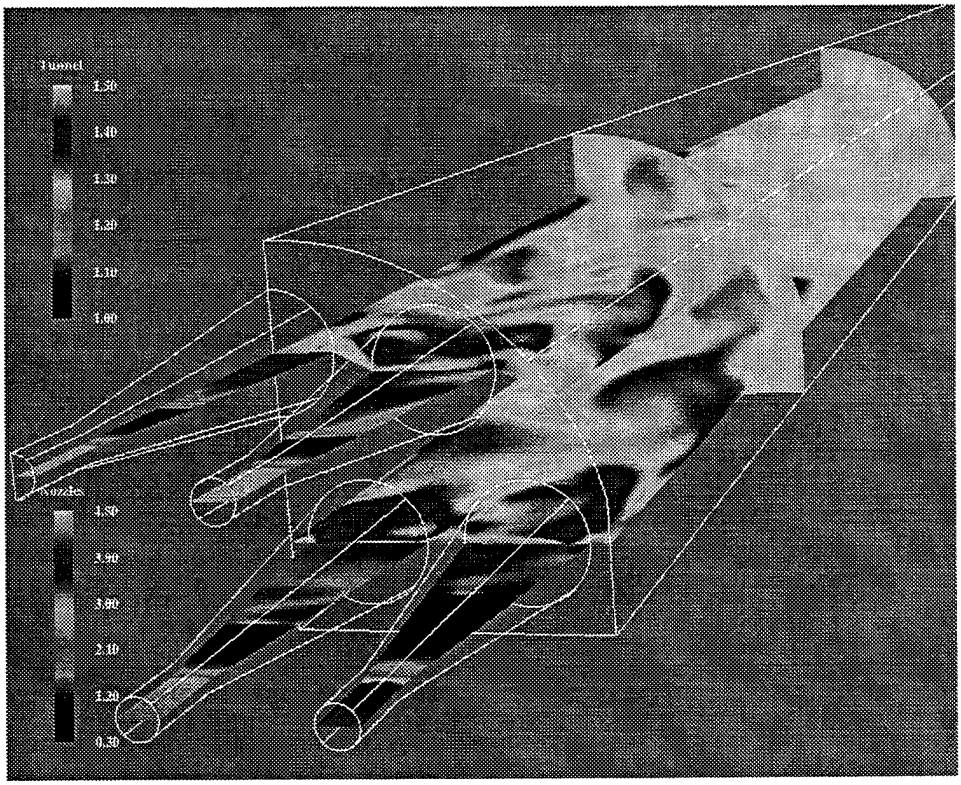

Figure 43. USA-RG3 Viscous Turbulent Solution: Density at 302 ms.

The USA-RG3 time history data are compared to the experimental records in the same manner as the SHARC results. The inviscid and viscous solution results for the 20-kPa and 80-kPa overpressure levels are compared to experimental data from the 67.5-m and 22.5-m locations in Figures 44 through 50. Again, the PB19 and PB4 gauge locations are the benchmarks against which the computational results are evaluated. The stagnation overpressure from PB19 on Test 1 is compared to the USA-RG3 calculations in Figure 44. This figure shows little difference between the two computational solutions. Both computational results closely follow the experimental data, with the greatest deviation occurring between 75 ms and 275 ms after shock arrival. The incident static overpressure predicted by the calculations was approximately 17.5 kPa, which is below the measured peak of 25 kPa.

The reason for the differences in the peak static overpressure lies in the resolution of the computational grid and the formulation of implicit CFD algorithms. Like the SHARC model, the grid resolution of the USA-RG3 model is near the minimum necessary to capture the dominant flow characteristics that are present in the SSGG. Increasing the grid resolution to capture more detail in the flow would make the run times unreasonably long.

The time step in implicit codes is determined by the Courant-Friedrichs-Lewy (CFL) stability condition.[27] Because the implicit formulation of the time-marching algorithm casts the entire system of equations into matrix form, the time step is not as strictly limited by

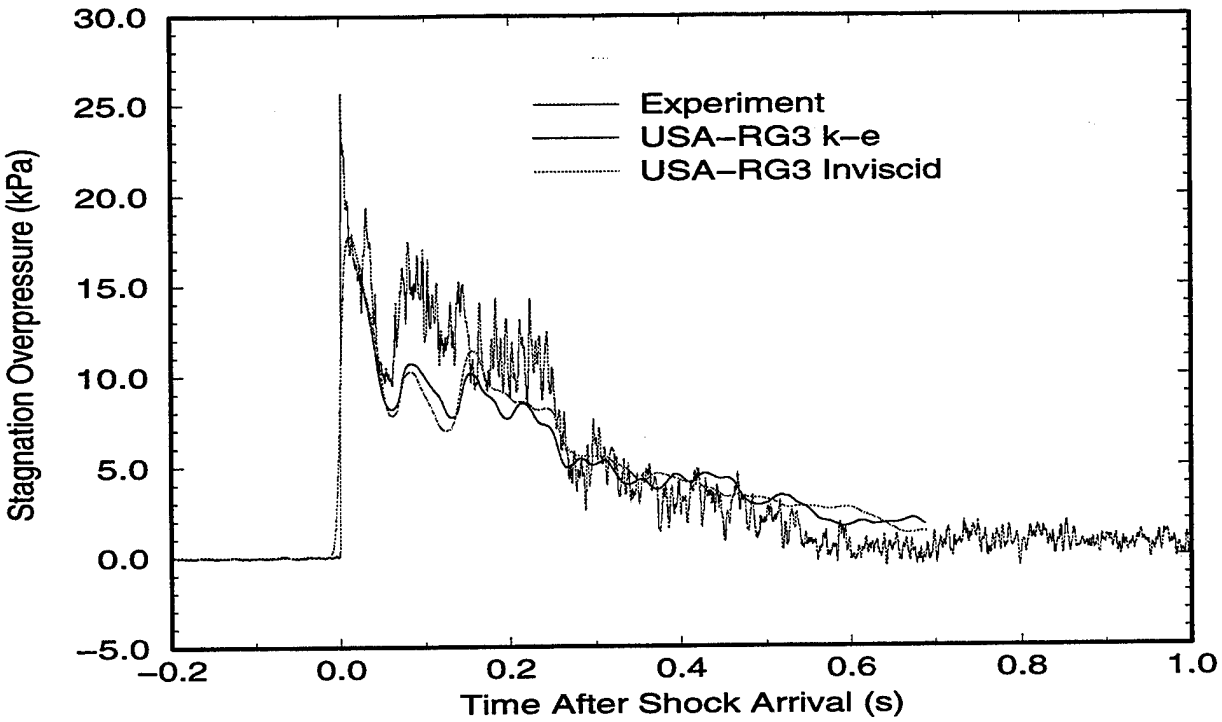

Figure 44. USA-RG3 Simulations of Test 1, Gauge PB19.

the computational cell size, particle velocity, and sound speed as in explicit schemes. The formulation of the implicit approach allows larger time steps to be realized by increasing the value of the CFL number used by the code. In each of the USA-RG3 calculations presented here, a CFL number of 10 was used for the entire computation. This value was selected as a compromise between definition of shock structure in the solution and the computer time required to complete the calculations.

This explanation for the reduced incident shock strength is further supported by the fact that the shock front does not have as steep a rise as the experiment or even the explicit SHARC results. To repeat these calculations with an initial CFL number of 1 until the leading shock had propagated past the 67.5-m measurement position, then increasing it to a value of 10 for the remainder of the calculation would probably produce a sharp shock front without significantly increasing the total CPU time required to complete the solutions.

The USA-RG3 predictions of the flow at the PB4 gauge for Test 1 are plotted in Figure 44. These experimental and computational results look very much like those of the previous figure because of the high level of flow uniformity in both the experiment and the calculations. Again, the rounded shock front on the leading edge of the computational records indicates a shock that is spread longitudinally across several computational planes because of the coarseness of the grid and the selected CFL number.

Figures 45 and 46 show the USA-RG3 predictions of stagnation overpressure at the 22.5-m instrumentation array location for Test 6. Both figures show that, closer to the upstream end of the expansion section, the shock front is not as rounded as in the computational

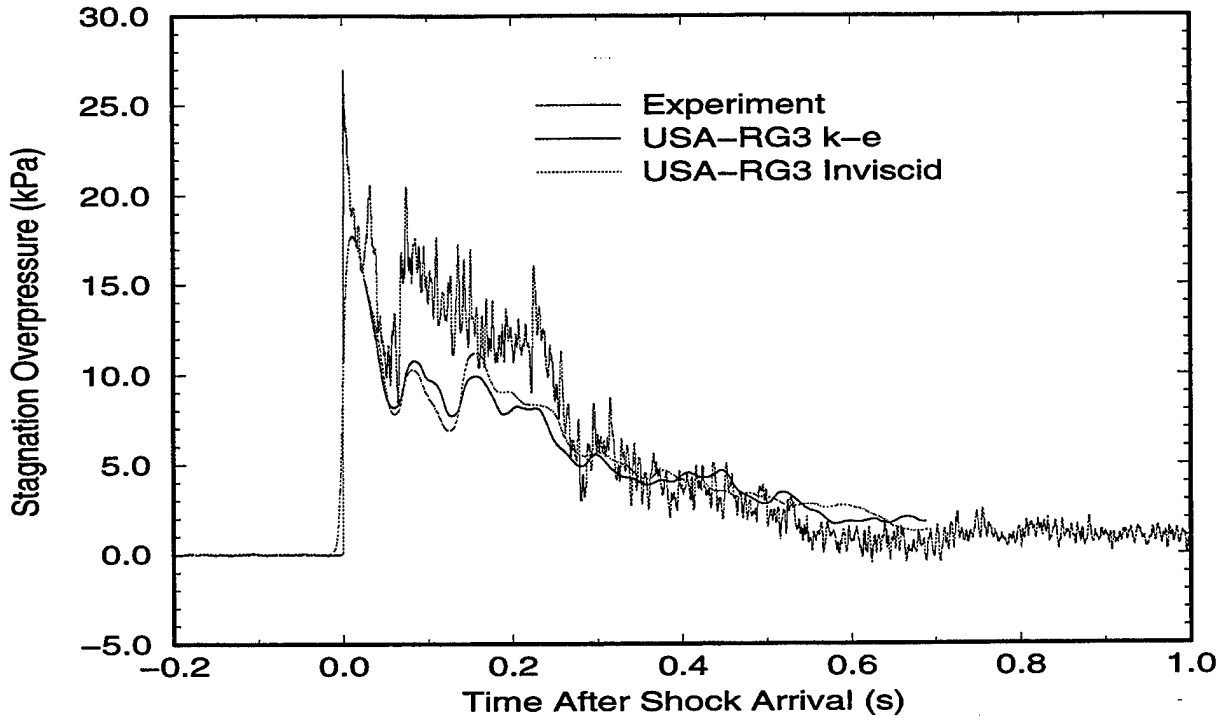

Figure 44. USA-RG3 Simulations of Test 1, Gauge PB4.

results at the 67.5-m location. Because the shock front has not traveled as far to reach this measurement position, there has been less opportunity for the solution to spread the shock front across the longitudinal grid planes. The PB19 comparisons in Figure 46 show that, like the SHARC results, the computation did not capture the jet flow effect observed in the path of the 44-m driver.

12.2. USA-RG3 Calculations of 80-kPa Tests

The simulations of the 80-kPa tests are summarized in Figures 47 through 50, with Test 2 comparisons in the first two figures and Test 8 comparisons in the last two. Figures 47 and 48 show that the USA-RG3 code again produced a somewhat rounded shock front. At the PB4 gauge in Figure 48, the predicted peak shock is nearly identical to the experiment, while the predicted shock strength at gauge PB19 is 5% greater than the measured peak. The difference between the peaks at these two gauge locations is in the experimental result, as the computations produce a peak static overpressure of 112 kPa uniformly across the 67.5-m cross section. The PB4 comparison shows that the computational results closely follow the experiment throughout the entire time of interest, with the computational results slightly lower than the experimental stagnation overpressure. The PB19 comparison shows the computational results, indicating a stagnation overpressure that is initially greater than the measured data, then falling slightly below the experimental record at 300 ms after shock arrival.

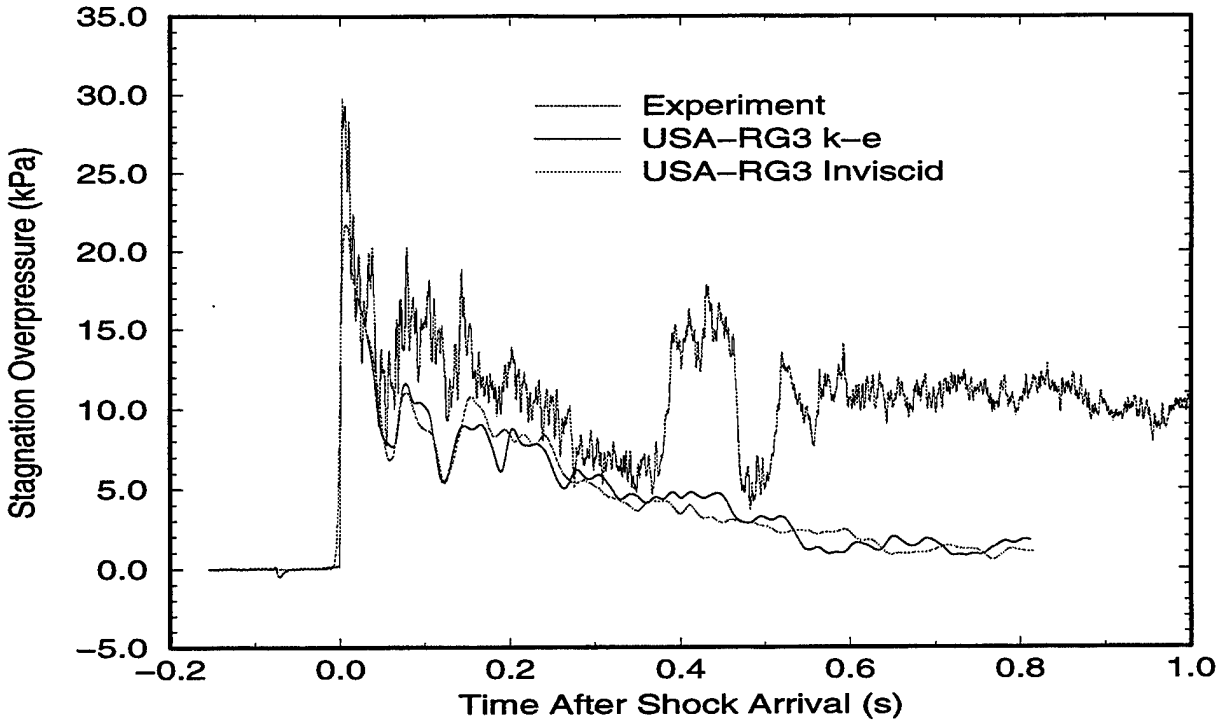

Figure 45. USA-RG3 Simulations of Test 6, Gauge PB19.

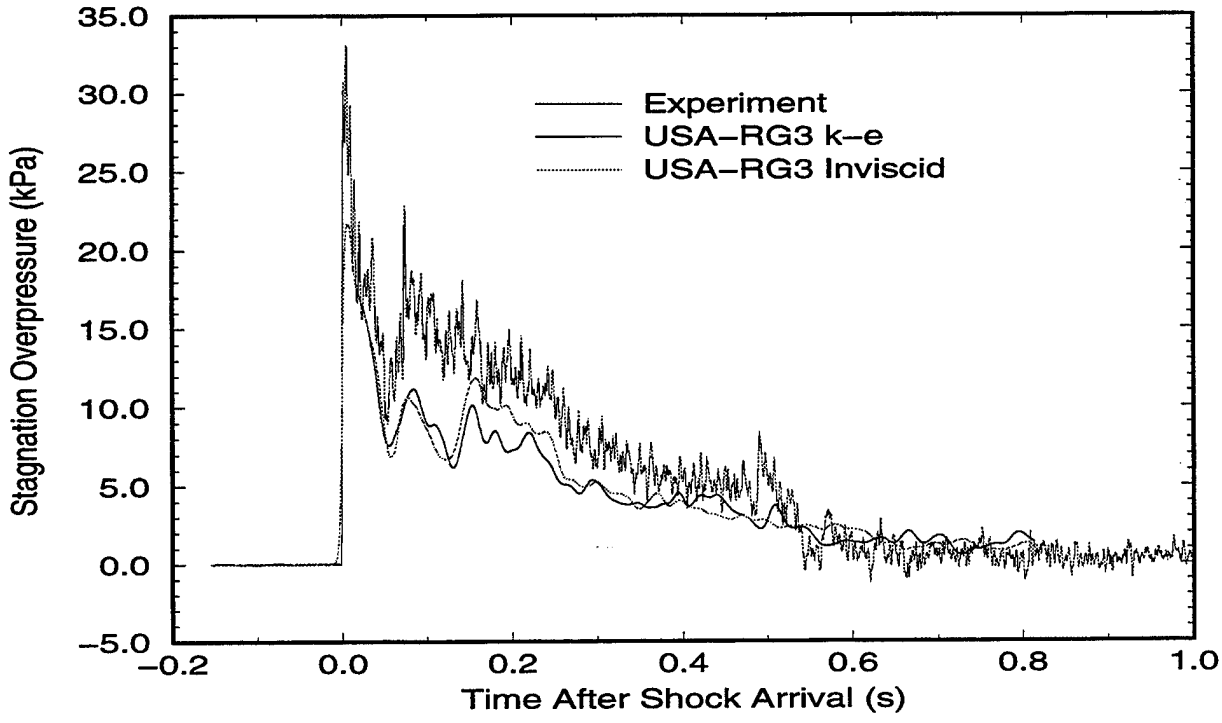

Figure 46. USA-RG3 Simulations of Test 6, Gauge PB4.

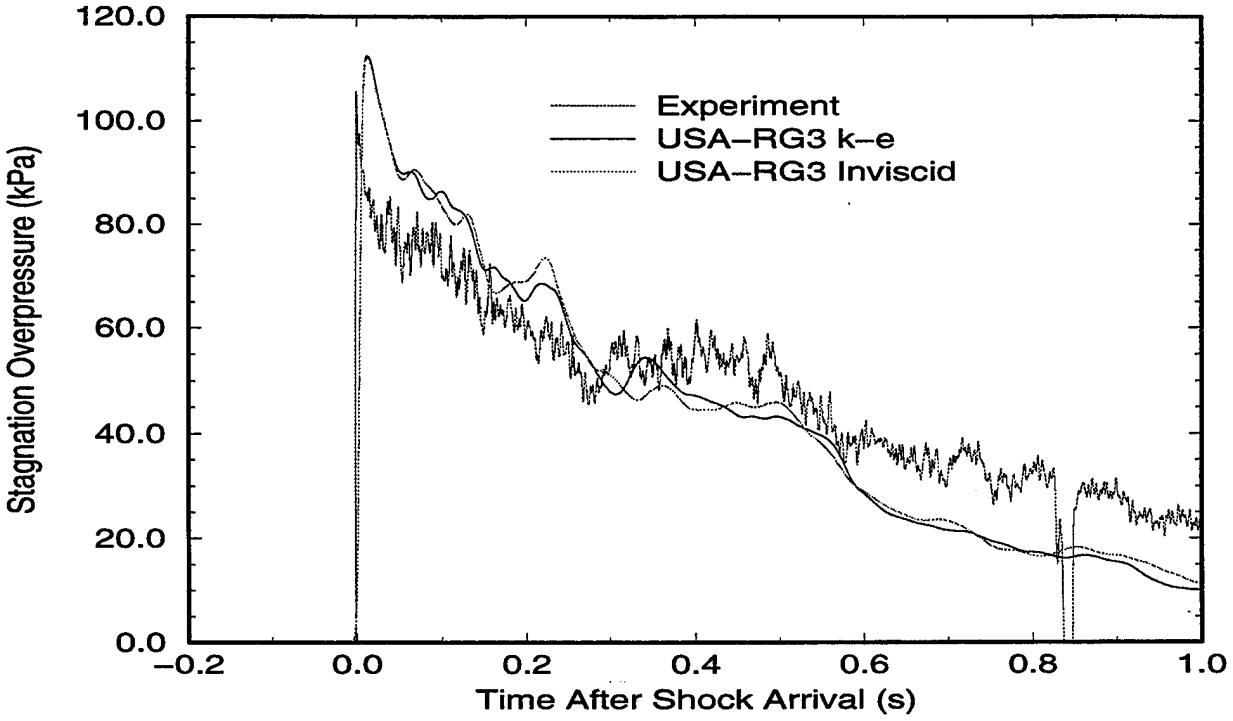

Figure 47. USA-RG3 Simulations of Test 2, Gauge PB19.

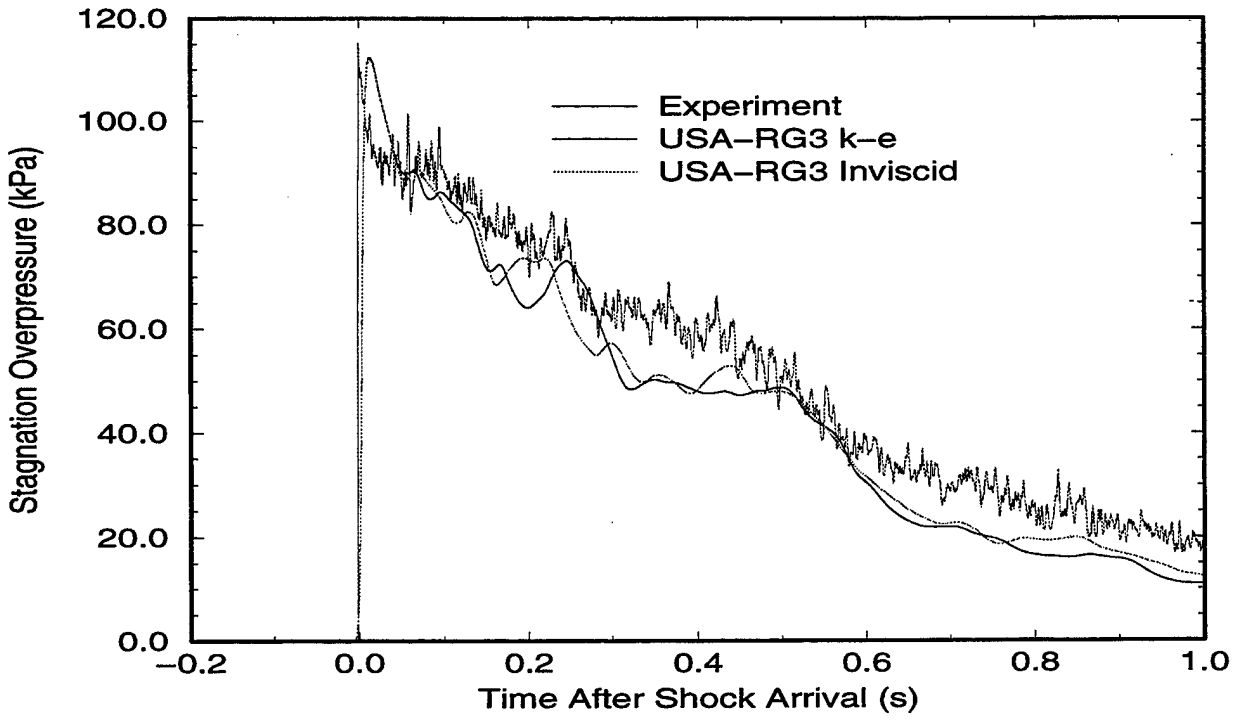

Figure 48. USA-RG3 Simulations of Test 2, Gauge PB4.

Finally, the stagnation overpressures from gauges PB19 and PB4 from Test 8 are compared to the 22.5-m station data in Figures 49 and 50. The PB19 record in the first figure is positioned within the path of the centerline of the 44-m driver and shows highly turbulent flow in the jet produced by that driver. The USA-RG3 inviscid and viscous, turbulent predictions both show erratic activity between 75 ms and 400 ms after shock arrival but generally do not follow the trend of the experimental data during that time interval. In this figure, the k-ϵ turbulence model in the USA-RG3 may behave in the exact opposite manner as the SHARC turbulence model in that it appears to be introducing too little diffusion to the flow field.

The PB4 stagnation overpressure comparison for Test 8 is seen in Figure 50. Here, the experimental data demonstrate only a few, sudden oscillations resulting from the jet flow from the neighboring drivers. The USA-RG3 predictions of stagnation overpressure at this gauge contain some large disturbances between 75 ms and 400 ms after shock arrival but otherwise closely follow the path of the experimental record. For both gauge locations examined at the 22.5-m test section at the 80-kPa overpressure level, the shock front produced by the USA-RG3 calculations has a steep rise and nearly exactly matches the peak static overpressure of the experiments.

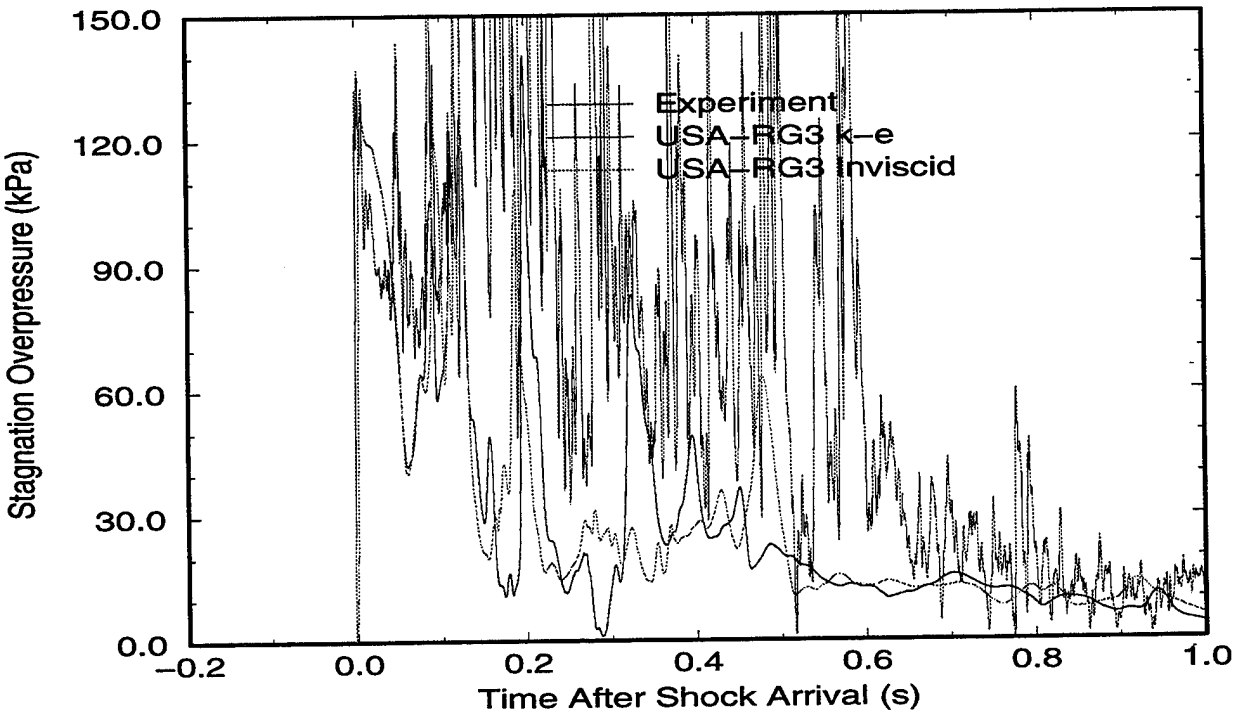

Figure 49. USA-RG3 Simulations of Test 8, Gauge PB19.

13. SUMMARY

A series of eight tests was performed to map the flow in the expansion tunnel of the SSGG large blast simulator. Four of the eight tests provided a set in which data were gathered at

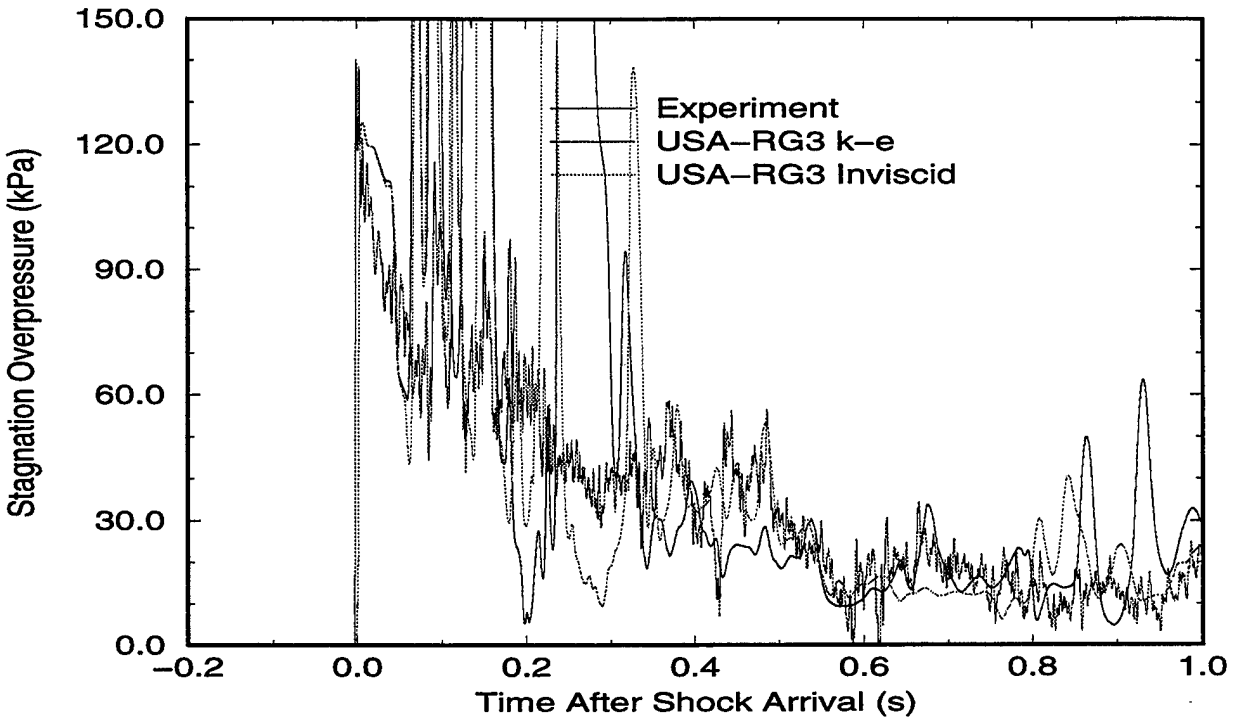

Figure 50. USA-RG3 Simulations of Test 8, Gauge PB4.

two longitudinal positions in the expansion tunnel, each at the same two overpressure levels. Analysis of these tests was performed by comparing flow characteristics from different gauge locations for a given test.

The static overpressure histories were found to be uniform across the entire cross-sectional area of the tunnel for all the tests. The data from the static and stagnation overpressure histories at the 67.5-m test section reveal a highly uniform environment for equipment testing throughout the range of overpressure levels.

Some evidence of jet flow was found from stagnation overpressure histories measured at the 22.5-m measurement position. This pattern occurred in the flow path of the 44-m driver in the 20-kPa overpressure test. Additional evidence of driver jet flow at the 22.5-m measurement position was found in the paths of each of the drivers in the 80-kPa test. At both pressure levels, this shear flow diffuses, resulting in the aforementioned uniform flow field at the test section.

This experimental effort provides a valuable set of three-dimensional, time-dependent, turbulent flow field data, which can be used to validate CFD codes. The data should help in the evaluation of the characterization tests of the U.S. LB/TS.

The USA-RG3 and SHARC codes were employed in a detailed, 3-D computational investigation that revealed many of the significant features, strengths, and weaknesses of these codes. The computational results presented in this report were selected to illustrate these strengths and weaknesses. The wealth of data produced by these calculations is too voluminous to be presented here.

Overall, the CFD codes do an excellent job of predicting the complex, time-dependent flow that exists in the SSGG blast simulator. Additionally, the codes demonstrated the capability to simulate 3-D blast phenomena of interest to ARL and much of the blast effects community. Both 3-D codes are used at ARL for problems that can be reasonably represented in a three-dimensional domain, without resulting in unreasonably long run times.

The calculations presented in this report also serve to further reinforce the need to adapt these types of CFD codes to scalable, parallel computer platforms to obtain significant increases in computational performance. This type of computing technology and robust CFD codes such as SHARC and USA-RG3 should make routine 3-D computations of blast effects a reality in the near future.

REFERENCES

1. Schraml, S.J. and R.J. Pearson. "Small Scale Shock Tube Experiments Using a Computer Controlled Active Rarefaction Wave Eliminator." BRL-TR-3149, U.S. Army Ballistic Research Laboratory, Aberdeen Proving Ground, MD. September 1989.

2. Schraml, S.J. and R.J. Pearson. "Characterization of Flow Distribution inf Axisymmetric Shock Tubes." BRL-TR-3353, U.S. Army Ballistic Research Laboratory, Aberdeen Proving Ground, MD. June 1992.

3. Brochure "Simulateur de Souffle à Grand Gabarit." Centre d'Etudes de Gramat, 46500 Gramat, France.

4. S. Gratias and J.B.G. Monzac. "Le Simulateur de Souffle à Grand Gabarit de Centre d'Etudes de Gramat - Conception, études, performance." Proceedings of the 7^{th} International Symposium on the Military Applications of Blast Simulation. Medicine Hat, Alberta, Canada. 13-17 July 1981.

5. A. Cadet and J.B.G. Monzac. "Le Simulateur de Souffle à Grand Gabarit de Centre d'Etudes de Gramat - Description et utilisation opérationelle." Proceedings of the 7^{th} International Symposium on the Military Applications of Blast Simulation. Medicine Hat, Alberta, Canada. 13-17 July 1981.

6. "Shock and blast simulation. Concept and definition of a Large Blast Simulator." Technical Papers T74-27a and T77-13a. Centre d'Etudes de Gramat, 46500 Gramat, France.

7. Gion, E.J. "A Multidriver Shock Tube Model of a Large Blast Simulator." BRL-MR-3757, U.S. Army Ballistic Research Laboratory, Aberdeen Proving Ground, MD. 1989.

8. Loucks, R.B. et al. "Simulation of Non-Ideal Blast with a Shock Tube Exit Jet." Proceedings of the 14^{th} International Symposium on the Military Aspects of Blast and Shock. Las Cruces, NM, 10-15 September 1995.

9. Ethridge, N.H. and J.H. Keefer. "Real (Non-Ideal) Surface Effects on Nuclear Explosion Airblast from PRISCILLA-Type Events." Applied Research Associates, Inc. Aberdeen MD. June 1995.

10. Needham, C.E., R.G. Ekler and L.W. Kennedy. "Extended Desert Calculation Results with Comparisons to PRISCILLA Experimental Data and a Near-Ideal Calculation." U.S. Army Research Laboratory Contract Report ARL-CR-235. Aberdeen Proving Ground, MD. July 1995.

11. Ethridge, N.H. "Proposed Design for a Differential Pressure Gage to Measure Dynamic Pressure in Blast Waves." U.S. Army Ballistic Research Laboratory Memorandum Report ARBRL-MR-02814. Aberdeen Proving Ground, MD. 1978.

12. Private conversation with Mr. P.C. Muller. Aberdeen Proving Ground, MD. March 1995.

13. Schraml, S.J. "A Data Parallel Implementation of the BRL-Q1D Code." U.S. Army Ballistic Research Laboratory Technical Report BRL-TR-3389. Aberdeen Proving Ground, MD. June 1992.

14. Schraml, S.J. "Evaluation of a Multiple Instruction / Multiple Data (MIMD) Parallel Computer for CFD Applications." U.S. Army Research Laboratory Technical Report ARL-TR-589. Aberdeen Proving Ground, MD. October 1994.

15. Crepeau, J.E. at al. "SHARC Hydrocode Computations of the PRISCILLA Event." S-Cubed Technical Report SSS-DFR-93-14283. October 1993.

16. Opalka, K.O. "Numerical Simulation of the Flow in a 1:57-Scale Axisymmetric Model of a Large Blast Simulator." U.S. Army Research Laboratory Technical Report ARL-TR-111. Aberdeen Proving Ground, MD. April 1993.

17. Kundu, P.K. "Fluid Mechanics." Academic Press, Inc. San Diego, CA. 1990.

18. Hikida, S., R. Bell, and C. Needham. "The SHARC Codes: Documentation and Sample Problems." S-Cubed Technical Report SSS-R-89-9878. September 1988.

19. Fry, M., R. Durret, G. Ganong, D. Matuska, M. Stucker, B. Chambers, C. Needham and C. Westmoreland. "The HULL Hydrodynamics Computer Code." U.S. Air Force Weapons Laboratory Technical Report 76-183. September 1977.

20. Barthel, J. "2-D Hydrocode Computations Using a k-ϵ Turbulence Model: Model Description and Test Calculations." S-Cubed Technical Report SSS-TR-85-7115. June 1985, (Footnotes added August 1988).

21. Needhan, C. at al. "Theoretical Calculations for Precursor Definition." DNA-TR-90-18, Defense Nuclear Agency, Washington, DC. September 1990.

22. Pierce, T. "Numerical Boundary Layer Analysis with k-ϵ Turbulence Model and Wall Functions." DNA-TR-87-15, Defense Nuclear Agency, Washington, DC. September 1986.

23. Chakravarthy, S., K. Szema, U. Goldberg, J. Gorski and S. Osher. "Application of a New Class of High Accuracy TVD Schemes to the Navier-Stokes Equations." AIAA Paper 85-0165. January 1985.

24. Ramakrishnan, S. and U. Goldberg. "Versatility of an Algebraic Backflow Turbulence Model." AIAA Paper 90-1485. 1990

25. Goldberg, U. and S. Chakravarthy. "Separated Flow Predictions Using a Hybrid $k - L$/Backflow Model." AIAA Journal, Volume 28, Number 6. pp. 1005-1009. June 1990.

26. Goldberg, U. and D. Ota. "A k-ϵ Near-Wall Formulation for Separated Flows." AIAA Paper 90-1482. 1990.

27. Roache, P.J. "Computational Fluid Dynamics." Hermosa Publishers. Albuquerque, NM. 1972

NO. OF COPIES	ORGANIZATION
2	ADMINISTRATOR DEFENSE TECHNICAL INFO CENTER ATTN DTIC DDA 8725 JOHN J KINGMAN RD STE 0944 FT BELVOIR VA 22060-6218
1	DIRECTOR US ARMY RESEARCH LABORATORY ATTN AMSRL OP SD TA/ RECORDS MANAGEMENT 2800 POWDER MILL RD ADELPHI MD 20783-1197
1	DIRECTOR US ARMY RESEARCH LABORATORY ATTN AMSRL OP SD TL/ TECHNICAL LIBRARY 2800 POWDER MILL RD ADELPHI MD 207830-1197
1	DIRECTOR US ARMY RESEARCH LABORATORY ATTN AMSRL OP SD TP/ TECH PUBLISHING BRANCH 2800 POWDER MILL RD ADELPHI MD 20783-1197
2	HQDA (SARD TR/MS K KOMINOS) (SARD TR/DR R CHAIT) WASHINGTON DC 20310-0103
2	DIRECTOR FEDERAL EMERGENCY MGMT AGENCY ATTN PUBLIC RELATIONS OFFICE TECHNICAL LIBRARY WASHINGTON DC 20472
2	HQDA (SARD TT/MS C NASH) (SARD TT/DR F MILTON) WASHINGTON DC 20310-0103
1	CHAIRMAN DOD EXPLOSIVES SAFETY BOARD ROOM 856 C HOFFMAN BLDG 1 2461 EISENHOWER AVENUE ALEXANDRIA VA 22331-0600
1	DIRECTOR OF DEFENSE RESEARCH AND ENGINEERING ATTN DD/TWP WASHINGTON DC 20301

NO. OF COPIES	ORGANIZATION
1	DIRECTOR DEFENSE INTELLIGENCY AGENCY ATTN DT 2/WPNS & SYS DIVISION WASHINGTON DC 20301
1	ASST SECRETARY OF DEFENSE (ATOMIC ENERGY ATTN DOCUMENT CONTROL WASHINGTON DC 20301
6	DIRECTOR DEFENSE NUCLEAR AGENCY ATTN CSTI TECHNICAL LIBRARY ESA W SUMMA E SEIDEN K PETERSEN WEP T KENNEDY M FRANKEL WASHINGTON DC 20305
1	CHAIRMAN JOINT CHIEFS OF STAFF ATTN J 5 R&D DIVISION WASHINGTON DC 20301
2	DA DCSOPS ATTN TECHNICAL LIBRARY DIR OF CHEM & NUC OPS WASHINGTON DC 20310
4	COMMANDER FIELD COMMAND DNA ATTN FCTTS E MARTINEZ FCTOSL F MOYNIHAN FCTIH H ROSS FCTIH W BRENNAN KIRTLAND AFB NM 87115
1	EUROPEAN RESEARCH OFFICE USARDSG (UK) ATTN DR R REICHENBACH BOX 65 FPO NEW YORK 09510-1500
10	CENTRAL INTELLIGENCE AGENCY DIR/DB/STANDARD ATTN GE 47 HQ WASHINGTON DC 20505
1	DIRECTOR ADVANCED RSCH PROJECTS AGENCY ATTN TECHNICAL LIBRARY 3701 NORTH FAIRFAX DRIVE ARLINGTON VA 22203-1714

NO. OF COPIES	ORGANIZATION
2	COMMANDER US ARMY NRDEC ATTN AMSNA D DR D SIELING STRNC UE J CALLIGEROS NATICK MA 01762
2	COMMANDER US ARMY CECOM ATTN AMSEL RD AMSEL RO TPPO P FORT MONMOUTH NJ 07703-5301
1	COMMANDER US ARMY CECOM R&D TECHNICAL LIBRARY ATTN ASQNC ELC IS L R MYER CTR FORT MONMOUTH NJ 07703-5000
1	MIT ATTN TECHNICAL LIBRARY CAMBRIDGE MA 02139
1	COMMANDER US ARMY FSTC ATTN RESEARCH & DATA BRANCH 220 7TH STREET NE CHARLOTTESVILLE VA 22901-5396
1	COMMANDER US ARMY ARDEC ATTN SMCAR FSM W/BARBER BLDG94 PICATINNY ARSENAL NJ 07806-5000
1	DIRECTOR US ARMY TRAC FT LEE ATTN ATRC L MR CAMERON FORT LEE VA 23801-6140
1	DIRECTOR US ARMY MISSILE & SPACE INTELLIGENCE CENTER ATTN AIAMS YDL REDSTONE ARSENAL AL 35898-5500
1	COMMANDING OFFICER (CODE L51) NAVAL CIVIL ENGINEERING LAB ATTN J TANCRETO PORT HUENEME CA 93043-5003

NO. OF COPIES	ORGANIZATION
2	COMMANDER US ARMY STRATEGIC DEFENSE CMD ATTN CSSD H MPL TECH LIB CSSD H XM DR DAVIES PO BOX 1500 HUNTSVILLE AL 35807
2	COMMANDER US ARMY CORPS OF ENGINEERS WATERWAYS EXPERIMENT STA ATTN CEWES SS R J WATT CEWES TL TECH LIBRARY PO BOX 631 VICKSBURG MS 39180-0631
1	COMMANDER US ARMY ENGINEER DIVISION ATTN HNDED FD PO BOX 1500 HUNTSVILLE AL 35807
3	COMMANDER US ARMY NUCLEAR & CHEM AGENCY 7150 HELLER LOOP SUITE 101 SPRINGFIELD VA 22150-3198
1	COMMANDER US ARMY CORPS OF ENGINEERS FT WORTH DISTRICT ATTN CESWF PM J PO BOX 17300 FORT WORTH TEXAS 76102-0300
1	DIRECTOR TRAC FLVN ATTN ATRC FORT LEAVENWORTH KS 66027-5200
1	COMMANDER US ARMY RESEARCH OFFICE ATTN SLCRO D PO BOX 12211 RESEARCH TRIANGLE PARK NC 27709-2211
1	COMMANDER NAVAL ELECTRONIC SYSTEMS CMD ATTN PME 117 21A WASHINGTON DC 20360
1	DIRECTOR HQ TRAC RPD ATTN ATRC RPR RADDA FORT MONROE VA 23651-5143

NO. OF COPIES	ORGANIZATION
2	OFFICE OF NAVAL RESEARCH ATTN DR A FAULSTICK CODE 23 800 N QUINCY STREET ARLINGTON VA 22217
1	DIRECTOR TRAC WSMR ATTN ATRC WC KIRBY WSMR NM 88002-5502
1	COMMANDER NAVAL SEA SYSTEMS COMMAND ATTN CODE SEA 62R DEPARTMENT OF THE NAVY WASHINGTON DC 20362-5101
2	COMMANDER US ARMY WSMR ATTN STEWS NED (DR MEASON) STEWS DATTS O (RL PENNY) WSMR NM 88002-5158
2	CHIEF OF NAVAL OPERATIONS DEPARTMENT OF THE NAVY ATTN OP 03EG OP 985F WASHINGTON DC 20350
1	COMMANDER DAVID TAYLOR RESEARCH CENTER ATTN CODE 522 TECH INFO CTR BETHESDA MD 20084-5000
1	OFFICER IN CHARGE (CODE L31) CIVIL ENGINEERING LABORATORY NAVAL CONST BATTALION CENTER ATTN TECHNICAL LIBRARY PORT HUENEME CA 93041
1	COMMANDING OFFICER WHITE OAK WARFARE CENTER ATTN CODE WA501 NNPO SILVER SPRING MD 20902-5000
1	COMMANDER (CODE 533) NAVAL WEAPONS CENTER ATTN TECHNICAL LIBRARY CHINA LAKE CA 93555-6001
1	COMMANDER DAHLGREN DIVISION NAVAL SURFACE WARFARE CENTER ATTN CODE E23 LIBRARY DAHLGREN VA 22448-5000

NO. OF COPIES	ORGANIZATION
1	COMMANDER NAVAL RESEARCH LABORATORY ATTN CODE 2027 TECH LIBRARY WASHINGTON DC 20375
1	OFFICER IN CHARGE WHITE OAK WARFARE CENTER DETACHMENT ATTN CODE E232 TECH LIBRARY 10901 NEW HAMPSHIRE AVENUE SILVER SPRING MD 20903-5000
1	AL/LSCF ATTN J LEVINE EDWARDS AFB CA 93523-5000
1	COMMANDER NAVAL WEAPONS EVALUATION FAC ATTN DOCUMENT CONTROL KIRTLAND AFB NM 87117
1	RADC (EMTLD/DOCUMENT LIB) GRIFFISS AFB NY 13441
1	AEDC ATTN R MCAMIS MAIL STOP 980 ARNOLD AFB TN 37389
1	AFESC/RDCS ATTN PAUL ROSENGREN TYNDALL AFB FL 32403
1	OLAC PL/TSTL ATTN D SHIPLETT EDWARDS AFB CA 93523 5000
1	AFIT/ENY ATTN LTC HASEN PHD WRIGHT PATTERSON AFB OH 45433-6583
2	AIR FORCE ARMAMENT LAB ATTN AFATL/DOIL AFATL/DLYV EGLIN AFB FL 32542-5000
1	DIRECTOR IDAHO NATIONAL ENGINEERING LAB ATTN SPEC PROGRAMS J PATTON 2151 NORTH BLVD MS 2802 IDAHO FALLS ID 83415

NO. OF COPIES	ORGANIZATION
3	PHILLIPS LABORATORY (AFWL) ATTN NTE NTED NTES KIRTLAND AFB NM 87117-6008
1	DIRECTOR LAWRENCE LIVERMORE NATL LAB ATTN TECH INFO DEPT L 3 PO BOX 808 LIVERMORE CA 94550
1	AFIT ATTN TECHNICAL LIBRARY BLDG 640/B WRIGHT PATTERSON AFB OH 45433
1	DIRECTOR NATL AERONAUTICS & SPACE ADMIN ATTN SCIENTIFIC & TECH INFO FAC PO BOX 8757 BWI AIRPORT BALTIMORE MD 21240
1	FTD/NIIS WRIGHT PATTERSON AFB OH 45433
3	KAMAN SCIENCES CORPORATION ATTN LIBRARY PA ELLIS FH SHELTON PO BOX 7463 COLORADO SPRINGS CO 80933-7463
4	DIRECTOR IDAHO NATIONAL ENGINEERING LAB EG&G IDAHO INC ATTN R GUENZLER MS 3505 R HOLMAN MS 3510 R A BERRY W C REED PO BOX 1625 IDAHO FALLS ID 83415
5	DIRECTOR SANDIA NATIONAL LABORATORIES ATTN DOC CONTROL 3141 C CAMERON DIV 6215 D GARDNER DIV 1421 J MCGLAUN DIV 1541 PO BOX 5800 ALBUQUERQUE NM 87185-5800

NO. OF COPIES	ORGANIZATION
2	LOS ALAMOS NATL LABORATORY MAIL STATION 5000 REPORT COLLECTION CID 14 MS P364 PO BOX 1663 LOS ALAMOS NM 87545
1	REPORT COLLECTION CIC 14 MS P364 LOS ALAMOS NATL LABORATORY LOS ALAMOS NM 87545
1	REPORT COLLECTION RESEARCH LIBRARY MS P362 PO BOX 7113 LOS ALAMOS NM 87544-7113
1	DIRECTOR SANDIA NATIONAL LABORATORIES LIVERMORE LABORATORY ATTN DOC CONTROL FOR TECH LIB PO BOX 969 LIVERMORE CA 94550
1	DIRECTOR NASA AMES RESEARCH CENTER APPLIED COMPUTATIONAL AERO BR ATTN DR T HOLTZ MS 202 14 MOFFETT FIELD CA 94035
1	DIRECTOR NASA LANGLEY RESEARCH CENTER ATTN TECHNICAL LIBRARY HAMPTON VA 23665
2	APPLIED RESEARCH ASSOCIATES INC ATTN J KEEFER NH ETHRIDGE PO BOX 548 ABERDEEN MD 21001
4	APPLIED RESEARCH ASSOCIATES INC ATTN C NEEDHAM J CREPEAU S HIKIDA R NEWELL 4300 SAN MATEO BLVD ALBUQUERQUE NM 87110
1	ADA TECHNOLOGIES INC ATTN JAMES R BUTZ HONEYWELL CENTER SUITE 110 304 INVERNESS WAY SOUTH ENGLEWOOD CO 80112

NO. OF COPIES	ORGANIZATION
1	ALLIANT TECHSYSTEMS INC ATTN ROGER A RAUSCH (MN48 3700) 7225 NORTHLAND DRIVE BROOKLYN PARK MN 55428
1	CARPENTER RESEARCH CORP ATTN H JERRY CARPENTER 27520 HAWTHORNE BLVD SUITE 263 PO BOX 2490 ROLLING HILLS ESTATES CA 90274
1	AEROSPACE CORPORATION ATTN TECH INFO SERVICES PO BOX 92957 LOS ANGELES CA 90009
1	GOODYEAR CORPORATION ATTN RM BROWN BLDG 1 SHELTER ENGINEERING LITCHFIELD PARK AZ 85340
1	THE BOEING COMPANY ATTN AEROSPACE LIBRARY PO BOX 3707 SEATTLE WA 98124
2	FMC CORPORATION ADVANCED SYSTEMS CENTER ATTN J DROTLEFF C KREBS MDP 95 BOX 58123 2890 DE LA CRUZ BLVD SANTA CLARA CA 95052
1	CALIFORNIA RES & TECH INC ATTN M ROSENBLATT 20943 DEVONSHIRE STREET CHATSWORTH CA 91311
1	SVERDRUP TECHNOLOGY INC SVERDRUP CORPORATION AEDC ATTN BD HEIKKINEN MS 900 ARNOLD AFB TN 37389-9998
1	DYNAMICS TECHNOLOGY INC ATTN D T HOVE G P MASON 21311 HAWTHORNE BLVD SUITE 300 TORRANCE CA 90503
1	KTECH CORPORATION ATTN DR E GAFFNEY 901 PENNSYLVANIA AVE NE ALBUQUERQUE NM 87111

NO. OF COPIES	ORGANIZATION
1	EATON CORPORATION DEFENSE VALVE & ACTUATOR DIV ATTN J WADA 2338 ALASKA AVE EL SEGUNDO CA 90245-4896
2	MCDONNELL DOUGLAS ASTRO-NAUTICS CORP ATTN R W HALPRIN K A HEINLY 5301 BOLSA AVENUE HUNTINGTON BEACH CA 92647
4	KAMAN AVIDYNE ATTN R RUETENIK S CRISCIONE R MILLIGAN T STAGLIANO 83 SECOND AVENUE NORTHWEST INDUSTRIAL PARK BURLINGTON MA 01830
1	MDA ENGINEERING INC ATTN DR DALE ANDERSON 500 EAST BORDER STREET SUITE 401 ARLINGTON TX 07601
2	POINTWISE INC ATTN J CHAWNER J STEINBRENNER PO BOX 210698 BEDFORD TX 76095-7698
2	PHYSICS INTERNATIONAL CORP PO BOX 5010 SAN LEANDRO CA 94577-0599
2	KAMAN SCIENCES CORPORATION ATTN DASIAC (2CYS) PO DRAWER 1479 816 STATE STREET SANTA BARBARA CA 93102-1479
1	LOGICON RDA ATTN GP GANONG PO BOX 9377 ALBUQUERQUE NM 87119
1	LOGICON RDA ATTN B LEE 6053 W CENTURY BLVD LOS ANGELES CA 90045

NO. OF COPIES	ORGANIZATION
1	LOCKHEED MISSILES & SPACE CO ATTN J J MURPHY DEPT 81 11 BLDG 154 PO BOX 504 SUNNYVALE CA 94086
1	SCIENCE CENTER ROCKWELL INTERNATIONAL CORP ATTN S RAMAKRISHNAN D OTA 1049 CAMINO DOS RIOS PO BOX 2085 THOUSAND OAKS CA 91358
1	METACOMP TECHNOLOGIES INC ATTN S CHAKRAVARTHY 650 WESTLAKE BLVD SUITE 203 WESTLAKE VILLAGE CA 91362
1	ORLANDO TECHNOLOGY INC ATTN D MATUSKA 60 SECOND STREET BLDG 5 SHALIMAR FL 32579
4	S CUBED A DIVISION OF MAXWELL LABS INC ATTN TECHNICAL LIBRARY R DUFF K PYATT J BARTHEL PO BOX 1620 LA JOLLA CA 92037-1620
1	SAICORPORATION ATTN J GUEST 2301 YALE BLVD SE SUITE E ALBUQUERQUE NM 87106
1	SUNBURST RECOVERY INC ATTN DR C YOUNG PO BOX 2129 STEAMBOAT SPRINGS CO 80477
1	SAICORPORATION ATTN N SINHA 501 OFFICE CENTER DRIVE APT 420 FT WASHINGTON PA 19034-3211
1	SVERDRUP TECHNOLOGY INC ATTN RF STARR PO BOX 884 TULLAHOMA TN 37388

NO. OF COPIES	ORGANIZATION
1	S CUBED A DIVISION OF MAXWELL LABS INC ATTN JAMES SEVIER 2501 YALE BLVD SE ALBUQUERQUE NM 87106
3	SRI INTERNATIONAL ATTN DR GR ABRAHAMSON DR J GRAN DR B HOLMES 333 RAVENWOOD AVENUE MENLO PARK CA 94025
1	TRW BALLISTIC MISSILE DIVISION ATTN H KORMAN MAIL STATION 526/614 PO BOX 1310 SAN BERNADINO CA 92402
1	BATTELLE ATTN TACTEC LIB JN KHIGGINS 505 KING AVENUE COLUMBUS OH 43201-2693
1	THERMAL SCIENCE INC ATTN R FELDMAN 2200 CASSENS DRIVE ST LOUIS MO 63026
2	DENVER RESEARCH INSTITUTE ATTN J WISOTSKI TECHNICAL LIBRARY PO BOX 10758 DENVER CO 80210
1	STATE UNIVERSITY OF NEW YORK MECH & AEROSPACE ENGINEERING ATTN DR PEYMAN GIVI BUFFALO NY 14260
2	UNIVERSITY OF MARYLAND INST FOR ADV COMPUTER STUDIES ATTN L DAVIS G SOBIESKI COLLEGE PARK MD 20742
1	CALIFORNIA INST OF TECHNOLOGY ATTN T J AHRENS 1201 E CALIFORNIA BLVD PASADENA CA 91109

NO. OF COPIES	ORGANIZATION
1	STANFORD UNIVERSITY ATTN DR D BERSHADER DURAND LABORATORY STANFORD CA 94305
1	UNIVERSITY OF MINNESOTA ARMY HIGH PERF COMP RES CTR ATTN DR TAYFUN E TEZDUYAR 1100 WASHINGTON AVE SOUTH MINNEAPOLIS MN 55415
3	SOUTHWEST RESEARCH INSTITUTE ATTN DR C ANDERSON S MULLIN A B WENZEL PO DRAWER 28255 SAN ANTONIO TX 78228-0255
2	COMMANDER US ARMY NRDEC ATTN SSCNC YSD (J ROACH) SSCNC WST (A MURPHY) KANSAS STREET NATICK MA 10760-5018
	ABERDEEN PROVING GROUND
5	DIR ARL ATTN AMSRL OP AP L (TECH LIB) BLDG 305 APG
1	COMMANDER US ARMY TECOM ATTN AMSTE TE F (L TELETSKI) RYAN BLDG APG
1	COMMANDER US ARMY THAMA ATTN AMSTH TE APG -EA
1	COMMANDER US ARMY TEST CENTER ATTN STEC LI APG
27	DIRECTOR US ARMY RESEARCH LABORATORY ATTN AMSRL SC C C NIETUBICZ AMSRL SC CC C ELLIS D HISLEY P COLLINS T KENDALL R SHEROKE AMSRL SC I W STUREK AMSRL SC S R PEARSON AMSRL SL CM E FIORVANTE AMSRL WT TB R FREY J STARKENBERG K BENJAMIN W LAWRENCE T DORSEY R LOTTERO V SMITH J CONDON L FERGUSON R LOUCKS C MERMAGEN A MIHALCIN P MULLER S SCHRAML J SULLIVAN AMSRL WT PB P PLOSTINS P WEIHNACHT B GUIDOS AMSRL WT TC K KIMSEY